

**Stellar populations in the  
Carina dSph galaxy and in  
the globular cluster Omega  
Centauri**

Matteo Monelli



*Ad Elisa e Giuliana*



**Homer Simpson:** *All right brain, you don't like me, and I don't like you. But let's just get me through this, and I can get back to killing you with beer.*

**Homer's brain:** *It's a deal.*



## Abstract

Dwarf spheroidal galaxies (dSphs) in the Local Group are fundamental laboratories to constrain not only cosmological theories concerning the so-called hierarchical paradigm, but also to trace back in time the star formation history and the chemical enrichment of these systems. dSph are good candidate to be the building blocks needed to assemble big galaxies in the hierarchical scenario. The high Mass-to-Light (M/L) ratio estimated seem to indicate that they are Dark Matter dominated. However, photometric survey have brought the evidence of the presence of extra-tidal stars around these objects. This could be the signature of tidal interaction between dSphs and the Galaxy, and may explain the high M/L estimated. The study of stellar populations of these nearby objects may help us to understand the nature of these elusive galaxies, and how they interact with the Galaxy. We present in this thesis the result of a photometric campaign aimed at studying the stellar content of two particularly interesting objects, namely the Carina dSph galaxy and the globular cluster Omega Centauri. Carina is the prototype of dSph with complex star formation history. It hosts at least three different populations, which formed in bursting episodes spaced out by long quiescent phases. The main events occurred  $\approx 11$ , 5 and less than 1 Gyr ago. The lack of gas, and the fact the last the last perigalacticon passage occurred  $\approx 2$  Gyr ago, make the formation of the youngest population a real puzzle. Moreover, the spatial distribution of older and younger stars appear different, the former being more centrally concentrated while the old population is distributed in a sort of diffused halo. The possible detection of extra-tidal stars has been debated in the literature, but no firm detection has been established yet. We present a photometric a spectroscopic study of the stellar populations the Carina dSph. We investigated the stellar content on the central region, and exploited the wide field imagers available on medium class telescope to investigate the occurrence of extra-tidal stars. The other topic of this thesis is Omega Centauri. This peculiar cluster is considered as the missing ring between dwarf galaxies and globular clusters. In fact it is the only globular cluster characterized by undisputed multiple stellar populations and a spread in the metal content. Moreover, it has been suggested the existence of tidal tails along the Omega Cen orbit, but these results are not well established. However, recent theoretical simulations support the evidence that Omega Cen might be the core of a dwarf galaxy, which has lost most of its stellar content along the orbit. We present a multivawelength photometric study based on both ground-based as well HST data.



## Acknowledgments

This work has been done in the framework of a collaboration between the Università di Roma "Tor Vergata", the Osservatorio Astronomico di Roma, the Osservatorio Astronomico di Trieste, the Cerro Tololo Inter-American Observatory, the Dominion Astronomical Observatory, the Michigan State University. The collaboration has involved Roberto Buonanno, Giuseppe Bono, Carlo E. Corsi, Mario Nonino, Alistair R. Walker, Peter B. Stetson, and Horace A. Smith.

These collaborators are sincerely acknowledged for their contributions to this thesis.



# Contents

<b>1</b>	<b>Introduction</b>	<b>1</b>
1.1	Are dwarf Spheroidals DM dominated? . . . . .	2
1.2	Dwarf Spheroidals and Globular Clusters . . . . .	2
1.3	Thesis project . . . . .	3
<b>2</b>	<b>Observational strategies and reduction techniques</b>	<b>5</b>
2.1	General concepts of digital image processing . . . . .	5
2.2	Stellar photometry: DAOPHOT and ALLFRAME . . . . .	8
2.3	Recipe for a good PSF . . . . .	11
2.4	Photometric calibration of wide field imagers: the example of Carina . . . . .	12
2.4.1	The calibration strategy . . . . .	13
2.4.2	Positional effects of the Wide Field Imager . . . . .	19
2.5	Calibration of the external fields . . . . .	21
<b>3</b>	<b>The Carina dSph galaxy</b>	<b>24</b>
3.1	Overview . . . . .	24
3.1.1	The chemical enrichment history . . . . .	27
3.1.2	Spatial distributions . . . . .	28
3.1.3	Variable stars . . . . .	29
3.2	The Carina Project . . . . .	31
3.2.1	The Central Region: data and reduction strategy . . . . .	32
3.2.2	The Color-Magnitude Diagrams . . . . .	33
3.2.3	Radial distributions . . . . .	41
3.2.4	Field Subtraction . . . . .	46
3.2.5	Moving outward . . . . .	51
3.2.6	Spectroscopic analysis of Carina stars . . . . .	61
<b>4</b>	<b>The globular cluster Omega Centauri</b>	<b>64</b>
4.1	General description . . . . .	64
4.2	Distance and orbit . . . . .	64
4.3	Structure and shape . . . . .	65
4.4	Multiple populations . . . . .	66

4.5	Overview of the data sets . . . . .	71
4.5.1	The VLT data . . . . .	71
4.5.2	The HST data . . . . .	73
4.5.3	Infrared observations . . . . .	77
4.5.4	Tidal tails in $\omega$ Cen? . . . . .	78
4.6	White dwarfs in $\omega$ Cen . . . . .	81
4.6.1	Discussion . . . . .	90
<b>5</b>	<b>Conclusions</b>	<b>94</b>
5.1	Stellar populations in the Carina dSph galaxy . . . . .	94
5.1.1	Future perspectives . . . . .	95
5.2	Stellar populations in $\omega$ Cen . . . . .	95
5.2.1	Future perspectives . . . . .	97
<b>A</b>	<b>Publications</b>	<b>99</b>

# Chapter 1

## Introduction

The study of the stellar populations in the Galaxy and in the Local Group (LG) is crucial to understand the formation and evolution of galaxies. Within the Local Group the Galaxy and M31 are the biggest objects, the only two giant spirals that dominate the mass of the system. However, they are surrounded by more than 40 dwarf galaxies, that show a huge spectrum of properties in term of stellar populations, chemical evolution, and gas content. All the morphological types are present in the LG, with the exception of a giant elliptical. These nearby galaxies can now be resolved in stars, and this means that a detailed study on a star-by-star basis can be made. The class of dwarf galaxies is the most populated in the whole Universe, and the sample of dwarfs in the LG offer the unique possibility to test locally the prediction of theoretical models concerning the evolution of galaxies.

In the  $\Lambda$ Cold Dark Matter (CDM) framework, this process is described as a continous merging of small objects to form larger and larger galaxies (White & Frenk 1991). This means that the dwarf galaxies we observe today might be the relics of this merging process, and therefore the witnesses of the first structures formed in the Universe. Among the different morphological types of dwarf galaxies, the so-called dwarf spheroidals are the ideal candidates for the hierarchical process. The estimated Mass-to-Light ( $M/L$ ) ratio ranges from  $\approx 5$  for Fornax (Mateo 1998), to more than 300 in the case of Draco (Kleyna et al. 2001), thus supporting the idea that these small systems are Dark Matter dominated.

Moreover, the disrupting Sagittarius dSph is a strong evidence that this merging process is still ongoing, and may play an important role in building the Galactic halo (Frinchaboy et al. 2004). Concerning the star formation history, theory predicts that these "building blocks" should have experienced a star formation event in ancient epochs (Cen 2001), but they should not have had the possibility to retain gas and form stars in recent epochs. This seems to be supported by the low internal velocity dispersion ( $\leq 10$ km/s), together with the absence of both dust and gas (Mateo 1998; Carignan et

al. 1998). However, it has been clearly demonstrated (Stetson, Hesser & Smacker-Hane 1998; Monelli et al. 2003; Tolstoy et al. 2004) that the star formation history of most dwarf spheroidals is complicated and several of them have experienced star formation events in recent epochs (less than 1Gyr). This is confirmed in most of the LG dSph, and only a few of them, namely Tucana (Lavery et al. 1996; Castellani, Marconi & Buonanno 1996) and possibly Ursa Minor (Carrera et al. 2002; Ikuta & Arimoto 2002) and Draco (Dolphin 2002), host a *single* stellar population older than  $\approx 10$  Gyr that might be coeval to Galactic Globular Cluster (GGCs).

## 1.1 Are dwarf Spheroidals DM dominated?

One possible explanation for the high  $M/L$  ratio is that the dSphs are dominated by Dark Matter. However, large photometric surveys suggest the presence of extra-tidal stars around several dSphs (Irwin & Hatzidimitriou 1995), and in particular Carina (Kuhn et al. 1996; Majewski et al. 2000a). This could be a signature of ongoing tidal interaction of these systems with the Galactic potential. If this is the case, the assumption that dSphs are in virial equilibrium would fail, and the actual estimate of the  $M/L$  ratio could be inflated. However, recent  $N$ -body simulations by Hayashi et al. (2003) and Kazantzidis et al. (2004) suggest that dSph may be surrounded by an extended halo of DM. In these scenarios, the tidal radii actually measured would be heavily underestimated. This implies that the detection of extra-tidal stars in dSphs cannot rule out the possibility that these stars are still bound to the galaxy rather than belonging to a tidal tail.

Characteristic	dSphs	GCs
Mv (mag)	$-8 \div -13$	$-10 \div -2$
Mass ( $M_{\odot}$ )	$10^6 \div 10^8$	$10^5$
Ellipticity, $\epsilon = (1-b/a)$	$> 0.13$	$< 0.1$
$\Delta[\text{Fe}/\text{H}]$ , dex	$0.2 \div 1.4$	$< 0.1$
$I_0$ , ( $L_{\odot} \text{ pc}^{-3}$ )	$0.005 \div 0.1$	$10^4 \div 10^5$
$\rho_0$ ( $M_{\odot} \text{ pc}^{-3}$ )	$0.07 \div 0.6$	$0.03 \div 5.6$
$\sigma_v$ , $\text{km s}^{-1}$	$< 10$	$1 \div 14$
$r_c$ (pc)	$110 \div 500$	$2 \div 20$
$r_t$ (pc)	$1400 \div 2500$	$2 \div 200$
M/L ( $M_{\odot}/L_{\odot}$ )	$5 \div 330$	$1 \div 4$

Table 1.1: Qualitative comparison between dSphs (Mateo 1998; Irwin & Hatzidimitriou 1995) and globular clusters (Harris 1996).

## 1.2 Dwarf Spheroidals and Globular Clusters

For many years dSphs have been considered as a sort of looser analogue of Globular Clusters, but now it is clear that the nature of these two classes of objects is different. dSph galaxies are characterized (see tab. 1.1) by larger tidal radii ( $r_t$ ), and much smaller central densities. The small internal velocity dispersion of GCs implies very small values of the  $M/L$ , steadily estimated of the order of the unity. The only noticeable exception is given by  $\omega$  Cen, which presents  $M/L \approx 3 \div 6$  (Velrome 2003). Moreover, recent empirical evidence suggests that the occurrency of multiple stellar populations and a spread in the metal abundances among dSphs is the rule rather than the exception. These features indicate that these systems are substantially different from GCs. Once again, the only exception is  $\omega$  Cen, which presents at least three different stellar populations and a large spread in metallicity.

Finally, it is worth mentioning that empirical evidence supports the occurrence of tidal tails in several GCs (Grillmair et al. 1995; Leon, Meylan & Combes 2000). This feature has been soundly confirmed by the detection of a huge (more than  $10^\circ$  across the sky) tidal tail around Palomar 5 (Odenkirchen et al. 2003).

## 1.3 Thesis project

Current spectroscopic and photometric investigations of dSphs and GCs might be affected by selection effects. Spectra have only been collected for a few bright Red Giant stars. The same applies for the stellar tracers currently adopted to detect tidal tails. Only during the last few years the use of multi-object spectrographs available on the 8-m class telescopes (ESO: VIMOS, FLAMES, FORS; Gemini: GMOS; Keck: DEIMOS; Subaru: FOCAS) and wide field CCD cameras available on the 2-4m class telescopes (WFC@INT, WFI@2.2m ESO, MOSAICII@Blanco CTIO, OmegaCam@CFHT) provided the opportunity to investigate fainter MS stars in these stellar systems.

We selected two particularly interesting objects, namely the Carina dSph galaxy and the GC  $\omega$  Cen. Carina is the prototype of dSph with complex star formation history. It hosts at least three different populations, which formed in bursting episodes spaced out by long quiescent phases (Smecker-Hane et al. 1996). The main events occurred  $\approx 11$ , 5 and less than 1 Gyr ago. The lack of gas, and the fact the last the last perigalacticon passage occurred  $\approx 2$ Gyr ago (Piatek et al. 2003), make the formation of the youngest population a real puzzle. Moreover, the spatial distribution of older and younger stars appears different, the former being more centrally concentrated while the old population is distributed in a sort of diffused halo. The possible detection of extra-tidal stars has been debated in the literature (Kuhn et al. 1996; Majewski et al. 2000a; Morrison et al. 2001;

Walcher et al. 2003), but no firm detection has been established yet. We present a photometric and spectroscopic study of the stellar populations of the Carina dSph. We investigated the stellar content on the central region, and exploited the wide field imagers available on medium class telescope to investigate the occurrence of extra-tidal stars.

The other topic of this thesis is  $\omega$  Cen. This peculiar cluster is considered as the missing ring between dwarf galaxies and globular clusters. In fact it is the only GC characterized by undisputed multiple stellar populations and a spread in the metal content. Moreover, Leon, Meylan & Combes (2000) suggested the existence of tidal tails along the  $\omega$  Cen orbit, but their results were questioned by Law et al. (2003). However, recent theoretical simulations support the evidence that  $\omega$  Cen might be the core of a dwarf galaxy, which has lost most of its stellar content along the orbit (Chiba & Mizutani 2004). We present a multivavelength photometric study based on both ground-based as well HST data.

Note that dSph galaxies are fundamental laboratories to constrain the accuracy and plausibility of evolutionary and pulsational predictions for intermediate mass stars in the metal-poor regime. These systems present a mean metallicity that either is not present in nearby dwarf Irregulars (Magellanic Clouds) or is present in the outskirts of the Galactic disk. The same outcome applies to  $\omega$  Cen that provides the opportunity to investigate H and He burning phases of stellar populations characterized by different chemical compositions and located at the same distance (e.g. the  $M_V$ -[Fe/H] relation for RR Lyrae stars).

## Chapter 2

# Observational strategies and reduction techniques

CCD cameras have been introduced roughly 25 years ago, and their use was as revolutionary as the photographic plates had been one century before. The observational astronomy experienced the possibility to have two dimensional, high-sensitivity, digital, and, probably most important, linear sensors. This led to the creation of new analysis techniques, and the development of software able to manage the new data sets. The experience acquired in the last decades has now restricted most of the reduction process of astronomical digital images to few standard and well understood steps.

This chapter summarizes all the details of the observational strategy and the reduction techniques used. We will review the standard pre-reduction process, and then focus on the ALLFRAME package used for the photometric reduction. Particular attention will be paid on the PSF extraction and the calibration process, especially for ground-based wide field CCD cameras.

### 2.1 General concepts of digital image processing

In order to understand how to analyse digital astronomical images, it is crucial to understand the error sources that can affect the measurements, and how they can be removed. The process to obtain meaningful numbers from a CCD image has to deal with all the noise sources that contribute to the uncertainty of any astrophysical quantity derived. A very schematic view of the overall acquisition process is illustrated in fig. 2.1. A "classical" image, that is a continuous distribution of light incoming on the focal plane is subject to:

- *sky* (background pollution by diffuse emission, zodiacal light, moon, telluric lines, human light pollution...)
- *atmosphere* (turbulence, extinction, seeing variations, humidity)
- *telescope* (jitter, tracking error, scattered light, thermal emission)

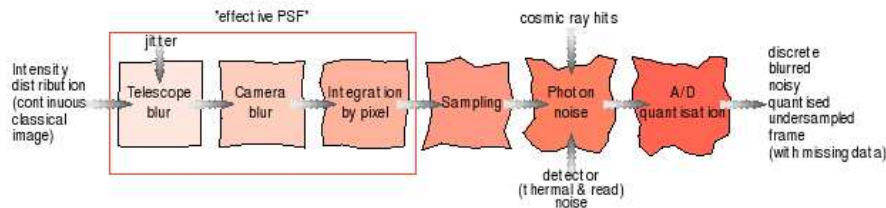


Figure 2.1: Figure 1 from Adorf (1995) illustrating the scheme of image blurring.

- **optics** (optics transmission, misalignments)
- **camera** blur (homogeneity of the camera response, charge diffusion, gain variation, read out noise, hot pixels, dead pixels)
- **pixel** blur (discretization effects, different pixel response function, under-sampling)
- **photon noise** (cosmic rays, thermal noise)
- **Analogue-to-Digital** quantisation,

resulting in a discrete, blurred, noisy, quantised, (sometimes) undersampled digital image. Part of these effects can be estimated and removed. At the end of the pre-reduction process, ideally, the only noise sources that cannot be removed should be the photon noise (unavoidable Poisson statistic), the conditions of the atmosphere (mainly seeing) and intrinsic to the nature of the source (crowding, faintness, morphology, variability). The blurring effect due to the electronics and defects of the instruments can in principle be reduced to the level of 1%.

We can model the "true" image  $I(x,y)$  as a function of the raw recorded raw image  $R(x,y)$  as:

$$Raw = (Image + sky \times (1+fringe) + tbe) \times otv \times qe + dark + flash + bias$$

where:

**sky** accounts for all the photons that join the signal between the source and the telescope;

**fringe** is the fringing interference pattern between the light along the optics or the sensor;

**tbe** is the thermal background emission from the telescope;

**otv** is the optical transmission variation, responsible of light absorption along the optical path;

**qe** quantum efficiency of the detector;

**dark** is the dark current emitted by the CCD itself;

**flash** is the charge present in the CCD due to preflash exposure before the observation;

*bias* is the zero integration time electronics background.

The logical sequence to clean the raw data starts by correcting for the additive effects. These take into account the dark current emission from the camera (usually negligible in modern sensors), the pre-flash exposure, and the bias level. In practice, many bias exposures are taken for every observing run, and a median image is subtracted from the scientific data in order to have the correct zero point of the photometric scale of the instrument.

The new image

$$\mathbf{Raw} - \langle \mathbf{BIAS} \rangle = (\mathbf{Image} + \mathbf{sky} \times (1 + \mathbf{fringe}) + \mathbf{tbe}) \times \mathbf{otv} \times \mathbf{qe}$$

must then be corrected for the (multiplicative) variations of sensitivity, due to both quantum efficiency and optical transmission variations. The quantum efficiency of the camera is never perfectly uniform. Pixel-to-pixel variations are expected, due to imperfections in the coating, variable thickness, small variations in the pixel area. The non-uniform response or illumination implies a non-standard relation between intensity of the source and counts detected along the camera. To overcome this problem, the raw counts must be rescaled to a common mean quantum efficiency. In principle, this can be easily done by exposing the CCD to a uniform (*flat-field*) intensity source, for the appropriate integration time. In practice, the flat-field correction is the most difficult and critical step. First, it is not trivial to observe a sufficiently uniform source, and moreover the quantum efficiency variations are wavelength dependent. There are basically two different approaches: the observation of a screen inside the dome (dome flat) or the observation of the sky at the twilights. Both ways give high S/N images, with the drawback that the spectrum of the screen or the twilight sky can significantly differ from the dark night sky (telluric emission lines). To solve this, frames of empty fields taken during the night may supply the right solution. However, the low signal level of the dark sky requires long exposure times, and indeed it is almost impossible to obtain high S/N night flat unpolluted by astronomical sources. The "best" possible flat-field is usually made with a composition of these three approaches, basically with a median combination of dome, twilights and scientific images (*super-flat field*). Even more complicated techniques, based on wavelets transformations, are used. The removal of the flat-field results in

$$(\mathbf{Raw} - \langle \mathbf{BIAS} \rangle) / \langle \mathbf{FLAT} \rangle = (\mathbf{Image} + \mathbf{sky} \times (1 + \mathbf{fringe}) + \mathbf{tbe})$$

where the  $\langle \mathbf{FLAT} \rangle$  is the median flat frame, corrected for additive bias effect, and normalized according to its mean value.

Usually, the thermal emission from the telescope is negligible, and the

fringing pattern appears only at longer wavelengths ( $R$  and  $I$  bands). Since the fringing, as well as other spurious contributions to the background, can be treated as an additive effect, a *SUPER-SKY* filter can be built with a median superimposition of many (say at least 10) background-limited, offset, empty images. The last step yields to

$$\mathit{Image} = (\mathit{Raw} - \langle \mathit{BIAS} \rangle) / \langle \mathit{FLAT} \rangle - \langle \mathit{SUPER-SKY} \rangle$$

Where now Image is the astronomical image ready for the photometric analysis.

It is important to mention other two quantities, that do not directly affect the error balance of the measures, but play an important role in the quality of the signal.

**Readout noise** : that is the electronic noise associated due to the output amplifiers. This cannot be eliminated from the measurement process.

**Gain** : is the conversion factor that transforms the electrons recorded in the CCD into ADU (Analogic to Digital Units), or counts.

These quantities do not directly affect the measurements, but play an important role in defining the threshold for the search of astronomical sources.

## 2.2 Stellar photometry: DAOPHOT and ALLFRAME

The basic problem that any software devoted to accurate stellar photometry has to solve can be summarized in two questions: how to recognize stellar-like sources? how to fit the two-dimensional distribution of light of each source, accounting for the contribution of the local background and the contamination by nearby objects? In this work we made an extensive use of DAOPHOT (Stetson, 1987), and its last evolution ALLFRAME (Stetson 1994). DAOPHOT is by no means the most popular software package for stellar photometry. It was developed by Peter B. Stetson at the Dominion Astronomical Observatory more than twenty years ago, and has undergone a continuous evolution and sophistication. DAOPHOT identifies the brightness peaks in the frame, performs synthetic aperture photometry, and tries to estimate an accurate PSF. Stand alone programs (ALLSTAR and eventually ALLFRAME) are then used to perform accurate PSF-fitting photometry of the stellar sources.

Here we present in some more details the single steps of a typical run of DAOPHOTII/ALLFRAME.

- **Identification of the stellar sources:** the image is scanned pixel by pixel and the brightness peaks are detected and estimated. A threshold must be defined in order to choose a level of significance of the brightness enhancement. This threshold depends on the read out noise and gain of the camera, and the mean sky value. These quantities are used to define

the random error per pixel, and a scaling factor decided by the user fixes the threshold for the star search. This is performed by the task *FIND*, who performs a rough estimate of the centroid and flux of the stars. To avoid that non-stellar objects (extended sources, cosmic rays, cosmetic defects) are included in the catalogue, DAOPHOT defines two shape parameters, the *sharpness* and the *roundness*, which are used for a first selection of the sources.

- **Aperture photometry** : this is the simplest and in principle most correct technique for doing photometry. The total number of photons (ADUs) are just counted in a fixed circular aperture centred on the star. The contribution of the local sky background can be estimated in a circular annulus around the object, and under the assumption that the spatial scale variation of the background are smaller than the aperture, it can be subtracted. There are two obvious drawbacks affecting this approach: (1) the crowding, that makes star profile overlap, so that its very difficult to take into account the contribution of nearby objects; (2) the measurement of faint stars, characterized by a very limited number of counts, is dominated by the background error, fluctuations and statistics. The task *PHOT* performs aperture photometry on all the objects detected, estimating the flux into a series of annuli of increasing radius, defined by user.

- **Modeling the PSF** : Once the aperture photometry has been performed, an accurate selection of stars used to model the PSF is done. This has been an important part of this thesis work, and will be discussed in the next section.

- **PSF-fitting: ALLSTAR** : ALLSTAR is program that performs PSF-fitting photometry on a single astronomical image, provided that aperture photometry and the PSF model by DAOPHOT are available. ALLSTAR tries to exploit all the information available, performing, as the name itself suggests, a simultaneous fit of all the sources. During every iteration, it subtracts all the stars from a working copy of the image according to the best estimates of position and magnitude of each object, computes the increments to the positions and magnitude of the subtraction residuals around each position, and then check each star to see whether it has converged or not. When a star has converged, it is permanently subtracted from the working image and the results saved. A non-linear least square fitting technique is applied to the derive the parameters of each object. ALLSTAR writes out also the final subtracted image, which can be visually inspected in order to:

- (1) check the quality of the fit;
- (2) look for any faint object lost or discarded.

At this point it can be very useful to run the FIND/PHOT process in order to recover all these stars, and run ALLSTAR again with the most complete list. This iterative procedure can be useful not only to measure faint stars, but also to improve the measurements of bright objects contaminated by

nearby faint sources.

- **Stacking the information** : Once that all the images have been reduced with ALLSTAR, a single catalogue containing position and magnitude for each star detected is available for each frame. DAOMATCH and DAOMASTER are two programs that estimate the coordinate transformations and allow to rescale all the catalogue on a single coordinate system. Once that all the lists are rescaled, it is possible to build the master list including all the objects of all the frames (and indeed it is routinely used to group all the lists in each photometric band, create the catalogue with weighted mean magnitudes and then use these to plot the color-magnitude diagrams). DAOMASTER output is basically a table which includes, per each image, the coefficients of the geometrical transformation to rescale the stars of individual images to the reference one.

- **ALLFRAME**: The last evolution of DAOPHOT is ALLFRAME. If ALLSTAR tries to exploit all the information available in a single image, ALLFRAME works simultaneously on all the stars in all the images available, independently on the filter, instrument, exposure time or any other parameter. The basic idea is the following: if I have many frames, and for each frame I already estimated the PSF, and if accurate coordinate transformations are available, I can use the same list of stars to fit the same object simultaneously on all the frames. After running DAOPHOT/ALLSTAR/DAOMASTER, ALLFRAME exploits all the information available for the best fit and the stellar parameters determination. ALLFRAME starts with the master list of stars, which are in the (x,y) system of the reference image, inverts the coordinate of each star in each frame, and performs local fit using the individual PSF. By applying non-linear least squares fitting technique, during every iteration a new estimate of the position and magnitude of each stars is provided. The position is rescaled in the reference frame, and then averaged. This ensures that, in case the transformations are accurate enough, the centroid of the stars is known with great precisions. This is probably the key point of this package: the accuracy in the centroid determination allows an optimal fit of stellar profile, which ensure precise estimates of the magnitudes. Moreover, by using the same list of stars for all the frames, it is possible to reach a deeper limit magnitude, in the sense that the knowledge *a priori* of the existence of a star in a specific position makes possible to fit it even if the S/N ratio is very poor, and therefore the fit on the individual image has failed. A useful approach to build the master list is to stack all the images in a median frame, and perform the search for individual stars on it. The S/N ratio of faint objects is raised, making their detection much simpler. Figure 2.2 shows an example of PSF-fitting by ALLFRAME on a Carina dSph image.

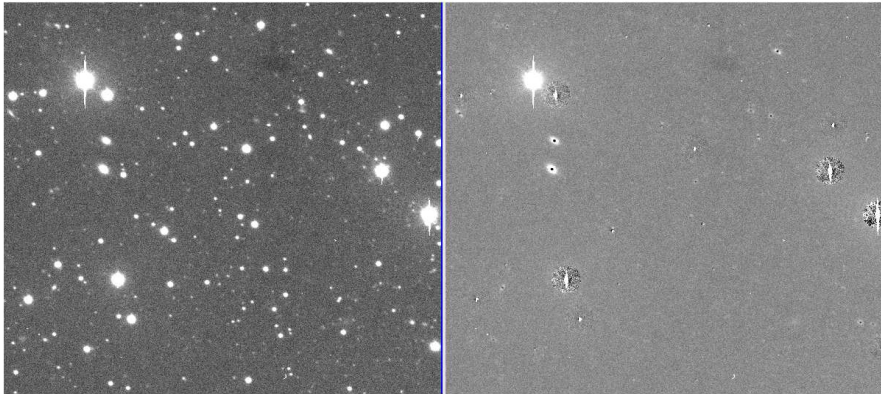


Figure 2.2: Comparison between a Carina frame and the subtracted image after the ALLFRAME fit. Note that the code fits the saturated

### 2.3 Recipe for a good PSF

The PSF-fitting algorithm of ALLFRAME requires a good estimate of the individual PSFs. The selection of the PSF stars is the crucial point of this process. DAOPHOT model the PSF with a mixed technique, in the sense that uses an analytic formula plus a numerical map of the residuals to take into account the spatial variations along the frame. Given the list of selected stars, the *PSF* task in the DAOPHOT environment fits a simple analytic formula with non-linear least squares. Then, all the observed residuals from the fit are interpolated on a common grid and averaged into a numerical look-up table of residuals.

I developed automatic procedures that select the PSF stars, and the most important criteria adopted are:

- PSF stars must be bright, unsaturated, and with good shape parameters;
- stars must be *isolated*, that is no object brighter than a user selected threshold must be too close to the PSF star. In this case "too close" means that the user can select a minimum distance, usually 5 or more times the FWHM of the stellar image;
- stars must uniformly sample the field of view of the CCD

This last point is particularly important. Modern cameras are often designed to observe wide areas of the sky and the changes in the PSF shape along the field must be carefully taken into account. The DAOPHOT algorithm to estimate the PSF allows to introduce a linear, quadratic, or cubic

dependency on the position. If a sufficient number of uniformly distributed stars are used to build the PSF, the shape variations can be estimated and taken into account during the fit process. Otherwise, unpredictable random errors may be introduced in the measurements. We performed a large number of tests using different analytic functions and different spatial dependencies. The best photometry, i.e. the best CMDs, were obtained with a linearly variable Moffat PSF.

The procedure iteratively works to select the best stars according to the previous criteria. After a first rough and blind estimate of the PSF, a first fit is performed on the entire catalogue using ALLSTAR. This is because the PSF photometry allows a better determination of the centroid of the stars, and of the shape parameter (*sharpness*).

All the selections are then performed on the resulting catalogue. Stars are grouped on a grid of squares according to their position on the frame. The best star is picked up in each square, which is typically dimensioned to  $128 \times 128$  px<sup>2</sup>, selecting the brightest and most isolated star, with the best sharpness and photometric error. This ensures that the entire field of view is scanned and should contribute to the PSF. At the very end, a second iteration of ALLSTAR is performed generating the final catalogue of the frame. In general, depending on the crowding and the total number of stars, the procedure ends up with  $150 \pm 50$  stars. The CPU time required for a single PSF is critically dependent on the number of stars: the bottleneck is represented by the double ALLSTAR iteration, because all the other selections requires a few seconds on average.

## 2.4 Photometric calibration of wide field imagers: the example of Carina

The calibration to a standard photometric system is a crucial point to obtain reliable results. Each instrument (telescope + sensor) is a unique device characterized by its own spectral response, and every single observation is carried out under different atmospheric conditions. This means that raw measurements cannot be directly compared, but must be rescaled to a common standard system. This is usually done by observing standard stars at different epochs during the night(s) of observation, in order to estimate the extinction coefficients of the night as well as the calibration curve of the instrument. Standard stars catalogue have been published by Landolt (Landolt (1983), and Landolt (1992) for CCD observations). More recently, Stetson (2000) made available a new set of standard fields, which are constantly updated and increased. All the data are public on the web (<http://cadwww.hia.nrc.ca/standards>).

In this thesis we will present photometric data of the Carina dSph galaxy and the Galactic Globular Cluster  $\omega$  Centauri. These two stellar systems

present completely different structural parameters, and require a rather different observational approach.

Strictly speaking, from a purely observational point of view, the main difference is that Carina is a loose and wide object, covering a huge area in the sky, while  $\omega$  Cen is a compact GC where the crowding is the dominant source of error. Both objects are characterised by a huge tidal radius, which makes the wide field of view necessary to sample a sizable fraction of their stellar content. Our strategy was to use wide field CCD to observe Carina (the 2.2m ESO and the 4m CTIO telescopes), and the highest spatial resolution to resolve the inner part of  $\omega$  Cen. Both ground based and space data of  $\omega$  Cen are presented. All the details of the data sets will be discussed in the following chapters. In the next section we discuss the calibration of wide field imagers data of the Carina dSph, and we will refer to two different data sets, namely the 2.2m ESO and the 4m CTIO data sets, both collected in January 2000.

The advent of wide field cameras has introduced new problems that go beyond the standard techniques. Non-uniform illumination of the camera may not be corrected by standard flat-fielding procedures. The subtle resulting effect is that the magnitude of an objects depends on the position on the frame, and the difference from an edge to the other of the camera can be as high as 0.08mag. In particular, the WFI camera mounted on the 2.2m suffers of this problem (Manfroid & Selman 2001; Koch et al. 2004). To solve this problem, we undertook a careful plan of observations devoted to characterize and correct this effect. At the same time we wanted to study the MOSAIC camera on the 4m CTIO telescope to eventually disclose similar behaviour. Moreover, other data sets have been collected with these two different cameras during many observing runs in the last five years. We briefly discuss the procedure adopted to homogeneize all the data to a common standard system.

### 2.4.1 The calibration strategy

The guide line of the project can be summarized as follows:

- calibration of the MOSAIC camera; this means that we need to collect plenty of data of standard stars spread across the field-of-view;
- creation of a set of local standards in the central region of Carina;
- use these to calibrate the WFI data (and all the other data sets).

As already mentioned, the meaning of "calibration" in this context goes beyond the standard color curve. We investigated all the possible trends present in the standard stars, against color, magnitude and the position on the frame.

We decided to use the standard field Selected Area 98 (SA98, RA= 06<sup>h</sup>

52<sup>m</sup> 07.90<sup>s</sup>, DEC=−00° 19′ 13.9″, see tab 2.1), because is one of the most populated fields in the Stetson’s archive, with several hundreds of stars in the *U,B,V,R* and *I* bands. Moreover, and crucial for our purpose, the area covered by standard stars fully sample the field of view of the instruments. This means that standard stars are present in all the chips, and we can analyze and estimate and absolute calibration of each chip. Data were col-

field name	RA (h)	DEC (deg)	filter,	exp. time (sec)	airmass
SA 98-B	06:51:10.30	-00:11:43.10	B	6	1.165
SA 98-B	06:51:10.39	-00:11:43.10	V	3	1.163
SA 98-C	06:51:50.02	-00:11:41.89	V	3	1.160
SA 98-C	06:51:49.92	-00:11:41.89	B	6	1.159
SA 98-D	06:52:29.90	-00:11:40.69	B	6	1.158
SA 98-D	06:52:29.90	-00:11:41.59	V	3	1.158
SA 98-E	06:53:00.06	-00:11:41.20	V	3	1.155
SA 98-E	06:53:00.12	-00:11:40.89	B	6	1.155
SA 98-G	06:51:15.04	-00:30:41.39	B	6	1.151
SA 98-G	06:51:15.07	-00:30:41.19	V	3	1.150
SA 98-H	06:51:49.94	-00:30:40.50	V	3	1.150
SA 98-H	06:51:49.97	-00:30:41.19	B	6	1.150
SA 98-I	06:52:30.01	-00:30:39.89	B	6	1.151
SA 98-I	06:52:29.98	-00:30:40.60	V	3	1.151
SA 98-J	06:53:10.02	-00:30:40.60	V	3	1.152
SA 98-J	06:53:10.12	-00:30:41.29	B	6	1.152
SA 98	06:52:17.39	-00:19:42.70	B	6	1.933
SA 98	06:52:17.34	-00:19:43.79	V	3	1.958
Carina	06:41:48.25	-50:58:15.20	B	120	1.077
Carina	06:41:48.50	-50:58:14.00	V	60	1.079
Carina-C	06:44:10.48	-50:43:59.40	B	120	1.078
Carina-C	06:44:10.54	-50:43:58.19	V	60	1.081
Carina-D	06:39:30.43	-51:17:59.20	B	120	1.089
Carina-D	06:39:30.33	-51:17:58.20	V	60	1.090
Carina-ex	06:41:38.50	-51:58:15.59	B	120	1.129
Carina-ex	06:41:38.45	-51:58:14.30	V	60	1.134

Table 2.1: Log of the observations for the calibration run, on Dec 31<sup>st</sup>, 2002.

lected on Dec 31<sup>st</sup>, 2002. The night was photometric, and 9 *B,V* couples were collected. Standard IRAF routines were applied for the prereduction, and then the images were reduced with DAOPHOTII. Aperture photometry was performed, with an aperture of 3px. The first step of the calibration requires the correction for the atmospheric extinction. Images were taken at different epochs during the night, and this allowed us to estimate the

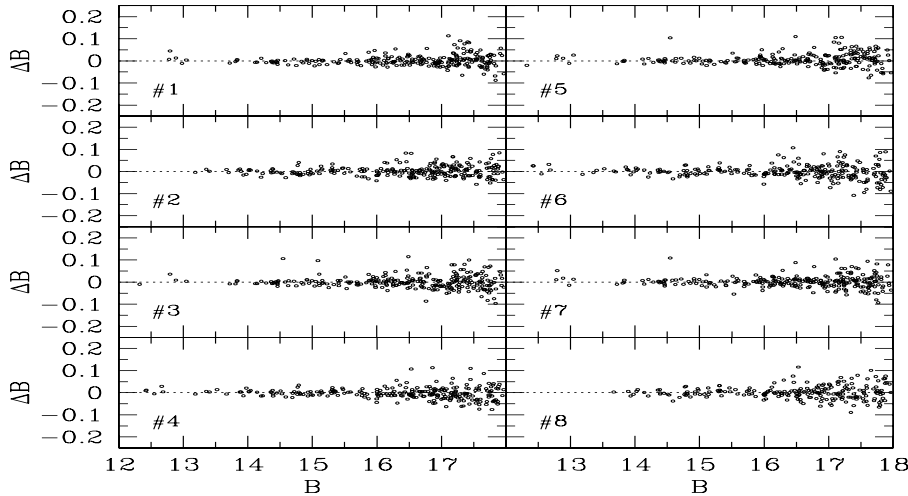


Figure 2.3: Residuals of the calibration applied to the standard stars.  $\Delta B$  is plotted as a function of the  $B$  magnitude.

extinction coefficients for both bands. The values we determined ( $\chi_b=0.25$  and  $\chi_v=0.13$ ) are in good agreement with the mean values of the site, in the summertime. Once corrected for exposure time and the atmospheric effects, we estimated the color curve for each of the eight chips. After applying the curves, we studied the residuals (standard  $v_s$  calibrated) as a function of the position on the chip. We did not detect any evident trend within the calibration error ( $\pm 0.02\text{mag}$ ). The lack of positional effect suffered by MO-SAICII@Blanco telescope can be possibly explained by the different optical setup of the two cameras. While the MO-SAICII is a prime focus instrument, the WFI is mounted at the Cassegrain focus of the 2.2m telescope. Moreover, since the telescope was not built to host a wide field imager, the optical path was modified introducing a focal reducer. The positional effect seems to be stable with time, is wavelength dependent, and survives to standard dome+sky flat field techniques. The most probable explanation is that scattered light is present within the telescope and causes a non-uniform illumination of the focal plane.

We report here the eight calibration curves:

$$\text{chip 1: } B = b + 0.073 + 0.083 * (b - v) - 0.072$$

$$V = v + 0.468 - 0.045 * (b - v) - 0.077$$

$$\text{chip 2: } B = b + 0.057 + 0.096 * (b - v) - 0.072$$

$$V = v + 0.473 - 0.043 * (b - v) - 0.077$$

$$\text{chip 3: } B = b + 0.059 + 0.087 * (b - v) - 0.072$$

$$V = v + 0.472 - 0.047 * (b - v) - 0.077$$

$$\text{chip 4: } B = b + 0.045 + 0.092 * (b - v) - 0.072$$

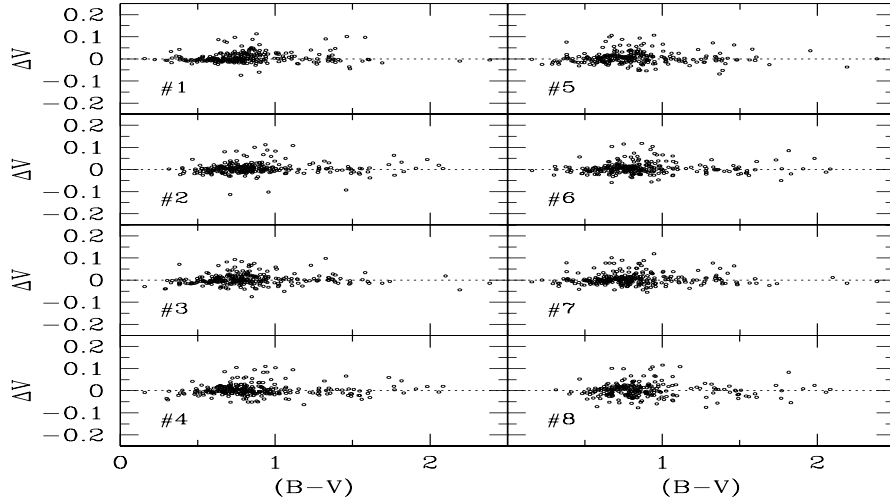


Figure 2.4: Same as 2.3, but against the color

$$\begin{aligned}
 & V = v + 0.445 - 0.040 * (b - v) - 0.077 \\
 \text{chip 5: } & B = b + 0.068 + 0.091 * (b - v) - 0.072 \\
 & V = v + 0.495 - 0.048 * (b - v) - 0.077 \\
 \text{chip 6: } & B = b + 0.049 + 0.103 * (b - v) - 0.072 \\
 & V = v + 0.479 - 0.044 * (b - v) - 0.077 \\
 \text{chip 7: } & B = b + 0.059 + 0.098 * (b - v) - 0.072 \\
 & V = v + 0.491 - 0.049 * (b - v) - 0.077 \\
 \text{chip 8: } & B = b + 0.061 + 0.092 * (b - v) - 0.072 \\
 & V = v + 0.465 - 0.042 * (b - v) - 0.077
 \end{aligned}$$

Where  $B, V$  are the standard magnitude and  $b, v$  are the instrumental measurements corrected for atmospheric extinction and normalized to an exposure time of 1sec. The last additional term is the aperture correction that rescales the photometry to an infinite aperture.

During the same night 3  $B, V$  couples of the Carina central region were collected. The same prereduction as well as reduction strategy was applied. The three measurements were averaged and then calibrated according to the previous curves. The resulting catalogue represents the first sample of local standards. In principle, these sample could be used to calibrate any other data set of this field. Unfortunately, these data are not deep enough to reach with high S/N ratio the bluest HB Carina stars. The calibration curves were obtained using bright stars in the color range spanning from  $B - V = 0.5$  to  $B - V = 1.8$ . This means that we had to extrapolate our relations to the bluest HB Carina stars. However, since the relation is fairly linear, no evident bias is expected in the measurements (this will be

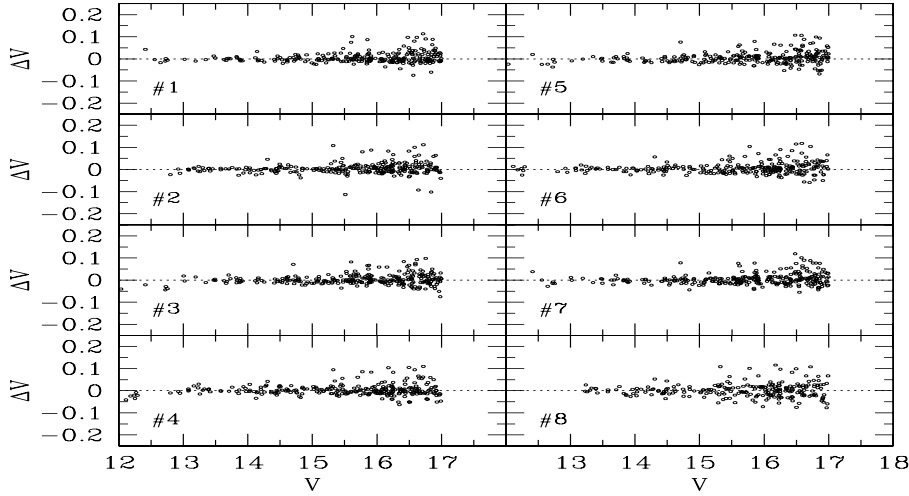


Figure 2.5: Same as 2.3, but for the  $V$  band

confirmed *a posteriori*, see below).

To overcome this problem and to obtain a more complete set of local standard, we calibrated the 2000 4m CTIO data set using this set of local standards. Each chip was independently calibrated, and we found the following relations:

$$\text{chip 1: } B = b + 6.336 + 0.095 * (b - v)$$

$$V = v + 6.142$$

$$\text{chip 2: } B = b + 6.332 + 0.108 * (b - v)$$

$$V = v + 6.138$$

$$\text{chip 3: } B = b + 6.334 + 0.110 * (b - v)$$

$$V = v + 6.137$$

$$\text{chip 4: } B = b + 6.340 + 0.111 * (b - v)$$

$$V = v + 6.147$$

$$\text{chip 5: } B = b + 6.193 + 0.107 * (b - v)$$

$$V = v + 6.092$$

$$\text{chip 6: } B = b + 6.318 + 0.107 * (b - v)$$

$$V = v + 6.132$$

$$\text{chip 7: } B = b + 6.319 + 0.116 * (b - v)$$

$$V = v + 6.142 + 0.015 * (b - v)$$

$$\text{chip 8: } B = b + 6.319 + 0.101 * (b - v)$$

$$V = v + 6.140 + 0.012 * (b - v)$$

Note that the color term for the  $V$  band is very small, and in most cases null, because the passband of this filter is very similar to the Johnson standard filter. This data set contains  $\approx 70,000$  stars. To verify that our

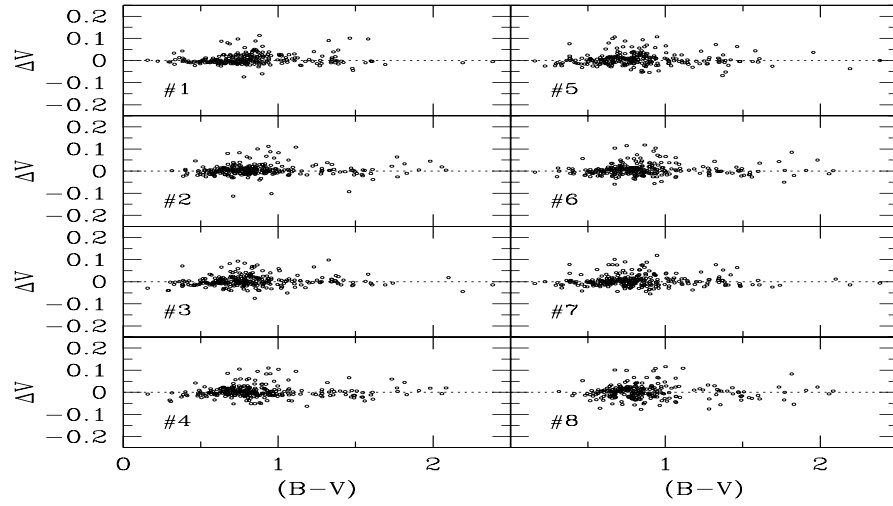


Figure 2.6: Same as 2.4, but for the V band

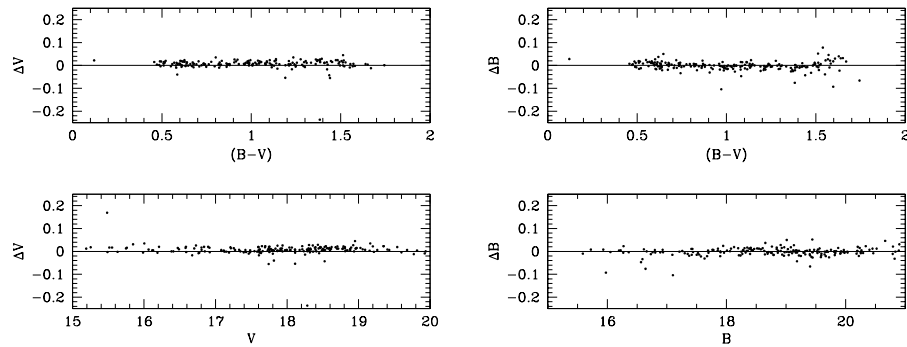


Figure 2.7: Comparison with the standard stars in common with the Stetson's database.  $\Delta V$  and  $\Delta B$  are shown as a function of both color and magnitude. No trends either offsets are present within the errors.

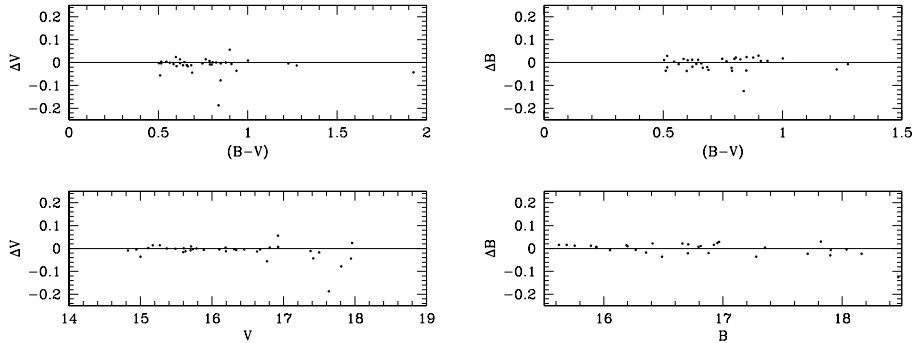


Figure 2.8: Same as 2.7, but the comparison has been made with local standard observed with the 0.9m CTIO on Dec 31<sup>st</sup>, 2000.

calibration is robust, we performed two independent *a posteriori* absolute checks.

The first test was performed using local standards available from the Stetson’s archive. We checked any residual against the magnitude and color and the result is shown in fig. 2.7. No trend is evident within the uncertainty, and notably the comparison is good at the bluer colors also ( $B-V \approx 0$ , but based on one standard star only).

The second check was performed using absolute  $B$  and  $V$  band photometry of a few dozens of stars located across the Carina center, secured during the night of December 31<sup>st</sup>, 2000 using the 0.9m CTIO telescope. Even if in this sample there are no stars bluer than  $B-V \sim 0.5$ , in the range in which the comparison is possible no trends appear with the magnitude nor the color, within the calibration error (see fig. 2.8).

To confirm the consistency of this double check, we cross-correlated the Stetson’s local standard with the 54 stars observed with the 0.9m. Once again, no trends appear between the two samples. This is very important, because it means that the two sets of standards are in a homogeneous photometric system, and therefore the calibration of our data can be considered fairly robust.

We adopted the calibrated catalogue as ”*the*” catalogue of local standard, and we used this to calibrate the 2.2m data sets and all the outer fields observed in subsequent runs (see sect. 2.5 and 3.2.5).

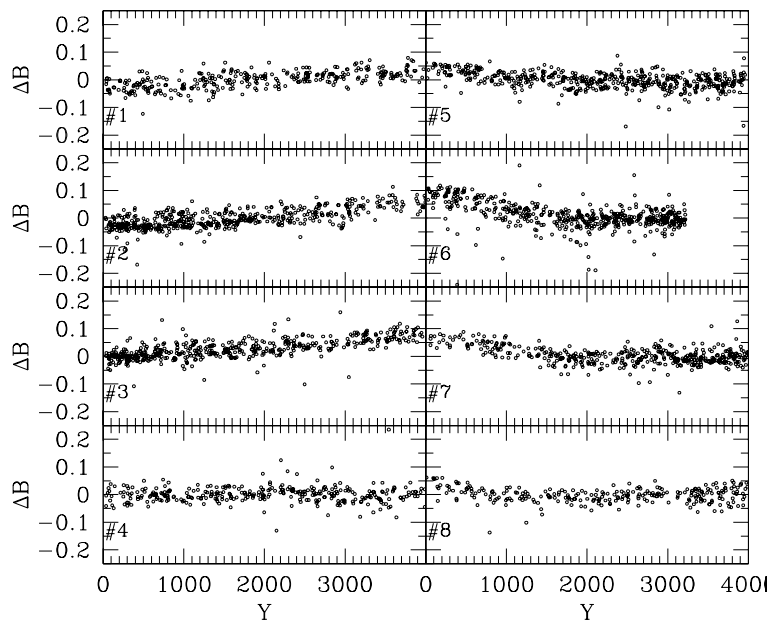


Figure 2.9:  $\Delta B$  as a function of the Y coordinate. A non-linear trend is evident, and a polynomial fit was adopted to remove this spurious effect.

### 2.4.2 Positional effects of the Wide Field Imager

To calibrate the 2.2m Jan 2000 data set we selected all the stars brighter than  $V=21$ . We ended up with few hundreds of stars per chip, and we could study both the color and the positional effects. Measurements are first rescaled to an exposure time of 1s and corrected for the atmospheric extinction. This means that the calibration recipe given below can be applied to any 2.2m data set in these bands, provided that the photometry is rescaled to an infinite aperture, at 1s and outside the atmosphere.

Each chip has been treated separately, and we adopted a two-step strategy. We estimated a first color curve and applied it. We then studied the residuals (calibrated  $v_s$  standard magnitude) as a function of the position on the chip. Once estimated and corrected the positional effect, we fitted once again the color curve. This procedure allows to disentangle the two effects, and reduce the scatter introduced by the positional trend when estimating the color curve. This strategy works under the assumption that the two corrections are independent, and there is no reason why this should not be the case. Only in the very unreasonable case that all red stars are in one side of the chip and all the blue ones in the opposite side this assumption is not valid.

Fig. 2.9 and 2.10 show the difference between standard stars and our

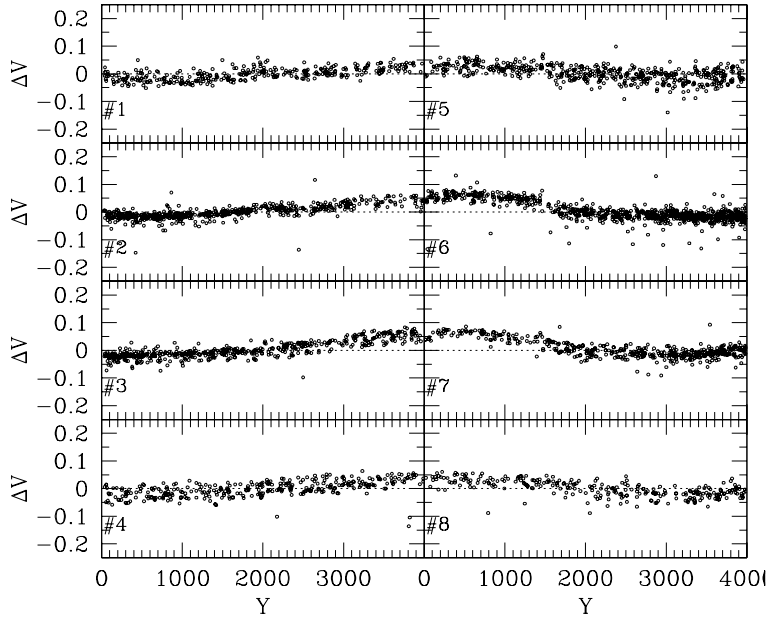


Figure 2.10: Same as fig. 2.9, but for the  $V$  band

stars calibrated with a color curve only, for the  $B$  and  $V$  band plotted as a function of the  $Y$  coordinate. The trend with the position is evident, and non-linear. The trend is present in all the 8 chips as a function of the  $Y$  coordinate, while a trend with the  $X$  has been detected only in the four external chips. We corrected this effect by fitting the  $\Delta(mag)$  vs  $X/Y$  with second or third order polynomials. Fig. 2.11 shows an example of color dependency after correcting for the positional effect. The relations used to fit these residuals are fourth or fifth order polynomials. The reason of this complicated trend with the color is probably due to the shape of the filters, which are quite different from the standard Johnson ones. Fig. 2.12 shows the residuals for the  $B$  band after the positional and color effects have been removed.

## 2.5 Calibration of the external fields

The calibration of the external fields (see sect. 3.2.5 and fig. 3.20) relies on the local standards of the central field. However, only two of the outer regions we observed (see sect. 3.2.5) are partially overlapped with the central pointing, and no direct calibration with local standard was possible. However, some of them (namely fields  $C$ ,  $D$ ,  $E$ ) were observed during the

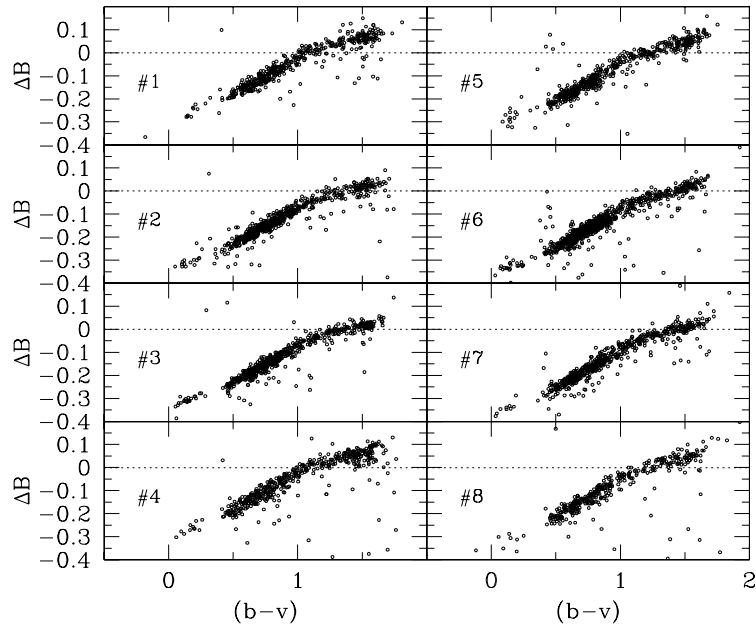


Figure 2.11: Color dependency of stars after correcting the positional effect. The trend is non-linear, and this is probably due to the fact that the  $B$  filter of the 2.2m ESO telescope presents a quite different passband with respect of the standard Johnson filter.

calibration night of Dec 31<sup>st</sup>, 2002, and the same calibration curves can be applied. For most recent observations (fields  $\alpha$ ,  $\beta$ ,  $\gamma$ ), a few images of the central field were collected during the same run, and the local standards were used to derive the calibration of each night.

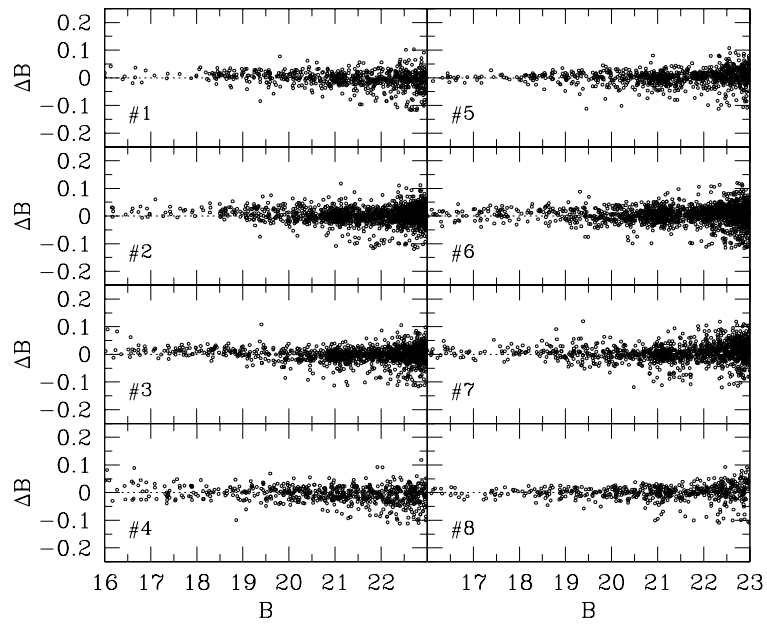


Figure 2.12: Example of residuals after the color and position corrections were applied.  $\Delta B$  is plotted as a function of the  $B$  magnitude.



## Chapter 3

# The Carina dSph galaxy

### 3.1 Overview

The Carina dSph galaxy was discovered in 1977 by Cannon et al. (1977) by visual inspection of ESO/SRC Sky Survey plates (see fig. 3.1). Carina presented all the attributes of dwarf spheroidal galaxies: low surface brightness, low central concentration, no evidence of gas nor dust. Carina appeared as a low surface density object, very difficult to pinpoint from the foreground Galactic star contamination. The large angular extent estimated and the faintness of stars excluded the hypothesis that it could be a Galactic Globular Cluster. However, by comparing the star counts in blue and red plates, Cannon et al. (1977) noticed an excess of blue objects, due to blue HB stars close to the limit magnitude in the blue plates, and undetected in the red ones. They could estimate the HB mean magnitude, and inferred a distance of  $170 \pm 50$  Kpc. This demonstrated that Carina was not only a member of the Local Group, but also a nearby satellite of the Galaxy.

The first clues on the Star Formation History (SFH) of Carina came from the discovery of two carbon stars, which revealed the presence of an intermediate-age population (Cannon et al. 1981). This result was confirmed by Mould et al. (1983, fig. 3.2), who collected deep *BV* CCD photometry. They disclosed the existence of a well-populated red Horizontal Branch (HB), and estimated the Turn Off (TO) magnitude to be  $V \approx 23$  suggested an age between 6 and 9 Gyr, thus supporting the hypothesis that the bulk of Carina stars are intermediate-age objects. However, Saha et al. (1986) detected a sizable sample of RR Lyrae stars. This evidence can be explained with the presence of an old population of stars ( $\geq 10$  Gyr). Mighell (1989), on the basis of deep, *V*, *R* photometry reported the existence of two different Turn-Offs, separated by  $\approx 0.6-0.8$  mag. In particular, Mighell (1989) estimated that the first old star formation episode occurred about 13-16 gyr ago, accounting for the  $\approx 17\%$  of the Carina stars, while the bulk of the stellar content was produced in a more recent, dominant burst 6-9 Gyr

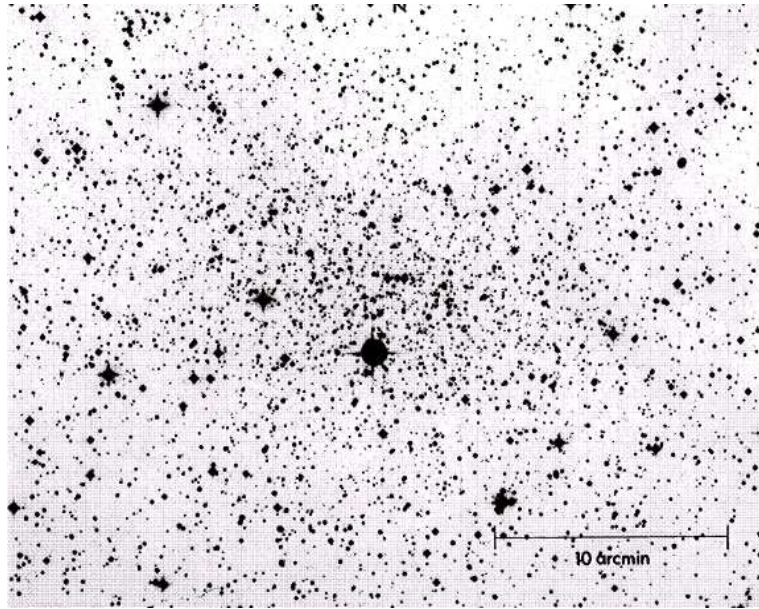


Figure 3.1: Fig. 1 from Cannon et al. (1977), showing the Carina centre. It appears as a loose, sparse cluster. The bright object close to the center is the foreground star SAO 234657.

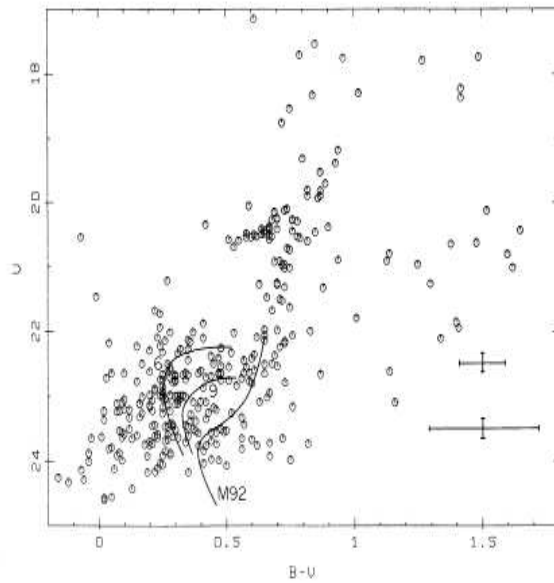


Figure 3.2: The CMD by Mould et al. (1983). The well populated red HB, and the discovery of two carbon stars supported the idea that the dominant population in Carina is made by intrermediate-age stars.

Table 3.1: Positional, photometric and structural parameters of the Carina dSph.

Parameter		Ref. <sup>1</sup>
$\alpha$ (J2000)	06 41 37	1
$\delta$ (J2000)	-50 58 00	1
$M_V$ (mag) <sup>2</sup>	-9.3	1
$r_c$ (arcmin) <sup>3</sup>	$8.8 \pm 1.2$	2
$r_t$ (arcmin) <sup>4</sup>	$28.8 \pm 3.6$	2
$e$ <sup>5</sup>	$0.33 \pm 0.05$	2
$\Theta$ (deg) <sup>6</sup>	$65 \pm 5$	2
$\sigma_V$ (km s <sup>-1</sup> ) <sup>7</sup>	$6.8 \pm 1.6$	3
$[Fe/H]$ <sup>8</sup>	$-2.0 \pm 0.02$	4
E(B-V) <sup>9</sup>	$0.04 \pm 0.02$	1
$(m - M)_0$ (mag) <sup>10</sup>	$20.03 \pm 0.09$	1

<sup>1</sup> References 1) Mateo 1998; 2) Irwin & Hatzidimitriou 1995;

<sup>3</sup>) Mateo et al. 1993; 4) Smacker-Hane et al. 1999

<sup>2</sup> Total Visual magnitude

<sup>3</sup> Core radius

<sup>4</sup> Tidal radius.

<sup>5</sup> Eccentricity.

<sup>6</sup> Major axis position angle.

<sup>7</sup> Stellar central velocity, dispersion.

<sup>8</sup> Metallicity.

<sup>9</sup> Reddening.

<sup>10</sup> True distance modulus.

ago. The episodic SFH of Carina was ultimately demonstrated by (Smecker-Hane et al. 1996, fig. 3.3), who showed a deep color-magnitude diagram reaching a limit magnitude of  $R \approx 24.5$ . The CMD reveals the occurrence of two distinct TOs, and two well separated Sub-Giant (SG) branches that merge in a thin unresolved Red Giant Branch (RGB). This striking feature suggests that a first star formation event took place  $\approx 11$ -13 Gyr ago, while the second occurred after a long quiescent phase roughly 3-6 Gyr ago. Moreover, they report the possible detection of an even younger stellar population formed  $\approx 2$  Gyr ago.

The complex star formation history of this galaxy poses many interesting questions related to the formation, evolution, and interaction of dwarf galaxies with bigger objects. What physical mechanism(s) can drive a similar complex picture? Is there any relations with the orbit around the Galaxy?

On the basis of deep V,I ( $V \approx 27$ ) band data collected with HST, Mighell (1997, and references therein), suggested that the very old population in Carina is a small fraction, if any, of the entire galaxy. A similar conclusion was also reached by Hurley-Keller, Mateo & Nemeč (1998). According to these authors the bulk of the stars in Carina formed in two different episodes roughly 3 and 7 Gyr ago, with the additional evidence of approximately 10-20% of very old stars with ages  $\approx 15$  Gyr. However, Hernandez, Gilmore

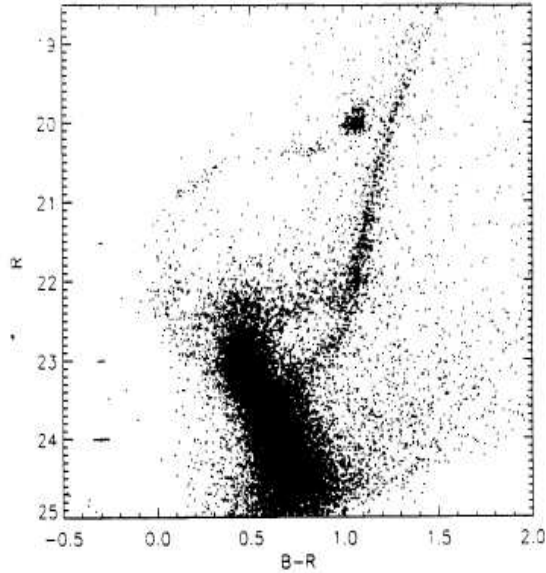


Figure 3.3: The CMD by Smecker-Hane et al. (1996). The two sub-giant branch-head are very well separated, indicating a long phase of quiescence during which Carina did not form stars.

& Valls-Gabaud (2000) on the basis of the same HST data concluded that Carina experienced three different SF episodes, namely at 3, 5, and 8 Gyr ago, with no evidence of stars older than 10 Gyr. This result has been recently questioned by Dolphin (2002) who marginally detected ( $1\sigma$  level) older stars.

### 3.1.1 The chemical enrichment history

The chemical evolution in Carina seems to have gently enriched the ISM. There is evidence, for example from the thinness of the RGB, of a small spread in metallicity between old and younger stars. This can be studied and used to infer how the stellar winds have polluted the environment, and the capability of this small system to retain the gas and form stars. However, recent spectroscopic measurements based on the Ca II triplet of 487 RGB stars (Koch et al. 2004) seem at odds with these conclusions. In agreement with previous work by Smecker-Hane et al. (1999), they estimate a mean value of  $[\text{Fe}/\text{H}] \approx -1.9$  (see fig. 3.4), and they state that the spread around this value is  $0.25dex$ , but the entire data set cover a range  $\geq 1dex$ . They suggest that the age spread is counteracted by a spread in the metal content, and that the narrowness of the RGB is a consequence of the age-metallicity degeneracy (Hodge 1989; Da Costa 1991). High resolution spectra of 5

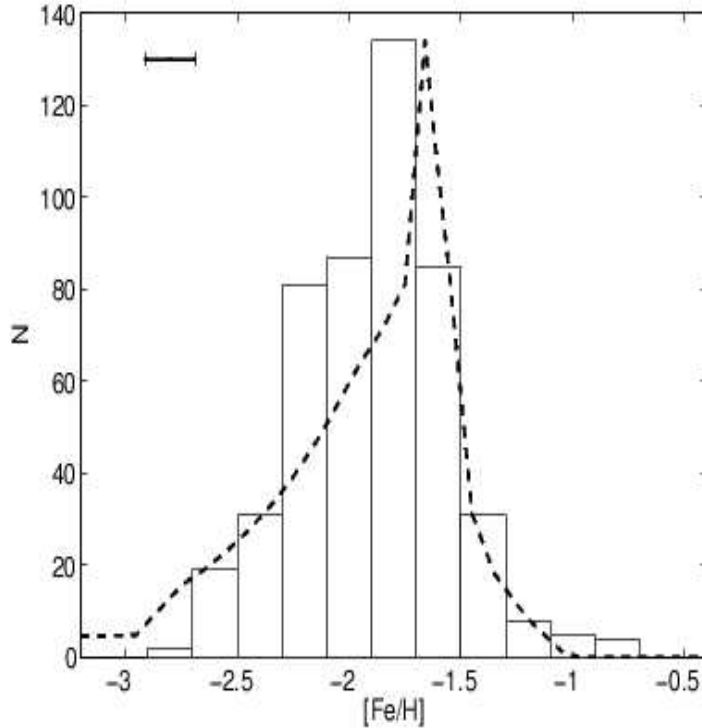


Figure 3.4: Metallicity distribution by Koch et al. (2004), obtained from the infrared Ca triplet.

giant stars (Tolstoy et al. 2003; Shetrone et al. 2003) indicate a mean metallicity of  $[Fe/H]=-1.6$ , with a spread of  $0.5dex$ .

### 3.1.2 Spatial distributions

With the exception of Draco, Ursa Minor, and Tucanae, all the nearby dSphs have witnessed a complicated SFH. It has been widely proved (Saviane, Held & Bertelli 2000; Koch et al. 2004; Tolstoy et al. 2004) that different populations within the same galaxy present different radial distributions and different kinematical properties. As a general feature, the older stars appear to be distributed in a sort of broad and diffuse "halo", while younger populations are more centrally concentrated. We will discuss the case of Carina, with both photometric and spectroscopic data.

The other debated point concerns the spatial extent of this galaxy. The first studies based on wide field photographic plates revealed the vast area covered by Carina. The estimates by Godwin (1985) suggested that Carina, as well as Draco and Ursa Minor, should be seriously affected by the Galactic tidal field. As already mentioned in chapter 1, this could play a crucial role in explaining the high  $M/L$  ratios. The tidal interaction in the outskirts of the Carina dSph has not been firmly established yet. Kuhn et

al. (1996) investigated the RR Lyrae stars distribution at distances of  $\approx 2^\circ$  from the centre, that is out to four tidal radii. They did not detect any RR Lyrae star beyond the tidal radius, but found a large surface density close to it, as if the spatial distribution of RR Lyrae stars was broader, or more clumpy, than the majority of stars.

Further support to the existence of extra-tidal stars in Carina was given by Majewski et al. (2000b). They investigated  $2.2\text{deg}^2$  around Carina, using the Washington photometric system to split RG Carina stars from foreground Galactic contaminants. This survey revealed the existence of Carina RGB stars at  $\approx 2\text{deg}$  from the Carina centre. This result was questioned by Morrison et al. (2001), who claimed that such conclusion was not reliable, since the photometric accuracy was not good enough to split the two samples.

More recently, an investigation by Walcher et al. (2003) based on data collected with the Wide Field Imager mounted on the 2.2m ESO telescope, covering an area of  $2\times 2\text{deg}^2$ , did not show any evidence of extra-tidal stars in Carina.

It is worth noting that all of the quoted investigations based their results on bright evolved stellar tracers. The problem that immediately comes up is that bright evolved stars may suffer strong statistics problems. Moreover, especially for the RGB stars, the field contamination at redder colors is a dominant source of error. In the following, we will present the result of our investigation of the outskirts of Carina, based on deep BV photometry aimed at sampling the much more numerous TO stars.

However, the detection of extra-tidal stars may not be the signature of tidal interaction with the Galaxy. It is interesting to note that recent N-body simulations in the  $\Lambda\text{CDM}$  framework (Hayashi et al. 2003; Mayer et al. 2001) suggest that the real extent of dSphs is heavily underestimated. The actual tidal radius may be a factor of 20 larger than typically assumed. The detection of Carina stars at greater distance from its centre might be the proof of such diffuse population.

### 3.1.3 Variable stars

The complex star formation history of Carina makes this galaxy a crucial object to search for and study variable stars. The existence of multiple stellar populations in the same cluster, that is at the same distance, allow us to simultaneously observe variable stars with different ages and in different stages of stellar evolution. At least three different samples of variable stars have already been detected in Carina. Saha et al. (1986) collected time series  $B$  photographic plates with the 4m CTIO telescope. They identified 58 RR Lyrae stars over an area of  $\approx 30' \times 40'$ . Both  $ab$  (fundamental pulsators) as well as  $c$  (first overtone) type RR Lyrae stars were detected.

However, Carina has experienced a dominant burst of SF 5-9 Gyr ago,

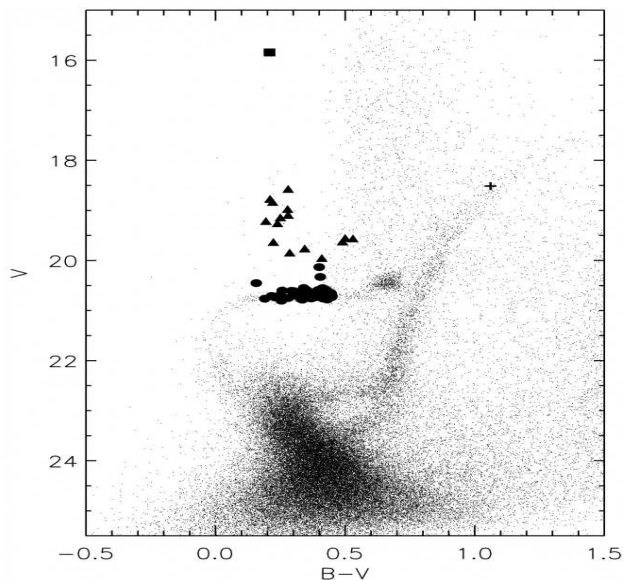


Figure 3.5: CMD diagram by Dall’Ora et al. (2003), showing the position of the variable stars detected. Filled circles show the 75 RR Lyrae stars, while the triangles indicate the Anomalous Cepheids.

and the MSTO is  $\approx 1$ mag more luminous than the TO of the old population. Interestingly enough, the upper part of the intermediate-age MS intersects the Cepheids instability strip. As a consequence, we expect to find short-period, low-amplitude intermediate-age pulsators (which we generically indicate as "Dwarf Cepheids", DCs). Mateo, Hurley-Keller, & Nemeč (1998) discovered 20 DCs, with period ranging from 0.5d to 0.9d and luminosity in the range  $V \approx 18.5 \div 20$ mag. Both fundamental and first overtone pulsators were identified. Unlike RR Lyrae stars, the pulsation mode turns out to be uncorrelated with light-curve shape, and the overtone pulsators do not show shorter periods compared with the fundamental pulsators. Using the period-luminosity relations from Nemeč, Nemeč & Lutz (1994) and McNamara (1995), they derived  $(m - M)_0 = 20.06 \pm 0.12$ , for  $E(B - V) = 0.025$  and  $[\text{Fe}/\text{H}] = -2.0$ .

It is worth noting that the same blue region of the CMD is populated also by BSs of the old population. Variable BSs are a common feature in GGc and Old Open Clusters. The variation can be intrinsic (pulsating BSs), or due to eclipses in binary systems. The study of variable BSs is important to understand the formation mechanism of these peculiar stars. Variable BSs coexist with intermediate-age TO variable stars: Carina is the ideal laboratory to study these stars, at the same distance and with the same interstellar extinction, to shed light on their formation and evolution.

A recent work by Dall’Ora et al. (2003) revised bright variable content

in Carina. The main result of this work was the discovery of 15 bone fide Anomalous Cepheids (ACs). These variables are intrinsically brighter than RR Lyrae stars and follow a Period-Luminosity (PL) relation with the less luminous ones ( $\sim 0.5$  mag above the RR Lyrae level) having shorter periods ( $P \sim 0.3$  day) and the most luminous ones ( $\sim 2$  mag brighter than RR Lyrae stars) longer periods ( $P \sim 2$  day). Concerning their evolutionary status, there is a general consensus that they are metal-poor central He-burning structures with mass larger than  $1.3M_{\odot}$ , but their origin (single young stars or old merged binary systems) is still debated (Bono et al. 1997, and references therein). They are almost absent in GGCs (except one in NGC 5466 and two suspected candidates in  $\omega$  Centauri), whereas they have been found in all dSphs that have been searched for variable stars. The presence of these variables might be taken as indicative of an underlying intermediate-age population or at least of the presence of a significant Blue Straggler component. In the former case, the ACs detected would support the detection (Monelli et al. 2003) of a recent star formation episod occurred  $\leq 1$  Gyr ago. If this is true, it would be possible to study, in the same cluster, variable stars populating the Cepheid instability strip from  $M_V \approx -2$  down to  $M_V \approx 3$ . This means that variable stars during the He-burning phase (RR Lyrae, Anomalous Cepheids) and the H-burning phase (oscillating BSs, dwarf Cepheids) can be observed in the same system.

### 3.2 The Carina Project

The work presented in this thesis on the Carina dSph galaxy is part of a large program started at the Rome Observatory in 1999. The so-called "Carina Project" is a long-term project aimed at studying the static and variable stars in the Carina dSph. Both photometric as well as spectroscopic techniques were adopted.

As already discussed in sect. 2.4, wide field imagers are mandatory to observe a sizable fraction of nearby, low-central density dwarf spheroidal galaxies. In the last decade, the advent of wide-field imagers available on medium-class (2-4m) telescopes, as well as the multi-object spectrographs on 8m class telescopes, has given new opportunities to the study of nearby dSphs.

The Carina core and tidal radii are  $8.8'$  and  $28.8'$ , respectively (see tab. 3.1). The ideal instruments located in the southern emisphere to observe this galaxy are the Wide Field Imager available at the 2.2m ESO telescope (La Silla), and the MOSAIC II Camera mounted at the prime focus of the 4m CTIO telescope (Cerro Tololo). The field of view of these instruments (see tab. 3.2 for details) is  $\approx 30' \times 30'$ , and allow to sample a sizable fraction of stellar content of Carina.

We extensively used both instruments to collect multiwavelength data

telescope	camera	f.o.v. arcmin <sup>2</sup>	pixel scale ("/px) "/px
4m Blanco	WFI	32' × 33'	0.23
2.2m ESO	MosaicII	36' × 36'	0.27

Table 3.2: Summary of the main characteristic of the two instrument used to observe the Carina dSph galaxy.

of the Carina stars. Time series data of the central region were aimed at:

- studying the multiple events of the star formation history;
- studying the radial distribution of different populations in order to find any peculiarity;
- searching for variable stars, from the Tip of the RGB down to the MSTO;
- distance estimate based on different indicators (RR Lyrae mean magnitude, RGB Tip, ZAHB);
- metallicity estimates, based on the comparison with homogeneous set of theoretical tracks;
- age estimates of stellar populations;

Moreover, we recently acquired low resolution spectra for a sample of  $\approx 330$  stars. We present preliminary results on the radial velocity determinations, while chemical compositions will be estimated in the near future.

Our analysis has been extended to the outer regions of this galaxy. The main aim was to estimate the real extent of Carina, trying to find any trace of tidal interaction with the Galactic gravitational potential. We selected several different fields, and deep CMDs were obtained.

In the following, all the dataset collected will be presented and discussed, starting from the central regions and then moving to the outskirts.

### 3.2.1 The Central Region: data and reduction strategy

We present here the two main datasets, based on proprietary data collected with the WFI@2.2m ESO and the MOSAICII@4m CTIO telescope. The details of the observations are presented in tab. 3.3. It is worth noting that the observations were optimized for the RR Lyrae detection. This means that the exposure times were chosen as a compromise between high S/N ( $\approx 100$ ) at the magnitude level of the HB ( $V \approx 20.5$ ), and an adequate time sampling.

telescope	RA (h)	DEC (deg)	filter	exp. time (sec)	# of images	date
2.2m	06:41:50	-50:58:28	B	30,500	60	5-7 Jan 2000
2.2m	06:41:50	-50:58:28	V	30,300	63	5-7 Jan 2000
Blanco	06:41:38	-50:58:00	B	7,100	29	8-9 Jan 2000 *
Blanco	06:41:38	-50:58:00	V	11,200	29	8-9 Jan 2000 *
Blanco	06:41:38	-51:06:30	B	5,600	23	8-9 Jan 2000
Blanco	06:41:38	-51:06:30	V	9,000	23	8-9 Jan 2000

Table 3.3: Log of the observations collected for the central regions of the Carina dSph galaxy.

\* a few exposure were collected during the night of December 29, 1999

More than 50  $B,V$  couples were secured in both datasets. Data were collected between December, 29<sup>th</sup> 1999, and January 9<sup>th</sup>, 2000, with average good seeing conditions ( $\leq 1''$ ). Standard IRAF procedures for mosaic data reduction (MSCRED, Valdes 1997) were adopted for bias subtraction and flat-field correction. Even if the two datasets are centred on Carina, the orientation of the WFI camera was  $90^\circ$  rotated with respect of the MOSAICII CCDs. We decided to split the two datasets, which have been independently reduced. Moreover, it is important to note that a strong dither has been applied to the CTIO dataset. In fact, after the first night, technical problems to chip #5 forced the observer to apply a dither of  $\approx 8'$  in the North-South direction. As a consequence, the area covered by central chips were observed twice when compared with the chips at the border, but a new distant "ninth chip" was observed.

Each mosaic has been split in the eight individual chips, and the photometric reduction was made using DAOPHOTII/ALLFRAME.

### 3.2.2 The Color-Magnitude Diagrams

The two cumulative CMDs from the two data sets are shown in fig. 3.6 All the single catalogue have been rescaled on a common geometrical coordinate system using DAOMATCH/DAOMASTER. Each measurement has been calibrated according to the curves presented in section 2.4.1, and then a weighted mean was calculated. The two CMDs appear very deep, both reaching  $V \approx 25$ . However, the CTIO data set results in a much better color-magnitude diagram, where all the features appear much more defined than in the 2.2m CMD, even for the bright RGB and HB stars. The reasons for this are not related to the exposure times, or any other details of the observational strategy. The already mentioned problems of the positional effect and of the shape of the  $B$  filter are the main culprits of this intrinsically less accurate photometry. Even if both error sources have been taken into account and properly (within the errors) removed, the net effect is to blur

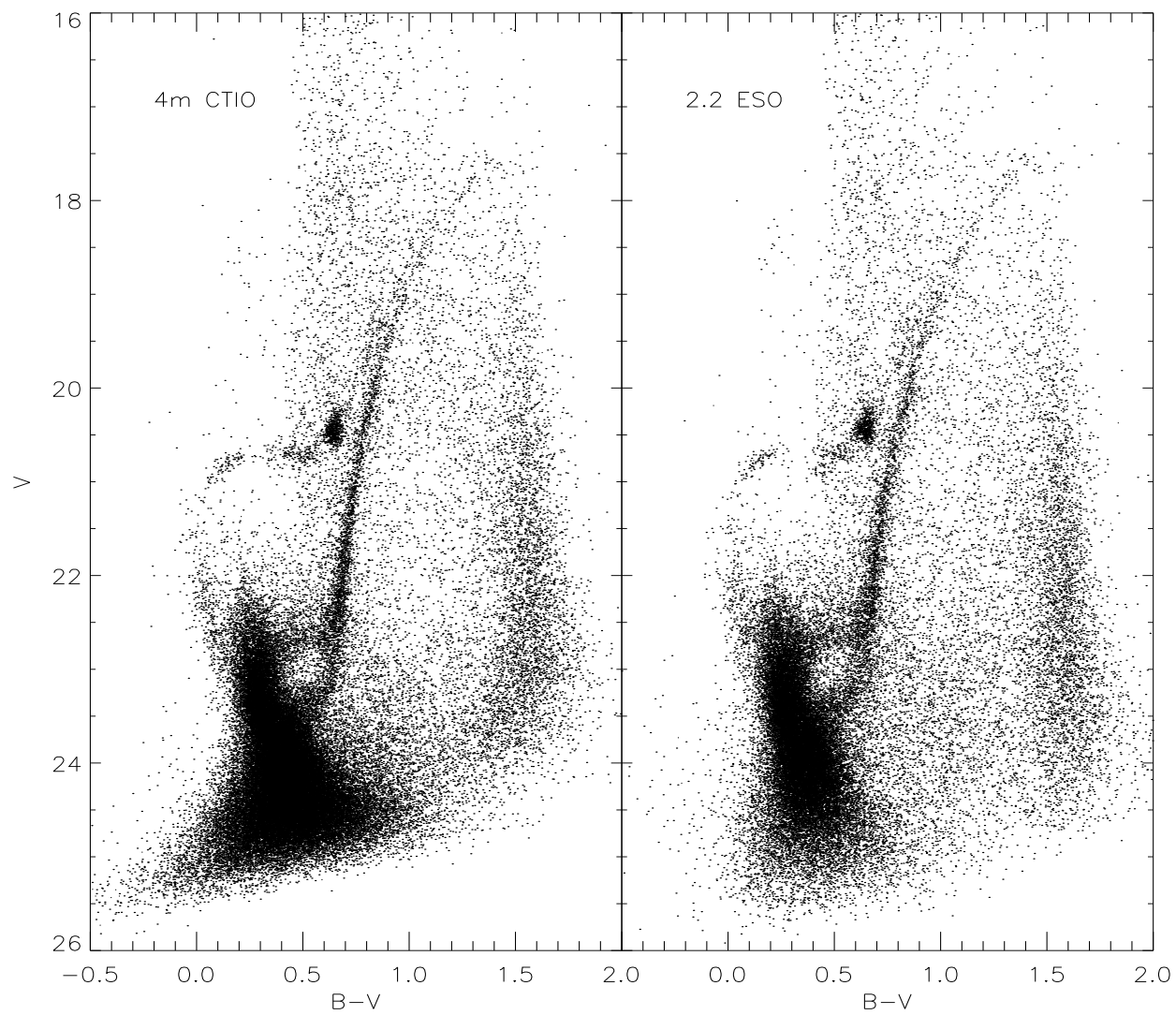


Figure 3.6: Comparison between the Carina CMD from the 4m CTIO and the 2.2m ESO datasets. The number of stars plotted is  $\approx 70,000$  (left) and  $\approx 50,000$ .

and broaden the features of the CMD. Any effort to average all the measurements from the two data sets resulted in a CMD which is worse than the CTIO data set only. This former CMD will be now extensively analysed, while the union of the two dataset will be useful for the detection of variable stars

To figure out the Carina evolutionary properties according to the observed CM diagram, one has first to single out detailed information on its metal content. This has been done by comparing the distribution in the CMD of the oldest Carina population with similar diagrams of old stellar systems with known metal abundance. This approach relies on the well-known evidence that the slope of the RGB is a bona fide metallicity indicator (Hartwick 1968). We found that the Carina old stellar population nicely follows the stellar distribution of the GGC NGC 1904 (Piotto et al. 2002), for which a mean metallicity of  $[Fe/H] \approx -1.69$  ( $Z=0.0004$ ) has been estimated (Zinn & West 1984). This empirical evidence strongly suggests not only a similar metallicity, but also a similar age, thus constraining the age of Carina old population in the range of ages typical of GGCs, i.e. 10-13 Gyr (VandenBerg et al. 2002). We notice that this metallicity estimate appears in good agreement with recent low-resolution spectra of the near infrared Ca II triplet in 52 stars located close to the tip of the Carina RGB. These data support a mean metallicity of  $[Fe/H] = -1.99 \pm 0.08$  (Smecker-Hane et al. 1999). However, these measurements present an intrinsic spread in metallicity of  $\approx 0.25$  dex ( $1\sigma$ ) and a full width of approximately 1 dex. This suggests that Carina could undergo a complex chemical evolution and/or SF history during the last few Gyrs. Recent findings in dSphs of the LG brought forward systematic differences not only between photometric indices and spectroscopic observations (Bonifacio et al. 2000; Cole, Smecker-Hane, & Gallagher 2000) but also between metallicities based on Ca II triplet and on Fe-peak element abundances (Tolstoy et al. 2003). Note that the latter is a thorny problem in stellar systems such as dwarf galaxies, because Ca is an  $\alpha$ -element.

An even more compelling comparison can be performed with the old LMC cluster Reticulum (Monelli et al. 2003), for which spectroscopic measurements support a metal abundance of  $[Fe/H] = -1.71 \pm 0.09$  (Suntzeff et al. 1992). This cluster indeed presents several advantages when compared with NGC 1904, the absolute calibration is more accurate, the relevant evolutionary phases are very well-defined across the CMD, and in particular the HB luminosity level. The comparison of HBs is facilitated because the Reticulum HB completely covers the instability strip (Walker 1992, 32 RR Lyrae), whereas NGC 1904 only contains blue HB stars and a few RR Lyrae (4 bona fide and 4 candidates, see Ferraro et al. 1992, and references therein). Fig. 3.7 shows that by simply decreasing the apparent magnitude of Reticulum stars by  $\Delta V \approx 1.68$  mag, the old Carina population nicely overlaps the Reticulum stellar loci all over H and He burning phase. One can derive the

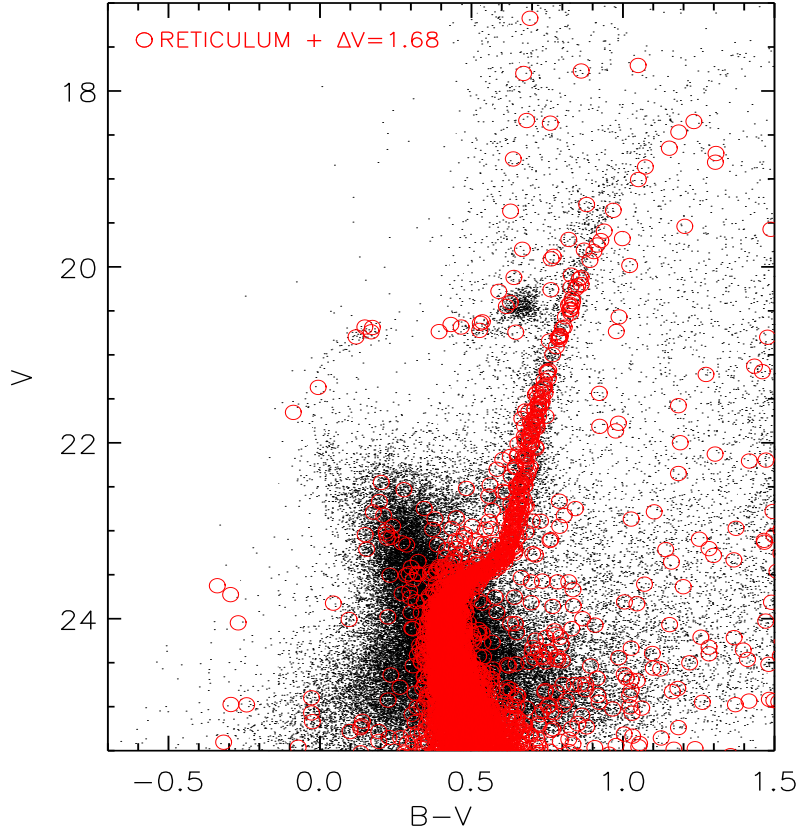


Figure 3.7: CMD of Carina, with, superimposed the stars belonging to the old LMC cluster Reticulum (red open circles, Monelli et al. 2003). The latter sample was artificially shifted in magnitude by  $\approx 1.68$  mag to match the old Carina population

conclusion that not only the two populations have quite similar evolutionary properties, but also that the two stellar systems should have quite similar reddenings. According to the pulsation properties of RR Lyrae stars, Walker (1992) estimated a mean reddening for Reticulum of  $E(B-V) = 0.03 \pm 0.02$ . The reddening map provided by Burstein & Heiles (1982) supplies for Carina a mean reddening of  $E(B-V) \approx 0.025$ , while the dust infrared map by Schlegel et al. (1998), provides, across the central  $0.3 \text{ degree}^2$  covered by our data, a mean reddening value of  $E(B-V) = 0.058 \pm 0.013$ . According to this map the reddening along the Northern direction is constant, whereas when moving from East to West presents a mild increase. In the following we assume  $E(B-V)=0.03$ , with an uncertainty which should not be larger than  $\pm 0.01 - 0.02$  mag.

Once we fixed both reddening value and metal content, we can compare empirical data with suitable theoretical isochrones. The comparison

was performed using stellar isochrones from the Pisa Evolutionary Library (Cariulo et al. 2004). The mixing length value adopted in these evolutionary models was calibrated as a function of metal content on the observed RGBs of GGCs. Theoretical predictions were transformed into the observational plane by adopting the bolometric corrections and the color-temperature relations predicted by atmosphere models (Castelli et al. 1997,a,b). To validate physical assumptions adopted to construct current stellar isochrones, fig. 3.8 shows the fit of the 11 Gyr isochrone (solid line) and of the Zero-Age-Horizontal-Branch (ZAHB, dashed line) to empirical data for the two quoted globular clusters. Theoretical predictions for NGC 1904 were plotted by adopting an apparent distance modulus of  $DM_V = (m - M)_V = 15.72$  mag and a reddening of  $E(B-V) = 0.03$  (Kravtsov et al. 1997). The distance was estimated using the apparent magnitude of HB stars estimated by Kravtsov et al. (1997),  $V_{HB} = 16.25$ , and the calibration of the  $M_V$  vs  $[Fe/H]$  relation provided by Caputo et al. (2000). The distance modulus we adopted for Reticulum is based on the classical Cepheid distance scale (Bono et al. 2002). Data plotted in this figure show that theory accounts quite well for both H and He burning evolutionary phases.

Now we adopt the same theoretical framework to constrain evolutionary properties of Carina stellar populations. Fig. 3.9 shows that theoretical predictions, by assuming a reddening of  $E(B-V) = 0.03$ , a mean metallicity of  $Z = 0.0004$ , and a distance  $DM_V = 20.24$  nicely fit the observed distributions for selected assumptions about stellar ages (see labeled values). The adopted distance appears in reasonable agreement with previous evaluations by Mighell (1997), Mateo, Hurley-Keller, & Nemeč (1998), Girardi & Salaris (2001), and by Dall’Ora et al. (2003). As a whole, we found evidence for a substantial amount of old stars with ages ranging around  $11 \pm 1$  Gyr. This finding, as well as the sizable sample of RR Lyrae stars (75) we have detected, confirms the early results by Smecker-Hane et al. (1994) and by Saha et al. (1986).

At the same time, data plotted in fig. 3.9 show that the bulk of the intermediate-mass stars present TO ages in the range of  $5 \pm 2$  Gyr. Age estimates for Red Clump (RC) stars provided by Caputo, Castellani & Degl’Innocenti (1995) on the basis of the difference in luminosity with the SGB give quite similar ages. This means that we can safely conclude that RC stars in Carina are the bona fide counterpart of the above intermediate-age population.

Moreover and even more importantly, data plotted in 3.9 bring forward the occurrence of young MS stars with ages younger than 1 Gyr (see the 0.6 Gyr isochrone plotted in the figure). The occurrence of relatively young stars is interesting because the available literature suggested that the most recent SF episode in Carina took place approximately 2-3 Gyr ago (Dolphin 2002). In this context it is worth mentioning that a stellar population as young as this might account for the sizable sample of Anomalous Cepheids

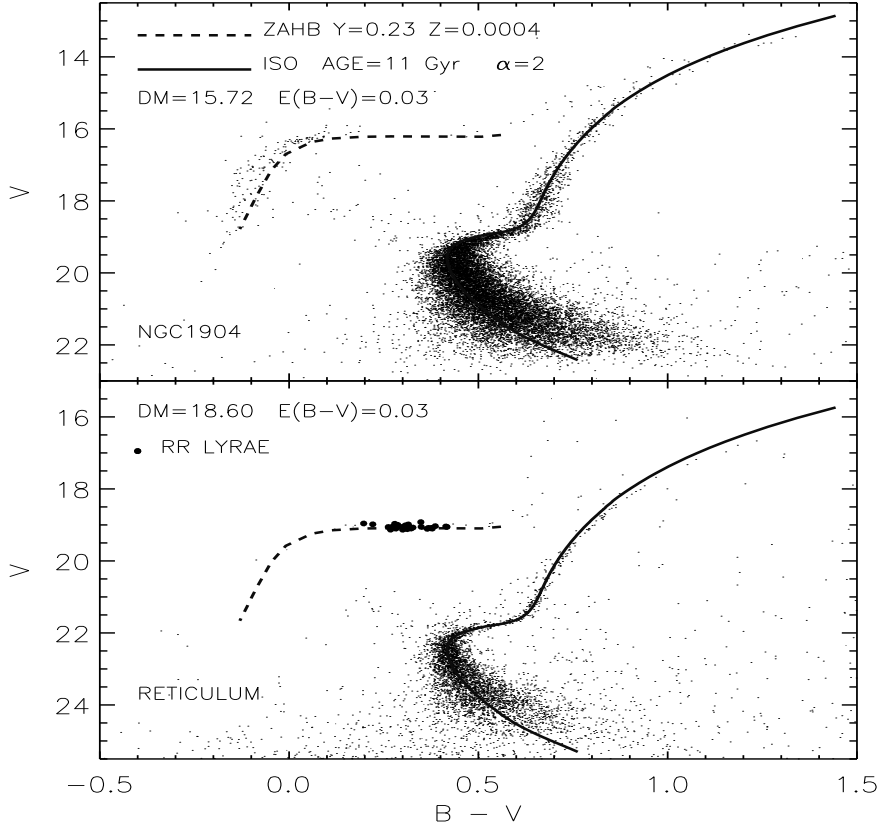


Figure 3.8: Top - Comparison between theoretical predictions and empirical data for the GGC NGC 1904. The solid line shows an isochrone of 11 Gyr, constructed by adopting  $Y=0.23$ ,  $Z=0.004$ , and a mixing length  $\alpha = 2$ . The dashed line displays the ZAHB for the same chemical composition (see text for details). The photometry was performed by Piotto et al. (2002) (see also the web page <http://www.menhir.pd.astro.it>). Bottom - Same as the top, but the data refer to Reticulum (Monelli et al. 2003). Theoretical models were plotted using distance moduli and reddening estimates available in the literature. See text for more details.

(6 bona fide plus 9 candidates) detected by Dall’Ora et al. (2003). If we assume that these bright variables are the progeny of young single stars then young, intermediate-mass He burning structures should account for their distribution in the CMD. To further constrain the nature of these objects we decided to investigate whether they could be Blue Stragglers of the old stellar population. Following Fusi Pecci et al. (1992) and Mateo, Fischer, & Krzemiński (1995) we estimated the specific frequency of blue plume stars and we found that  $N_B/N_{HB} = 360/280 \approx 1.3$ . Empirical estimates suggest that GGCs characterized by very low central densities present a specific frequency of BSs that is at least a factor of 2.5 smaller, namely  $N_{BS}/N_{HB} \approx 0.5$  (Preston & Sneden 2000). This finding further strengthens the hypothesis that blue plume stars are genuine young stars.

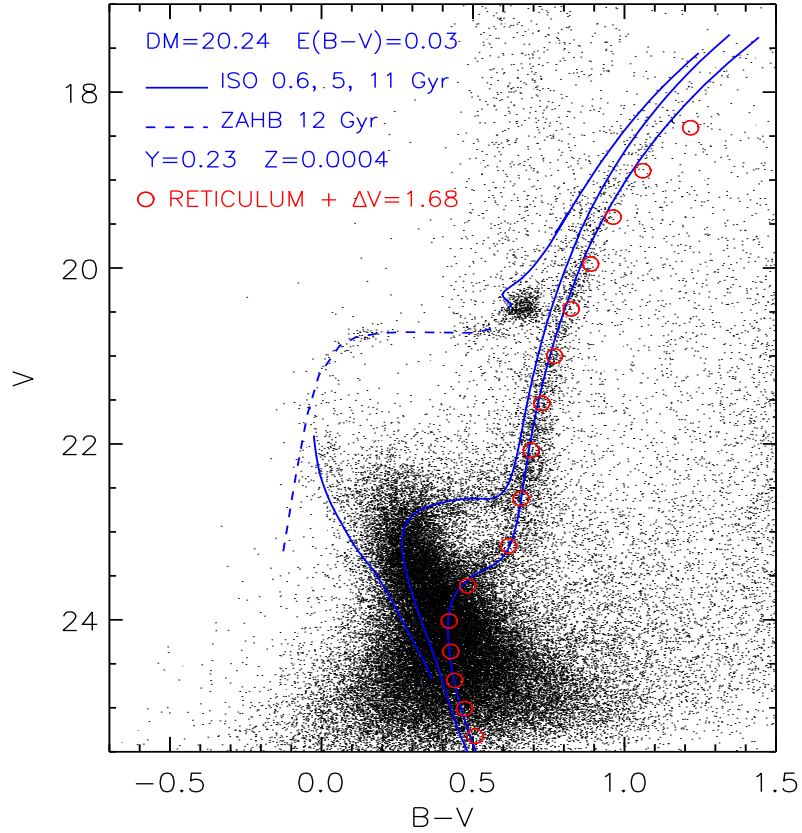


Figure 3.9: The cumulative CMD of Carina together with theoretical isochrones (solid blue lines) at fixed chemical composition  $-Y=0.23, Z=0.0004-$  and mixing length  $\alpha = 2$ . The isochrones range from 0.6 to 11 Gyr (see labeled values). Dashed line shows the ZAHB for the same chemical composition and for a progenitor age of 12 Gyr. Note that the isochrone for  $t \approx 5$  Gyr nicely fits the red clump region. Red open circles display the Reticulum ridge line. See text for details concerning distance and reddening correction.

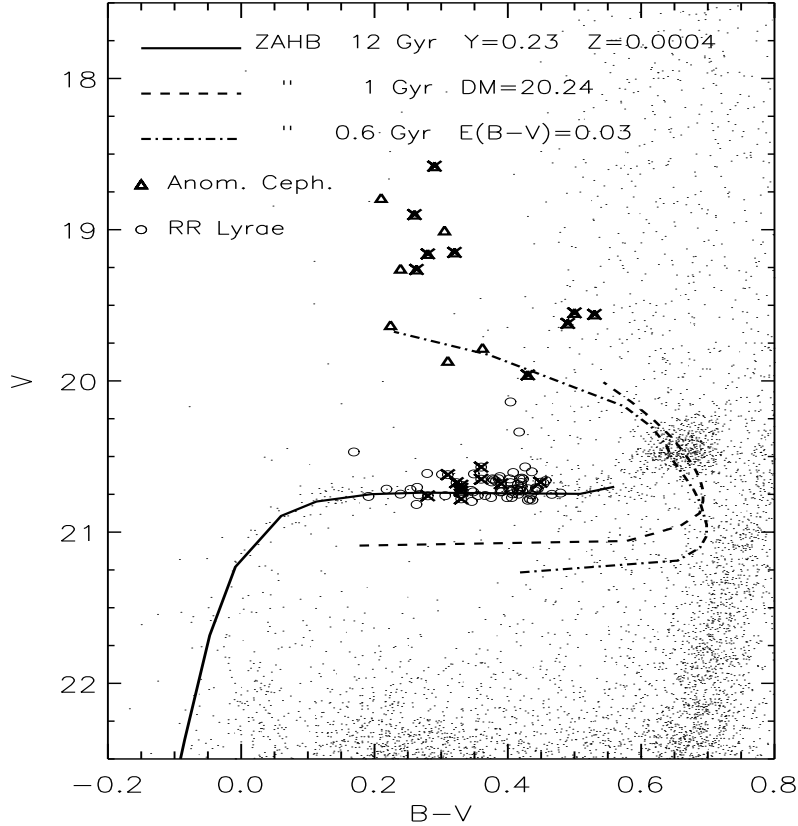


Figure 3.10: Comparison between predicted and empirical He-burning stars. Together with static stars (small dots) are also plotted the Carina variables: circles RR Lyrae stars, triangles, ACs. Crosses mark variables that present poor-phase coverage. Different line styles display predicted Zero Age He-burning structures at fixed chemical composition and progenitor ages ranging from 12 ( $M = 0.8M_{\odot}$ ) to 0.6 ( $M = 2.2M_{\odot}$ ) Gyr.

Figure 3.10 shows the comparison between old, low-mass RR Lyrae stars (circles) and young, intermediate-mass ACs (triangles) with theoretical predictions for Zero Age He-burning structures at fixed chemical composition and different assumptions for the progenitor age (Cassisi et al. 2003). Data in this figure support the evidence that the position of bright and bluer ACs appear in reasonable agreement with stars originating from the Zero Age He-burning structures constructed assuming the same chemical composition of the old stellar component ( $Y=0.23$ ,  $Z=0.0004$ ), a progenitor age of 0.6 Gyr, and therefore with a stellar mass  $M \approx 2.2M_{\odot}$ . This finding is in good agreement with the lower limit in stellar mass provided in Dall’Ora et al. (2003) on the basis of their pulsation properties, i.e.  $M \geq 1.4 - 1.5M_{\odot}$ . However, we cannot exclude that some redder ACs are the result of mass transfer in old binary systems (Renzini, Mengel, & Sweigart 1977; Corwin, Carney, & Nifong 1999).

To constrain the Carina mean metallicity we performed the same comparison between theory and observations of Figures 3.9 and 3.10 but using isochrones and He burning models for  $Z=0.0006$  ( $[\text{Fe}/\text{H}]\approx -1.5$ ) and  $Z=0.0002$  ( $[\text{Fe}/\text{H}]\approx -2.0$ ). Interestingly enough, we found that the new predictions for plausible assumptions concerning the distance and the reddening do not account for the three observables that are more sensitive to metal abundance, namely RGB color, HB luminosity, and RC color. In particular, more metal-rich predictions account for RGB color, and HB luminosity but Zero Age He-burning models are systematically bluer than RC stars. On the other hand, the more metal-poor predictions somehow account for HB luminosity and RC color, but the isochrones for the same ages are systematically redder than RGB stars.

Before concluding this section, let us notice that an age of the order of 11 Gyr makes the Carina old population coeval not only with NGC 1904 and Reticulum, but also with several other well studied globulars in the Galaxy (Cassisi et al. 1999) as well as in the Magellanic Clouds (Brocato et al. 1996). As long as the evidence that these stellar systems are coeval is not affected at all by the adopted theoretical evolutionary scenario, the evaluation of the absolute age does depend on it. By adopting the same theoretical framework but neglecting the efficiency of element diffusion we would derive cluster ages older by approximately 1 Gyr.

### 3.2.3 Radial distributions

On the basis of preliminary empirical evidence (Mighell 1997; Harbeck et al. 2001) it has been suggested that the old and the intermediate-age populations in Carina present different radial distributions. To investigate the spatial distribution of different stellar populations, we selected stars in suitable boxes representative of the old (see dashed boxes in fig. 3.11) and of the intermediate-age population (solid boxes). This approach, when compared with similar analyses in the literature, presents the substantial advantage to use quite large stellar samples both for the old ( $\approx 1000$ ) and the young ( $\approx 5000$ ) population.

Left panel of fig. 3.12 shows the comparison between the isodensities of the whole stellar sample (dashed contours) in Carina with those for the old (HB, SGB) stellar population (solid contours). The isodensity contours range from  $\approx 20\%$ , to  $100\%$  of the central maximum density with a density step of  $20\%$  the right panel of fig. 3.12 shows the same data, but the solid contours refer to the young (RC, intermediate-age MS) stellar population.

Data plotted in this figure show that the isodensity contours of the intermediate-age population resembles quite well the density distribution of the whole data. On the contrary, the isodensity contours of the old population appear more irregular, with a small offset of about 2 arcmin in the peak density of the old population when compared with the Carina center (see

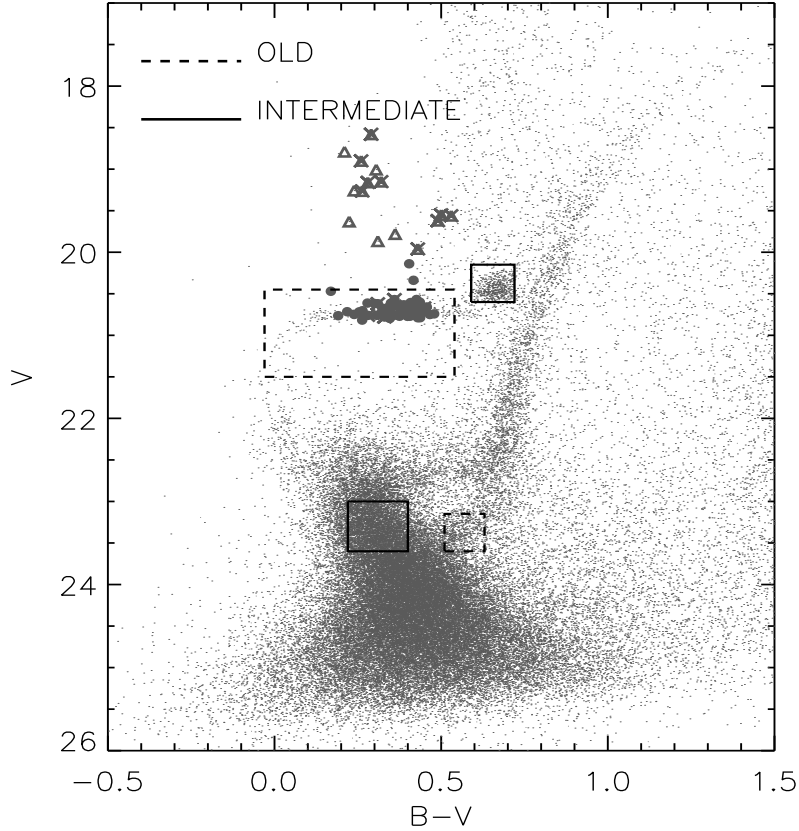


Figure 3.11: The dashed and the solid boxes show the CMD regions selected as representative of the old (HB and SGB) and of the young (RC, intermediate-age MS) population respectively. Variables have been plotted using the same symbols as in fig. 3.10.

the cross in fig. 3.12). To estimate on a quantitative basis the difference between the two populations we performed several two-tails Kolmogorov-Smirnov (KS) tests. At first, we tested whether the two old subsamples, i.e. the HB and SGB, present the same radial distributions. We found that the two distributions are almost identical, since the KS probability is equal to 90%. The same outcome applies to the two young subsamples, namely RC and intermediate-age MS, and indeed the KS probability is equal to 94%. On the other hand, the KS test applied to the old and the young samples, supplies a vanishing probability that the two radial distributions are the same. To avoid deceptive errors introduced by the spatial smoothing of the isocontour levels we decided to investigate the *in situ* spatial distributions of the two populations along the major and the minor axis, assuming a position angle of approximately 60 degrees ( $pa = 65 \pm 5^\circ$ , Irwin & Hatzidimitriou 1995). Moving along the major axis and by assuming a bin size of 2 arcmin

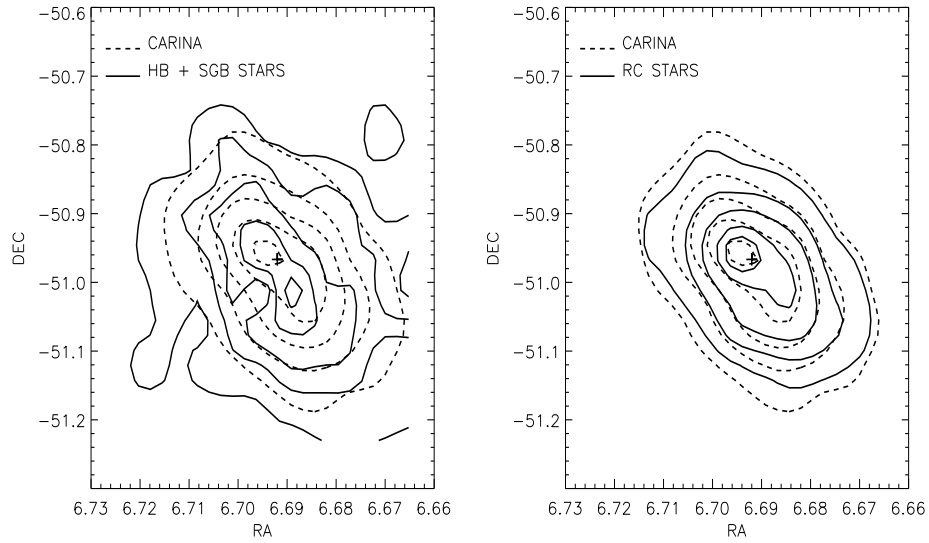


Figure 3.12: The isodensity map of the Carina stellar content (dashed contours). The solid contours in the left panel show the isodensity levels of the old (HB and SGB) stellar population. The isodensity levels range from 20% to 100% with a step of 20%. The right panel shows the comparison with the isodensity levels of the young (RC and intermediate-age MS) stellar population.

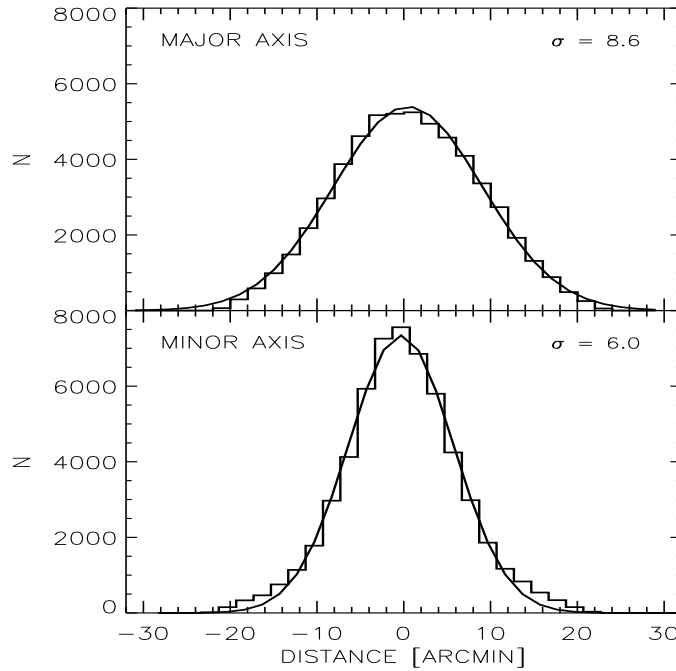


Figure 3.13: Histograms of the star counts along the major (top) and the minor (bottom) axis for the entire stellar population of the Carina dSph. The sigma of the gaussian fits are labeled.

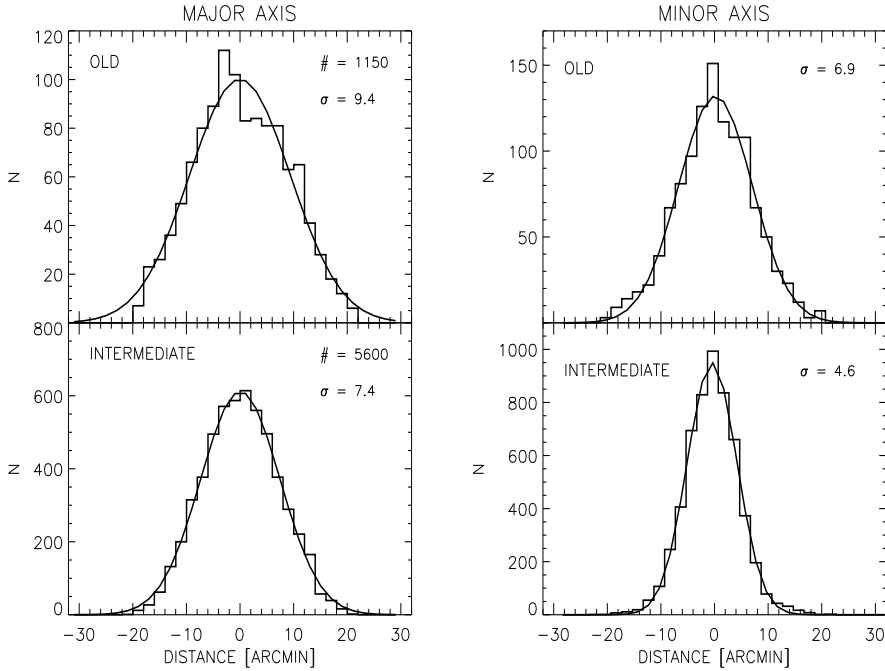


Figure 3.14: Left panel: histograms of the star counts for the old (top) and the intermediate-age (bottom) stellar populations along the Carina major axis. Right panel: same as left, but projected along the minor axis. In both cases the old population shows a broader distribution.

we computed the histogram of the entire stellar content of the galaxy. The same procedure was repeated but along the minor axis. fig. 3.13 shows the spatial distribution along the major (top) and the minor (bottom) axis respectively. Interestingly enough, we found that the eccentricity ( $e = 1 - b/a$ ), where  $b$  and  $a$  are the FWHMs of the individual distributions given by the gaussian fits, is roughly equal to  $\approx 0.3$ . This estimate is in good agreement with the estimate provided by Irwin & Hatzidimitriou (1995).

The same procedure has been applied to the old and the young samples. Figure 3.14 shows the two spatial distributions along the major axis and the minor axis respectively.

In both cases the spatial distribution of the old component is broader than the distribution of the young component. It turns out that the eccentricity of the old component is  $\approx 0.27$ , and therefore quite similar to the eccentricity of the entire galaxy. On the other hand, the eccentricity of the young population is  $\approx 0.38$ . We performed several tests by changing the bin size from 1.5 to 3 arcmin and we found that the eccentricities of the young and old populations change by less than a few percent. Therefore, current estimates seem to suggest that the old stellar component is distributed over a sort of "spheroidal halo", while the young component is more concentrated and flattened along the major axis. Moreover, data plotted in fig. 3.14 also show an interesting feature: the spatial distribution along the major axis of

the old population peaks at  $\approx 2 \pm 1$  arcmin from the Carina center, while it is centrally peaked along the minor axis. On the contrary, the young population is centrally peaked both along the major and the minor axis. This evidence further supports the hypothesis of a difference in the spatial distribution between the old and the young stellar populations.

We mention that data plotted in fig. 3.13, also suggest that the spatial distribution of the old component along the two axes is not centrally symmetric. The slope of the star counts in the South-West direction is steeper than along the opposite direction. This empirical evidence seem to suggest that the young and more massive population is more centrally concentrated than the old one. The present result, once confirmed, might provide valuable constraints on the Carina dynamical history and on its interaction with the Galaxy (Kuhn et al. 1996; Majewski et al. 2000a).

In their photometric investigation Stetson, Hesser & Smacker-Hane (1998) found that different stellar components in the Fornax dSph might present different centroids. Therefore, we performed a new test to figure out whether the young stellar component in Carina exhibits the same radial distribution as the intermediate one. The KS test suggests that blue plume stars present a radial distribution quite similar to RC and intermediate-age MS stars, and indeed the KS probability is roughly equal to  $\approx 50\%$ . On the other hand, the KS test with old HB stars indicates that the two populations are different, since the KS probability is vanishing ( $P=0.00001$ ).

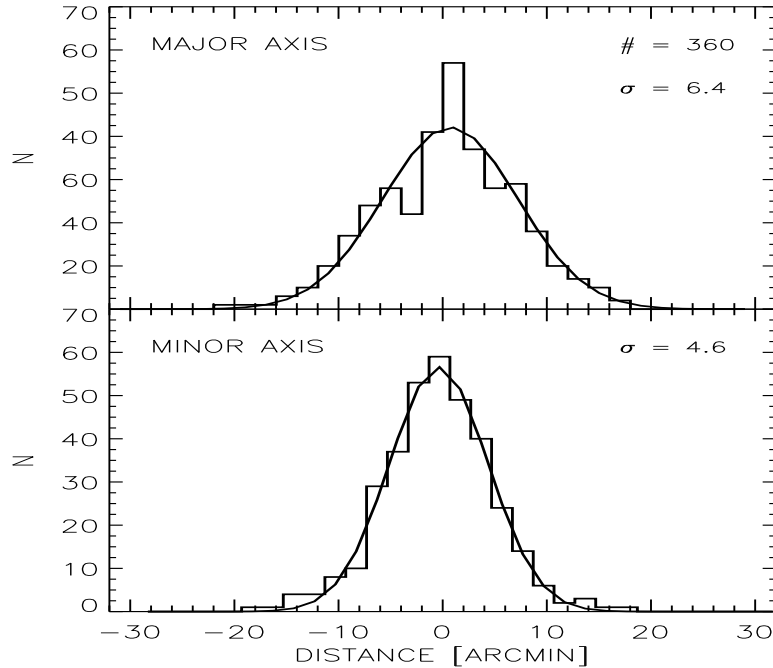


Figure 3.15: Same as fig. 3.13, but for blue plume stars along the major (top) and the minor (bottom) axis.

Finally, we also investigated the radial distribution of blue plume stars along the major and the minor axis. The comparison between data plotted in fig. 3.15 and data plotted in the bottom panel of 3.14 indicates that the radial distributions of these two stellar components are quite similar along the minor axis. Nevertheless there is a mild evidence that blue plume stars along the major axis appear more centrally concentrated. Unfortunately, current data do not allow us to constrain on a quantitative basis the difference in the centroids.

### 3.2.4 Field Subtraction

The color-magnitude diagram of the central region discloses the presence of heavy contamination by foreground Galactic stars. Carina is located at low galactic latitude ( $\approx -22^\circ$ ), therefore we expect to observe a non-negligible portion of the Galactic disk along the line of sight. The morphology of the field shows two main peaks, at  $B-V \approx 0.5$  and  $B-V \approx 1.8$ . We used our external fields (see section 3.2.5) to subtract the Galactic stellar component. The statistical subtraction we adopted is based on the comparison between the CMD of the cluster and the CMD of a nearby region. In its simplest application, this method subdivides the two CMD into a grid of magnitudes and color bins, counts the number of objects in each bin of the template field and randomly subtracts the same amount of stars from the corresponding bin of the cluster CMD. The Poisson error of the counting process is the main error source, and the method assumes that the Galactic field doesn't change between the two observed region of the sky. In our analysis, we selected two regions in the outskirts of Carina, observed with the 4m CTIO telescope. The two fields are located approximately at  $2^\circ$  from the Carina centre, along the major and minor axis. The details of the reduction and analysis of these fields is presented in section 3.2.5. It is worth noting that the two CMDs diagrams are very similar, and there is not evident presence of bright evolved Carina stars, as clearly shown in fig. 3.16. The global list of stars was assumed as reference list for the subtraction. To compensate the much greater area, we normalized the star counts in the region  $1.25 < B - V < 2$ ,  $18 < V < 22$ . The input parameters to be chosen *a priori* are the color and magnitude range in which the subtraction will be performed and the bin size. Once these parameters are fixed, the grid is automatically set. We tried to develop an algorithm that was not based on a random extraction of stars connected with the number of the field stars in each bin. We tried to exploit the information on the color and magnitude distribution of stars in the field, trying to reject the stars that more likely follow the same distribution in the Carina CMD. To do this, in each bin we estimate the normalized cumulative Probability Distribution Function (PDF) of both color and magnitude distribution, which are then interpolated with a spline function. Two random numbers are generated in the range  $0 < x < 1$ . These

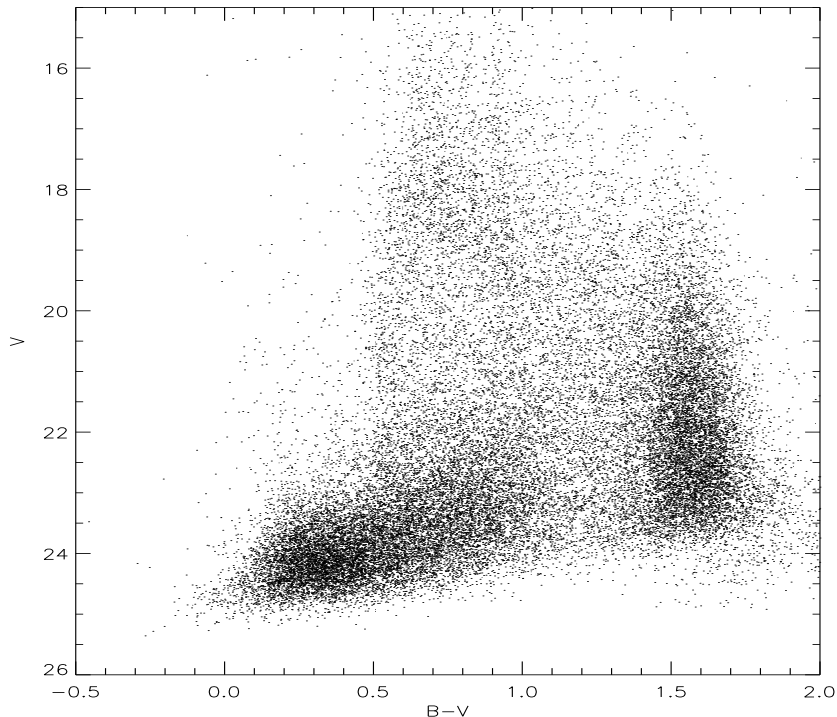


Figure 3.16: CMD of the two field used for the statistical subtraction of foreground stars.

two points are used as representative of the two PDFs, and the corresponding values of color and magnitude are estimated from the spline. This algorithm ensures that the random choice of the points reflects the real distribution in the CMD. Once the random star has been generated, the code finds the real star in the Carina CMD which is closest to it, and remove it. To estimate how many stars should be rejected per bin, we did not simply count their number in each bin of the field CMD. To limit the effect of small numbers in the star counts, stars are counted in a  $3 \times 3$  grid, and the median of the sample is adopted as the number for the subtraction. However, our test revealed that the final results somehow depend on the input parameters, both the extreme color as well as the binsize adopted. To reduce the fluctuations, a smoothing technique was applied. The grid is shifted in color and magnitude of a fraction of bin, and for each position of the grid a subtraction is performed, and the rejected stars saved. Typically, a  $3 \times 3$  or  $5 \times 5$  dithering is used, with color and magnitude bin dimensions varying in the range  $[0.1, 0.5]$  mag. At the end of all the iterations, an histogram of all stars rejected per each bin of the original grid is calculated. The stars which have been most frequently selected are rejected. It is also possible to set a variable binsize, in both color and magnitude. Our best result was obtained with a  $3 \times 3$  dithering grid, and binsize variable in the range 0.1, 0.2, 0.3 mag. This means that

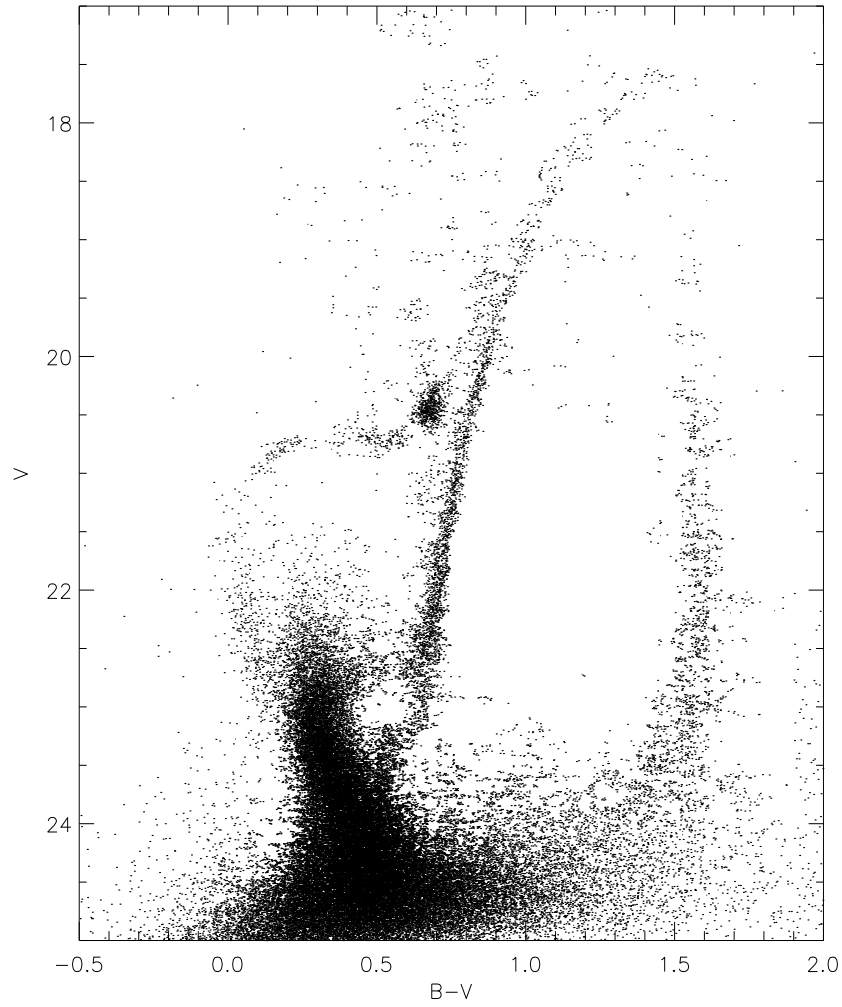


Figure 3.17: The CMD of central region of Carina after the subtraction of Galactic stars. The peak of residual field stars at  $B - V = 1.8$  is probably due to normalization effects. The two fields use for the subtraction are distant  $\approx 4^\circ$ , and it is reasonable at this Galactic latitude to expect variation of the field star distribution that can cause this effect.

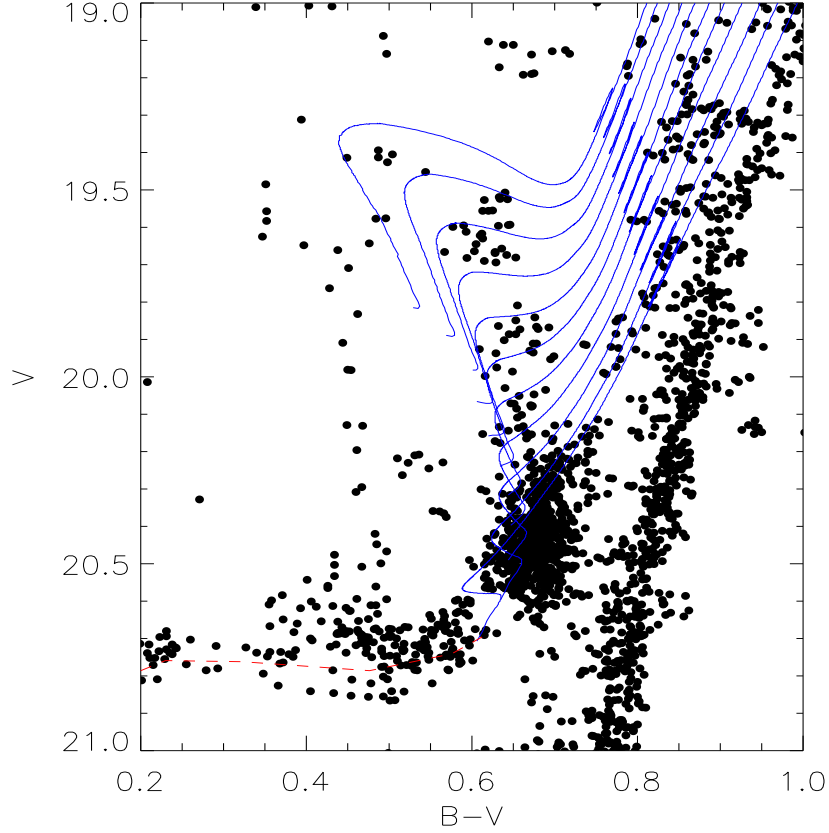


Figure 3.18: Zoom of the HB region. The blue lines are the post-ZAHB evolution of stars with mass ranging from  $0.9M_{\odot}$  and  $2M_{\odot}$ , for a chemical composition  $Z=0.004$ . The hook of bright stars at  $B - V \approx 0.6 \div 0.7$  and  $19.2 \leq V \leq 20.5$  predicted by theoretical models is in good agreement with the features present in our CMD after the subtraction of field stars. The red dashed line indicate the ZAHB for a 12Gyr population.

the code performed  $3 \times 3 \times 3 \times 3 = 81$  subtractions per bin before selecting the final set of star to be eliminated.

Fig. 3.17 shows the result. Many interesting features are evident.

- The TO region is now well defined, the two main subgiants are separated, and the TO of the old population is almost disentangled from the intermediate-age MS. Moreover, the intermediate-age sub-giant branch appears to be more structured. A small gap appears at  $V \approx 22.5$ , suggestive of an halt in the star formation history. This feature appears in all the simulations we made, and does not seem to be a spurious artifact due to the algorithm for the field subtraction.

- In the bright part of the diagram, the Red Clump morphology shows two interesting features. First, the hook of stars which are presumably

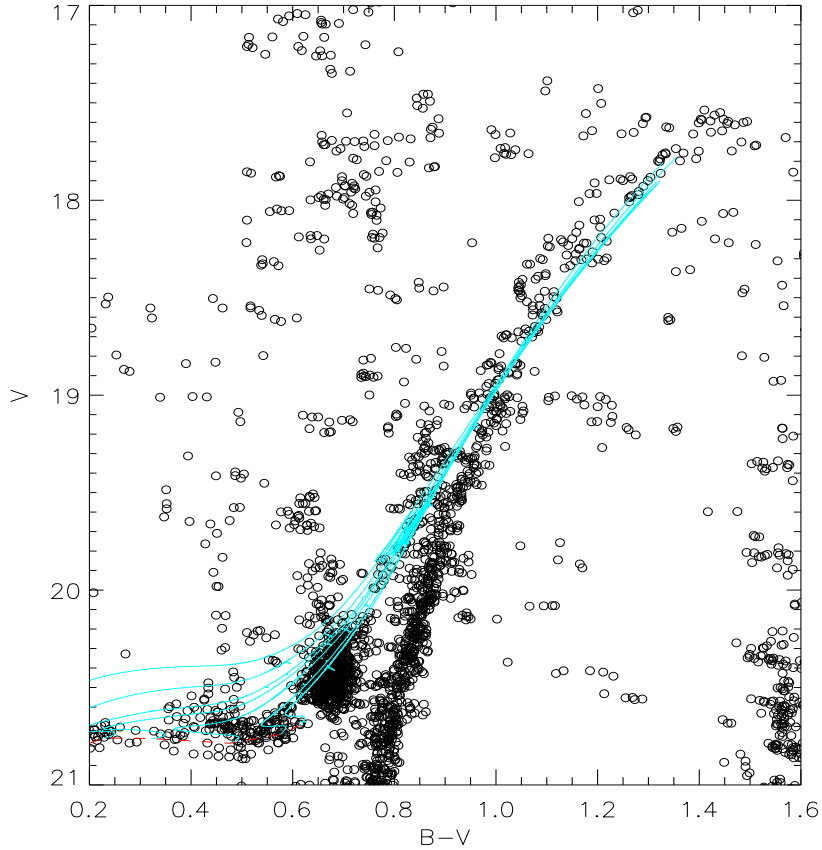


Figure 3.19: Post-ZAHB evolution of stars with mass  $M < 0.9 M_{\odot}$ ,  $Z = 0.004$ . The overdensity of points between  $B - V \approx 0.75$  and  $B - V \approx 0.90$  is consistent with the AGB of the old population.

populating the region of central helium burning stars in the mass interval  $1.3 < M < 2 M_{\odot}$ , see fig. 3.18. Second, the spread in color and magnitude is very small, suggestive of a small spread in metallicity. Moreover, the gap between the RC and the red HB of old stars is evident.

- The Asymptotic Giant Branch seems to be split in two regions. We interpret this as an evidence that we are observing the two AGBs of the old and intermediate-age stars. The comparison with theoretical tracks shows excellent agreement between the overdensity of stars in our CMD and position of the AGB bumps for the two populations (fig. 3.19).

### 3.2.5 Moving outward

We already mentioned the debate in the literature concerning the high  $M/L$  ratio of Carina and the possible explanation with a huge halo of DM. However, the possibility that Carina is interacting with the Galactic tidal field

has not been rejected nor demonstrated yet. If this was the case, such high values of the  $M/L$  ratio should be revised, because the current estimates rely on the hypothesis that the system is virialized, that is in dynamical equilibrium. It is important to note that the works by Hayashi et al. (2003) and Kazantzidis et al. (2004) predict that small systems like dSph galaxies should be strongly affected by the tidal interaction with the Galaxy, loosing most of their stellar content in a few orbits. Moreover, they claim that the tidal radius predicted by these models is much bigger than actually estimated, by a factor from 3 to 20.

We underwent a detailed study of the outer regions of Carina, in order to:

- estimate the real extent of the galaxy;
- search for evidence of tidal tails around Carina, if any;
- study the spatial distribution of different stellar populations at great distances from the centre, in order to verify the results obtained in the central regions. In particular, we were interested in testing to verify the occurrence of a "halo" of old stars surrounding Carina.

As a natural extent of the Carina project we selected five fields, mapping both the major and minor axis of the galaxy well beyond the tidal radius estimated by Irwin & Hatzidimitriou (1995). Two twin proposals were approved in 2002, and the observations were made between October 2002 and March 2003 at the 2.2m ESO and at the 4m Blanco CTIO telescopes. The details are presented in table 3.4, and the finding chart is shown in fig. 3.20. Note that at the time of writing all the fields have been reduced, with the exceptions of field *A* and *B* (yellow squares in fig. 3.20). The choice to observe with two telescopes relies on two different approaches to the same problem: how can we prove the existence of extra-tidal Carina stars in our fields? We used the 2.2m with the same philosophy of other previous works (Kuhn et al. 1996; Majewski et al. 2000a; Walcher et al. 2003): we decided to use RR Lyrae stars as stellar tracers, that is (relatively) bright, variable stars. We needed short integration times to detect the variability, and the 2.2m was the ideal instrument to accomplish this goal. However, we expected to find a very few objects, because of the low density of Carina and because we are observing stars in the phase of central Helium burning, i.e. life times of the order or  $10^8$ yr. Since we expect to find  $\approx 2000$  MS stars per each HB star, we decided to collect also, for selected fields, a few deep exposures with the 4m Blanco telescope. Our goal was to go deep enough ( $V \approx 25$ mag) to detect the TO of the Carina populations.

We refer to these fields with letters from *A* to *E* (tab. 3.4). Note that field *C* and *D*, are located across the tidal radius of Carina in both sides of the galaxy along the major axis. The reduction has been performed with

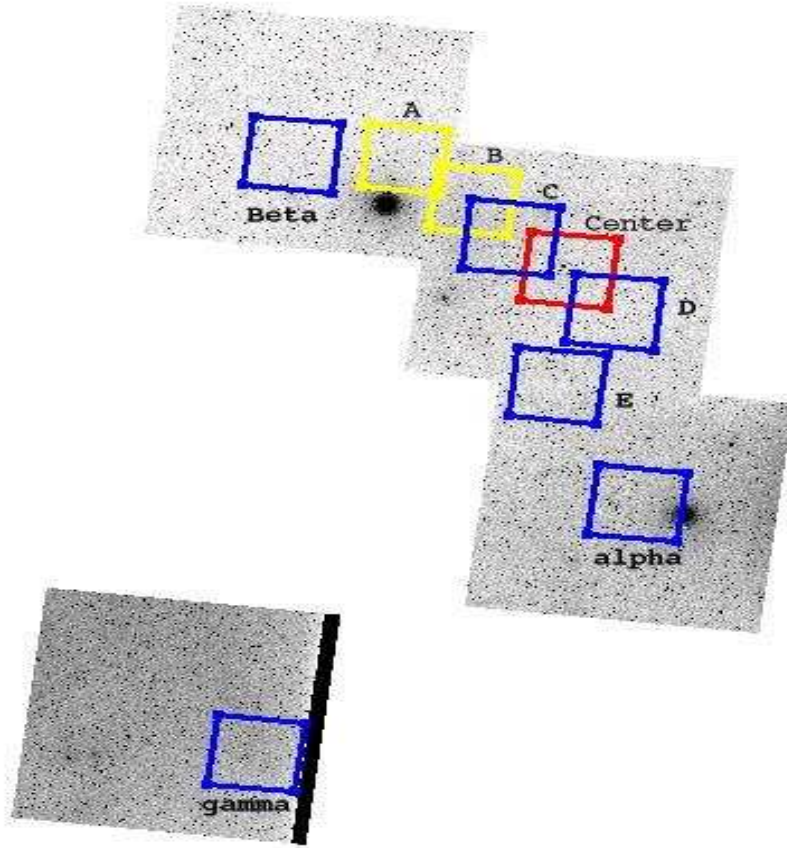


Figure 3.20: Positions of the fields observed. The red square shows the central regions, while the blue squares indicate the reduced fields.

DAOPHOTII/ALLFRAME, similarly to the central region. The calibration strategy has already been discussed in section 2.5.

Fig. 3.21 and 3.22 show the Color-Magnitude diagrams of fields *C* and *D*. Each panel shows the single CMD from one chip of the camera. Chip #3 was not available during the night of observations. The superimposition with the central regions is evident, but it is important to underline that the most distant chips are completely outside the tidal radius of Carina, at distances of at least  $30'$ .

The number of stars clearly decreases when moving from the centre to the outskirts, but there is a blue spur of faint objects ( $B - V \leq 0.4$ ,  $V \geq 23$ ) that is present in all the panels. These objects have the same colors and magnitudes of the old Main Sequence (MS) of Carina, and are located at distances from the centre of the order of  $\approx 40'$ , i.e. well beyond the Carina

field name	RA	DEC	total exposure time		D	telescope
	(h)	(deg)	B	V	( $l$ )	
A	06:48:30	-50:00:00	9600	7200	52	2.2m,Blanco
B	06:46:00	-50:25:00	9600	7200	87	2.2m
C	06:44:30	-50:44:00	9600	7200	30	Blanco
D	06:39:30	-51:18:00	8800	6000	28	Blanco
E	06:41:38	-51:58:00	5000	3000	60	Blanco
$\alpha$	06:53:45	-50:05:00	7200	4320	126	Blanco
$\beta$	06:37:30	-52:56:00	7200	7320	125	Blanco
$\gamma$	06:54:00	-55:15:00	3100	1920	282	Blanco

Table 3.4: RA, DEC, total exposure times and distance from the Carina center for the outer fields observed. Note that fields *A*, *B* have not been included in our analysis yet.

tidal radius (Irwin & Hatzidimitriou 1995). Note that the stars plotted in this CMD have been detected in all the images.

To further investigate the origin of this feature, we decided to observe again fields *C* and *D*, and indeed we selected new and more distant regions. Table 3.4 summarizes the characteristics of fields *E*,  $\alpha$ ,  $\beta$ ,  $\gamma$ , which are located at respectively  $1^\circ$  (south),  $2^\circ$  (east),  $2^\circ$  (west), and  $4.5^\circ$  (south-east) from the centre. The data were collected with the 4m Blanco telescope from October 2002 to January 2004.

Fig. 3.23 show the cumulative CMDs, with overplotted the same set of isochrones used for the central region.

The blue spur is present in all the figures. Moreover, the blue spur seems to be less populated at larger distances from the centre (field  $\gamma$ ). However, integration time for the external fields are quite different, and therefore a quantitative analysis of the completeness has not been performed yet.

Before we can assess the detection of such a strong component of extra-tidal stars, we have to analyze any possible source that can contaminate our sample. There are two main candidates: foreground Galactic field stars, and background distant galaxies.

To estimate the foreground stars contribution in this region of the sky, we computed a synthetic CMD (Degl’Innocenti 2004, private communication) of the Galactic component for all our fields. Fig. 3.24 shows an example comparing the real data with the simulation. All the features of the Galactic field are well represented by the model. The model is, by definition, deeper than the real data, which reach a limit magnitude of  $V \approx 25$ . Moreover, saturation problems make brighter part of the observed diagram less populated than the theoretical one. The features in the observed CMD appear broader because of the photometric error. However, the model predicts only

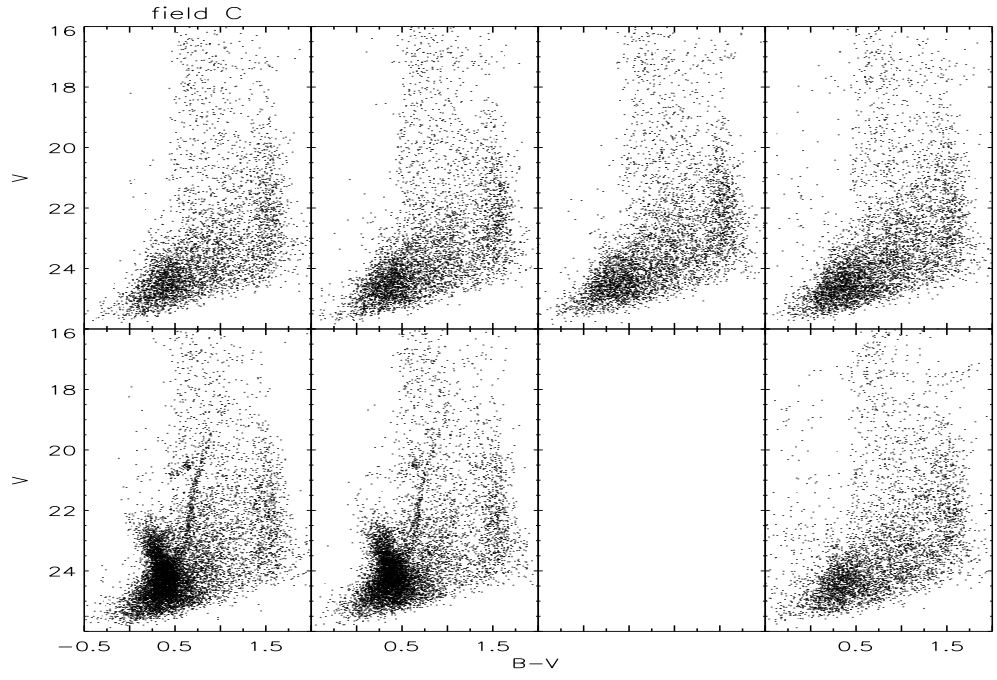


Figure 3.21: 8-panel CMD of field *C*. A spur of faint blue objects is evident in all the chips, and is present at distances of  $\approx 40'$  from the Carina centre.

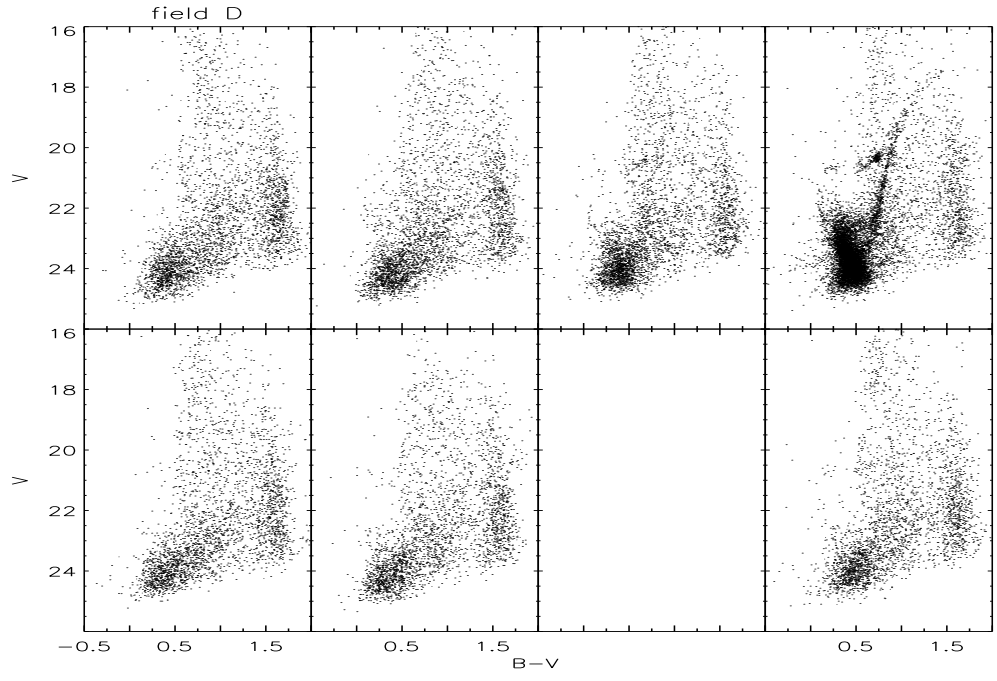


Figure 3.22: Same as 3.21, but for field *D*. The two fields are located along the major axis of Carina.

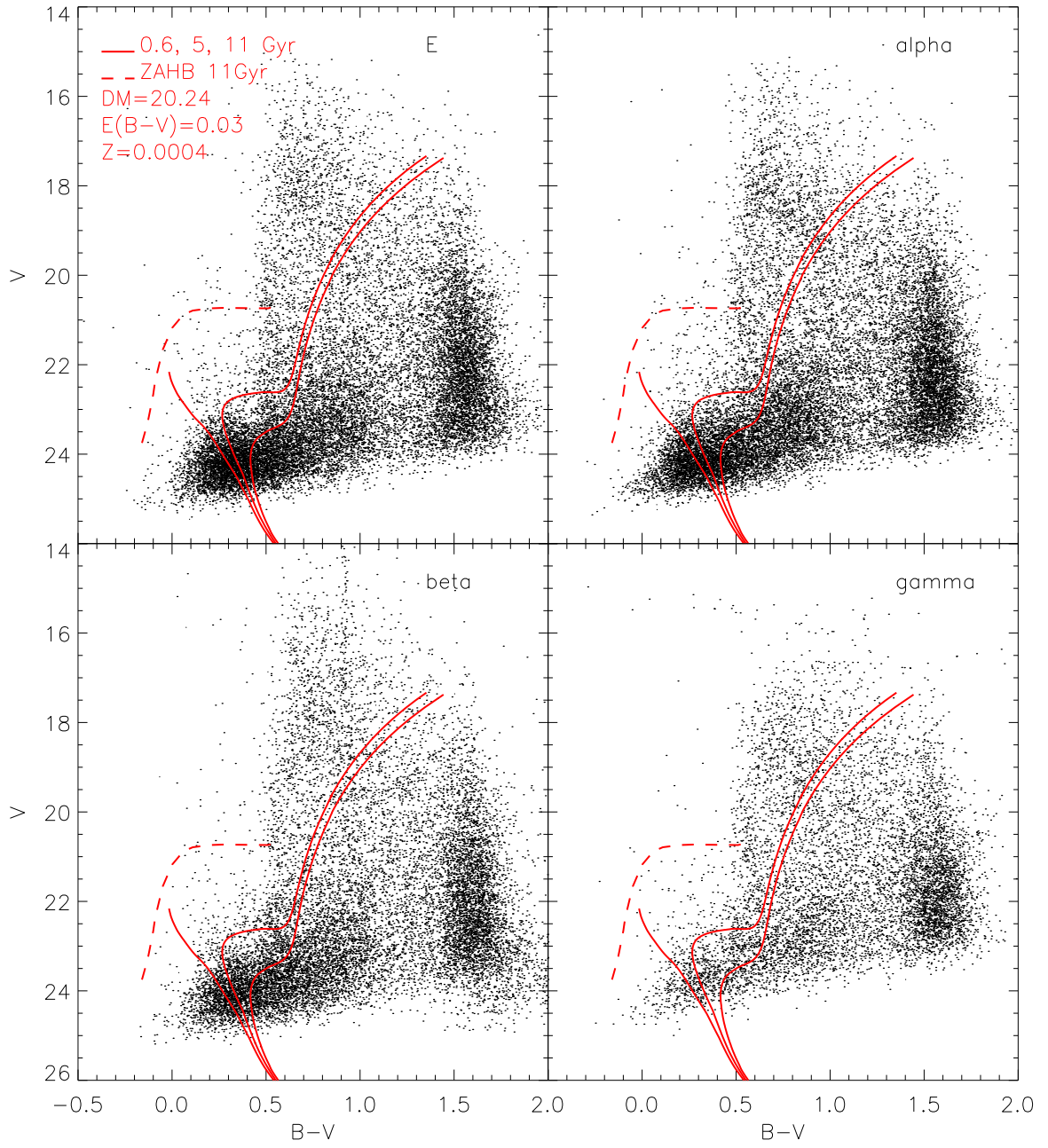


Figure 3.23: Cumulative CMD of field E,  $\alpha$ ,  $\beta$ ,  $\gamma$ . The theoretical tracks are the same used for the central region.

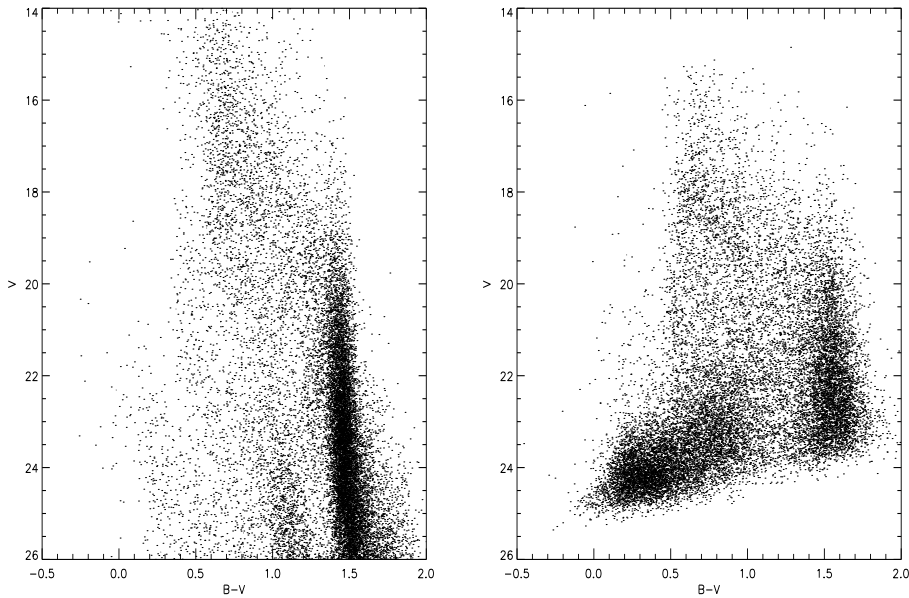


Figure 3.24: Left panel: theoretical predictions based on a Galactic models for the field  $\alpha$ . Right panel: the CMD of the same region of sky obtained from our data. The simulation takes into account the field of view of the data. Note that in the CMD region covered by blue spur stars are only present a few tens of disk white dwarfs.

a few tens of thick disk white dwarfs in the region corresponding to the blue spur. This supports the evidence that the blue spur is marginally populated by foreground WDs.

On the basis of current photometric data it is not possible to separate background galaxies from stars. Moreover, these objects are challenging to gather direct measurements of radial velocities, even with the multi-objects spectrographs mounted on a 8m class telescope (for example VIMOS or FORS). To solve this problem we decided to use color-color planes based on near-ultraviolet and optical data. Interestingly enough, we found that the  $(U-V)$  vs  $(B-I)$  colors allow a good separation between stars and galaxies. Fig. 3.25 shows galactic evolutionary tracks for different morphological types and redshift smaller than 2 (Fioc & Rocca-Volmerange 1997) together with three stellar samples, namely field stars (Pickles 1986), the old LMC globular cluster Reticulum (Monelli et al. 2003), middle), and NGC 2808 (Bedin et al. 2000), bottom. Data plotted in this figure show that the  $(U-V)$  vs  $(B-I)$  plane can be adopted to split stars from background galaxies, since they are distributed in different regions of the diagram. The plot also shows that the metal content only marginally affects this approach. In fact, the metallicity of the selected stellar samples ranges from solar (field)

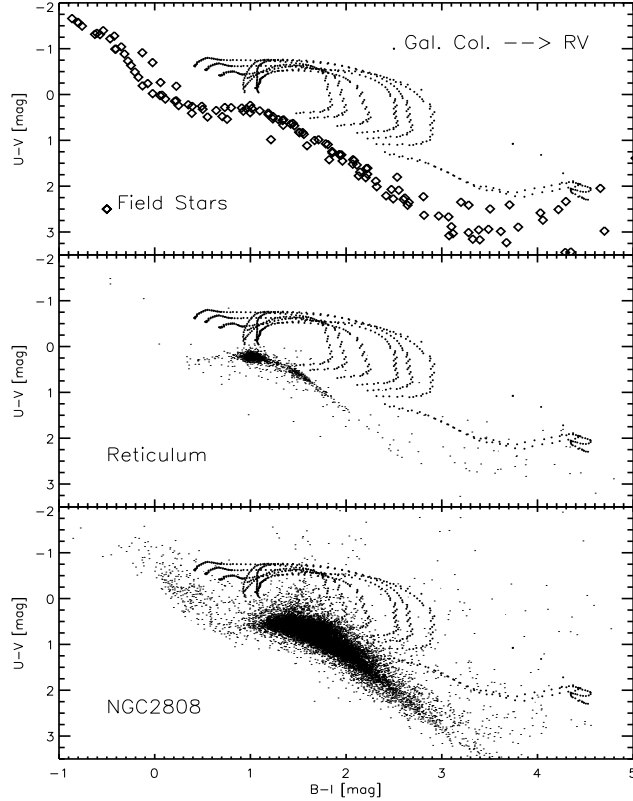


Figure 3.25: Color-color  $U - V$  vs  $B - I$  plane, comparing three samples of stars of different metallicities with evolutionary tracks for galaxies. These tracks account for different morphological types for redshift smaller than 2. Deep and accurate photometry in four bands will allow us to split stars from galaxies, if any.

to  $[\text{Fe}/\text{H}]=-1.7$  (Reticulum), and indeed all three samples are well separated from galactic tracks.

To test the reliability of this method, we collected new deep and accurate data in these four bands. We decided to observe two different regions: the center of Carina and the field located at  $1^\circ$  in the southern direction. Whatever the nature of the objects populating the blue spur, the latter field is the most appealing for this test. It is located at approximately  $2 r_t$ , and no Carina stars have been undisputedly detected at this distance from the centre. If we can confirm that the blue spur is populated by Carina stars it would be the first proof of extratidal stars in Carina. However, nothing can be assessed about the real extent of this galaxy, since the presence of the blue spur in the outer fields could support the existence of a diffused halo around Carina, in agreement with theoretical prediction by Hayashi et al. (2003).

In case we demonstrate that the blue spur is populated by background galaxies, we were forced to confirm previous results regarding the Carina extent,

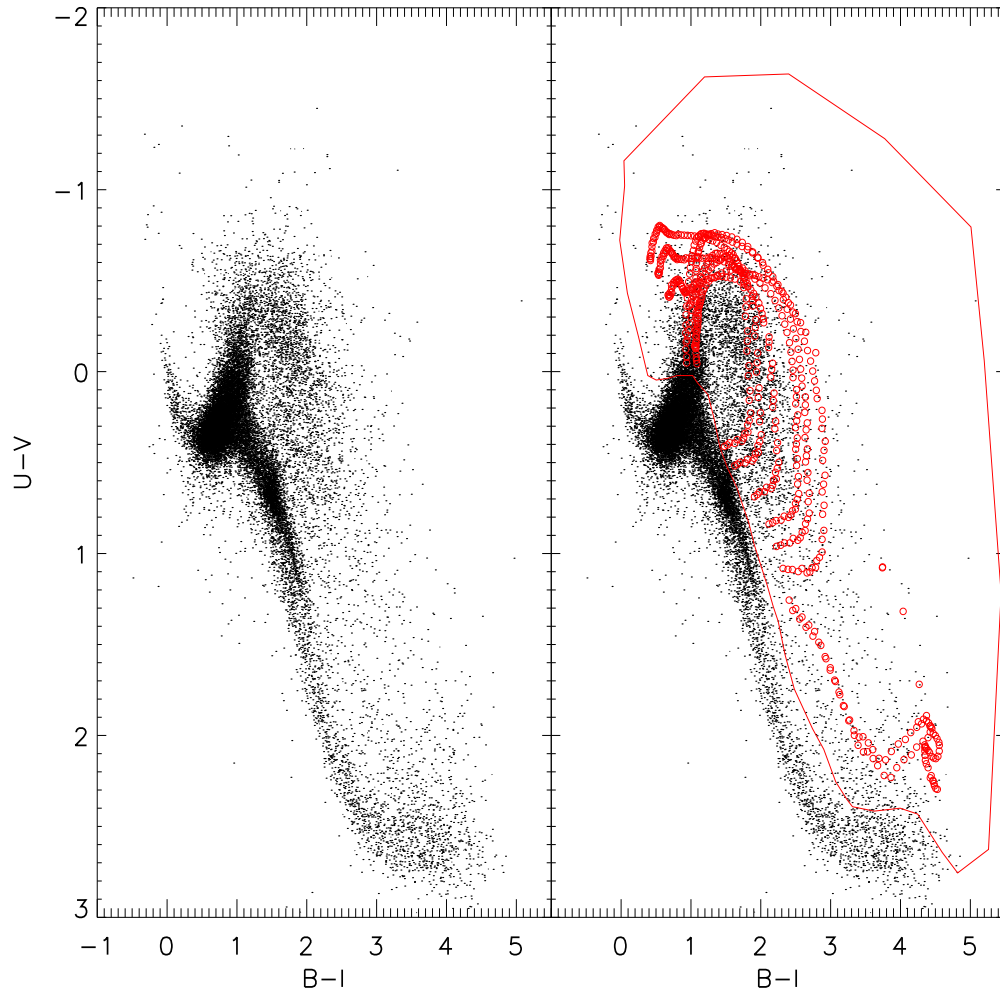


Figure 3.26: Left panel:  $(U-V)_{v_s}$   $(B-I)$  color-color diagram of the central region of Carina. The region where galaxies are expected to be is well populated by a few thousands of objects. Right panel: same as left panel, with superimposed both the galactic evolutionary tracks by Fioc & Rocca-Volmerange (1997) and the polygon used to select the candidate background galaxies

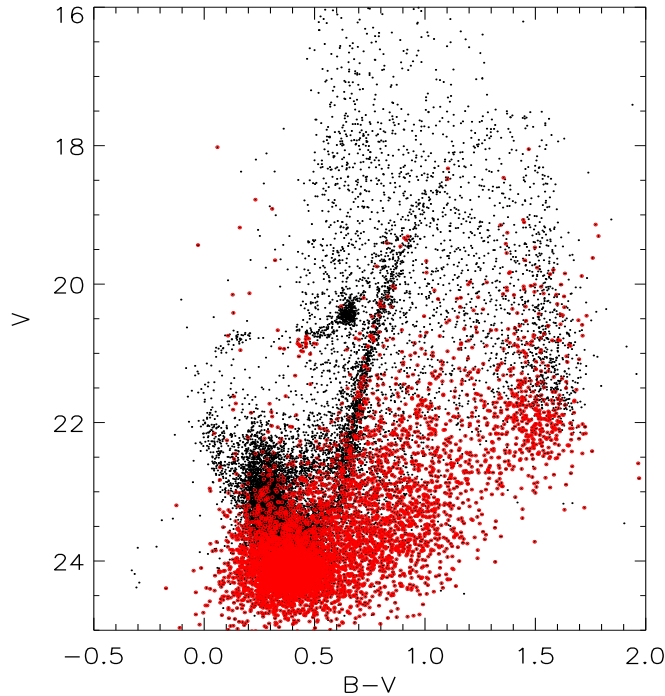


Figure 3.27:  $V$  vs  $B-V$  CMD with superimposed the selected objects. The region of the blue spur appears heavily contaminated by galaxies.

and the presence of this feature in the outer field would be the consequence of the isotropic distribution of galaxies. However, if the method works, we have devised a new diagnostic to split stars from galaxies, provided that deep and accurate multiband photometry is available. For this reason we selected the central field as second target of our experiment. It is the ideal field to compare the results obtained  $1^\circ$  away. If the spur is built up by background galaxies, they have to be present beyond the Carina centre, too. So the same feature must appear in the central region, and in principle it could be subtracted to obtain an even cleaner color-magnitude diagram.

Data were collected with the Blanco telescope during four half-night between December 2004 (central field) and January 2005 (field *E*, see tab. 3.5). Unfortunately, the weather conditions during the nights of 11 and 17 January were not good, with rapidly varying seeing and clouds. The data collected did not reach the expected limiting magnitude, in particular the *U* data.

The prereduction steps have been made with the usual IRAF tasks of the MSCRED environment (Valdes 1997). It is worth mentioning that a mask was built to correct for the fringing pattern in the *I* band. A median image was created using the less crowded scientific frames acquired during the night. The photometric reduction was performed with DAOPHOTII/ALLFRAME, working on the eight chips separately. All the *U* and *I* band

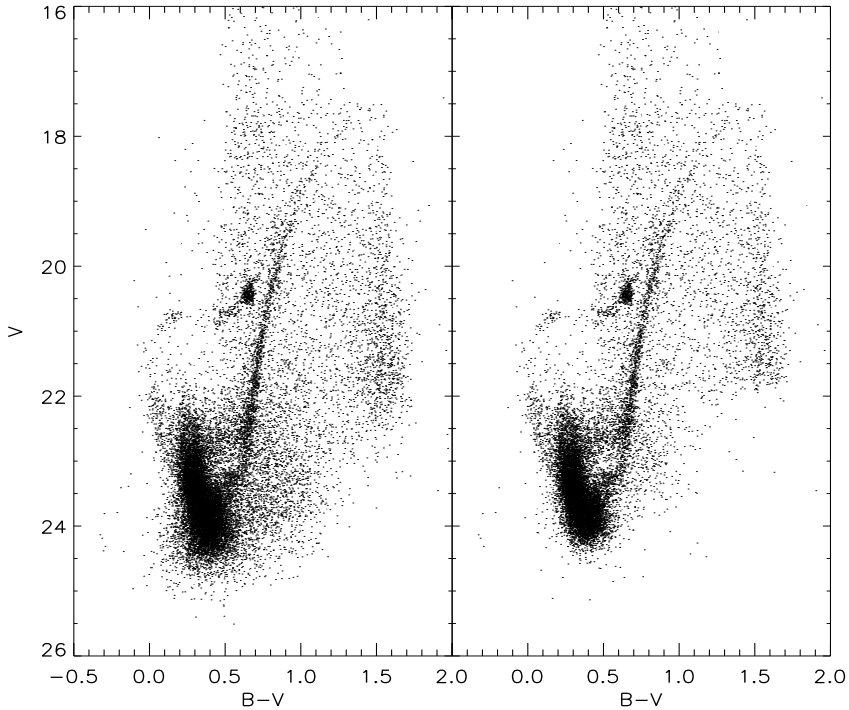


Figure 3.28:  $V$  vs.  $B - V$  CMD before (left) and after subtracting the suspected galaxies. Only the stars that have been detected in the four bands are plotted.

data collected during two night in Dec 2004 have been simultaneously reduced, while the data collected for the external field have been, at the time of writing, only reduced with ALLSTAR. Calibration frames of the standard field SA98 were acquired during the photometric nights, and the calibration curves were obtained using both Landolt (1992) as well as Stetson's standards (2004, private communication).

field name	RA (h)	DEC (deg)	total exposure time				D (")	telescope
			U	B	V	I		
central	06:41:38	-50:58:00	10000	21000	13200	7000	0	Blanco
E	06:41:38	-51:58:00	9350	7600	3000	8400	60	Blanco

Table 3.5: Summary of the observation collected in the four bands for the central and 1 degree south fields.

Figure 3.26 shows the color-color plane we obtained (left panel). The right panel shows the galactic evolutionary tracks from Fioc & Rocca-Volmerange (1997), and the polygon we used to select the candidate galaxies. The region is well populated and the catalogue of selected objects includes 5750

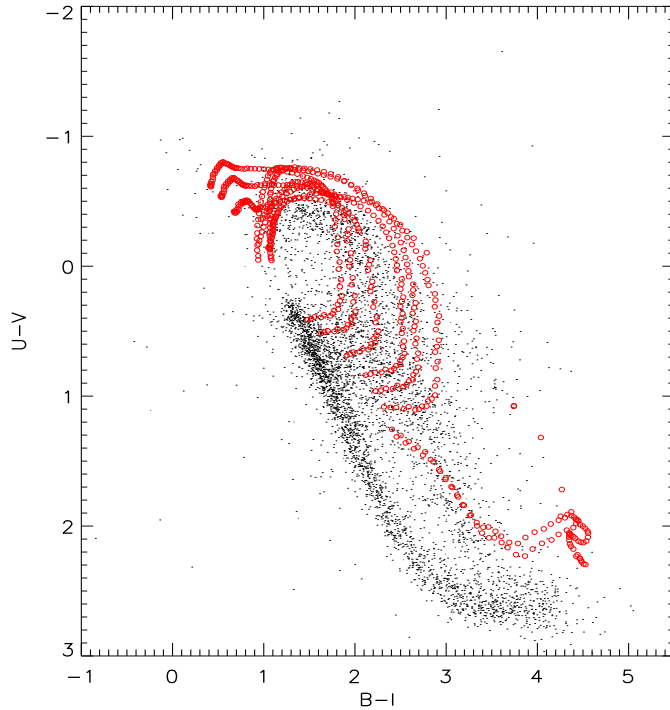


Figure 3.29: Color-color plane for the external field. We didn't detect objects in the blu region of the diagram, because of the bad quality of night.

possible galaxies.

Figure 3.27 shows the  $V$  vs  $B - V$  CMD of the objects that have been detected in the four bands. Red open circles indicated the sources selected from the color-color plane. Fig. 3.28 shows the same CMD before and after subtracting these objects. It is worth noting that the width in color of both old and intermediate-age MSs appears smaller in the right panel. This evidence is suggesting that the thickness of the MS is not entirely due to a spread in the chemical composition.

The same analysis cannot be performed on the external field, with the data at our disposal. Fig. 3.29 shows the  $(U-V)$  vs  $(B-I)$  plane, which discloses that no objects have been detected in the blue region of the diagram. The  $U$  data are too shallow to detect a sizable sample of objects populating the blue spur. New data are necessary for a meaningful comparison between the central and outer region, and estimate the fraction of background galaxies contaminating the CMDs.

### 3.2.6 Spectroscopic analysis of Carina stars

We collected low-resolution spectra of  $\approx 300$  stars belonging to both old and intermediate-age populations, to investigate their kinematical and chemical

properties. The targets were selected on the basis of the 4m CTIO data set (see fig. 3.30), and four fields around the Carina centre were observed with FORS2@VLT, with a spectral resolution  $R \approx 2000$ . The GRIS\_1400V+18 grism was adopted.

Standard data reduction, i.e. bias and flat field correction, has been performed with Iraf. The Iraf task APEXTRACT/APALL was used to extract the spectra, with interactively selected background sampling, in order to avoid contamination for the star spectrum. The wavelength calibration has been done using daily He, Ne, HgCd arcs, and, in order to improve the calibration, wavelengths values for the transitions used were taken from <http://physics.nist.gov/>.

The radial velocities were estimated by identifying a few lines (3 to 6, depending on the quality of the spectra) and fitting a Gaussian profile to each line to find the line core. We estimated the average radial velocity, and we present here only the stars with standard deviation of the mean less than  $7 \text{ km s}^{-1}$ .

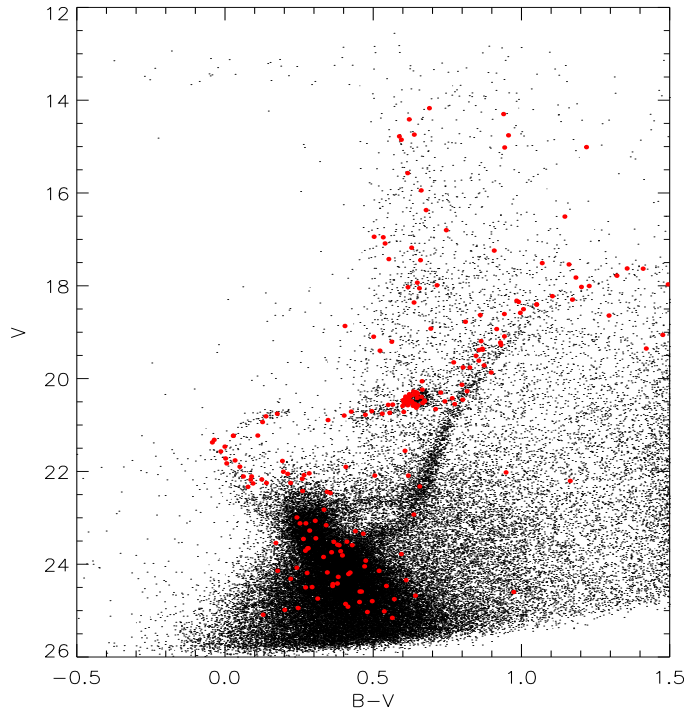


Figure 3.30: CMD showing the target selected for

Fig. 3.31 (left panel) shows the radial velocity distribution of selected stars. We estimate a main peak of  $V_r \approx 220 \pm 7 \text{ km s}^{-1}$ , in good agreement with previous measurements based on RGB stars Mateo (1998). A secondary peak appears at  $V_r \approx 180 \pm 7 \text{ km s}^{-1}$ . This dichotomy is shown in

the right panel of fig. 3.31, where the radial velocity is plotted as a function of the distance from the centre. These are very preliminary results, and the final sample of stars will be increased of a factor of 5. Previous spectroscopic surveys involving Carina stars were focused on the bright RGB stars only (Koch et al. 2004; Tolstoy et al. 2003). For the first time spectra were collected for stars of both the old population (HB, RGB) as well as intermediate-age objects (Red Clump). Moreover, spectra of a few young MS stars were collected. This will allow us to constrain the dynamical properties of different populations. At the same time, the analysis of chemical abundances will be performed.

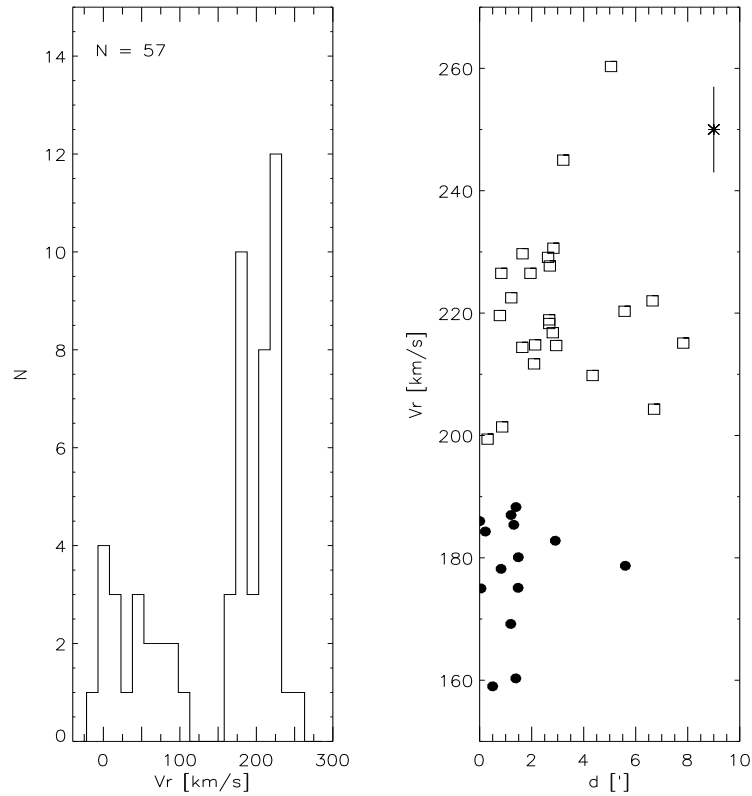


Figure 3.31: Left : distribution of the radial velocities. Right : radial velocity plotted as a function of the distance from the Carina center. Only stars with  $\sigma_v < 10\text{kms}^{-1}$  are considered in this analysis.

## Chapter 4

# The globular cluster Omega Centauri

### 4.1 General description

$\omega$  Cen is among the most studied object in the southern sky. However, there is no theoretical model which accounts for all the peculiarities of this cluster. It is located at about mid-distance from the Sun and the Galactic centre, with  $R_{\odot}=5.3$  kpc and  $R_{gc}=6.3$  Kpc, and it is the most massive ( $10^6 M_{\odot}$ , Meylan et al. 1995) and brightest ( $M_V \approx -10.3$ , Harris 1996) GGC. Clearly visible with the naked eye, it's apparent diameter is as big as twice the full moon.  $\omega$  Cen appears as a giant, rather nearby star cluster. However, the most surprising characteristic is the chemical inhomogeneity, and the fact that at least three different stellar populations coexist in  $\omega$  Cen. This is a unique feature among GCs, which makes  $\omega$  Cen much more similar to dSph galaxies rather than a globular cluster. Table 4.1 summarizes the average values for selected structural parameters of GGCs and dSphs. The comparison with  $\omega$  Cen shows that it can be considered as a "bridge" between globular clusters, which are not able to retain the gas ejected from their own massive stars, and the dwarf galaxies, which are the least massive self-enriching systems known (Meylan 1987). It is interesting to note that those dSphs that are less luminous than  $\omega$  Cen (e.g. Carina, Draco and Ursa minor) present a very modest abundance spread with respect to this cluster.

### 4.2 Distance and orbit

One of the first modern estimate of the  $\omega$  Cen's distance was derived by Noble et al. (1991), resulting in one of the largest value of the distance modulus published:  $(m - M)_V = 14.29 \pm 0.18$ . Harris (1996) gives a much lower value of  $(m - M)_V = 13.97$ , based on the work by Butler,

Characteristic	GC	$\omega$ Cen	dSphs
Mv	<0.9	-10	-8÷-13
Mass ( $M_{\odot}$ )	$10^5$	$10^6$	$10^6\div 10^8$
Ellipticity, $\epsilon = (1-b/a)$	<0.1	0.12	>0.13
$\Delta[\text{Fe}/\text{H}]$ , dex	<0.	$\approx 1$	0.2÷1.4

Table 4.1: Qualitative comparison between  $\omega$  Cen and globular cluster (Harris 1996) and dSphs (Irwin & Hatzidimitriou 1995; Mateo 1998). The properties of  $\omega$  Cen are intermediate between these two classes of objects.

Dickens & Epps (1978), who studied  $\approx 50$  RR Lyrae stars. This value is in good agreement with Djorgowski (1993), but two recent estimates are somehow at odds with previous results. Thompson et al. (2001), based on the infrared surface brightness of the eclipsing binary OGLE 17, obtained a larger distance modulus  $(m - M)_V = 14.05 \pm 0.11$ , while van Leeuwen et al. (2000) obtained a lower value of  $(m - M)_V = 13.27$  from the comparison of radial velocity and proper motion dispersions. This means that the  $\omega$  Cen distance value ranges from  $d=4.5\text{kpc}$  to  $d=5.4\text{kpc}$ .

The recent study of the proper motions by van Leeuwen et al. (2000) suggest a value of  $(\mu_x = -3.97 \text{ mas yr}^{-1}$  and  $\mu_y = -4.38 \text{ mas yr}^{-1}$ . This study, in agreement with Dinescu et al. (1999), supports the evidence that  $\omega$  Cen is moving in a strongly retrograde orbit, somewhat eccentric ( $e=0.67$ ) but confined on the Galactic plane ( $z_{max} = 1 \text{ kpc}$ ), with an apocentric radius of 6 kpc. This means that  $\omega$  Cen is actually close to its apogalacticon.

### 4.3 Structure and shape

$\omega$  Cen appears one of the flattest GGC, with a mean ellipticity  $\langle \epsilon \rangle = 0.121$ . However this value grows from  $\approx 0$  near the center up to  $\approx 0.25$  around  $10'$ , and then declines smoothly going outward (Geyer, Nelles & Hopp 1983). This profile is very similar to that of the velocity  $v_{rot}$ . This similarity supports the conclusion that the flattening of  $\omega$  Cen is due to its high degree of rotation. The position angle of the isophotes does not seem to change significantly with the distance from the centre, with the cluster elongated in the E-W direction.

The estimates of the core ( $r_c$ ), half-mass ( $r_h$ ), and tidal ( $r_t$ ) radii usually do not take into account the flatness of  $\omega$  Cen and these values should be considered as representative values averaged on the position angle (Merritt, Meylan & Mayor 1997). Many determinations of these parameters can be found in the literature. It is worth noting that there is general agreement around  $r_c \approx 3.7 \text{ pc}$  (Webbink 1995; Djorgowski 1993; Pryor & Meylan 1993), while the determinations of the  $r_h$  and  $r_t$  are more uncertain. In fact,

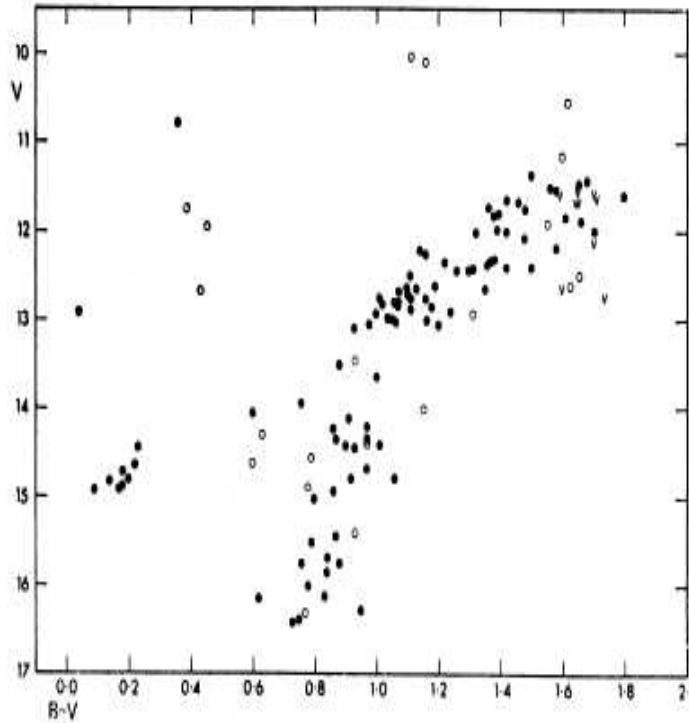


Figure 4.1: CMD by Cannon & Stobie (1973). Open circles indicate Galactic field stars.

the determinations of the tidal radius is intrinsically much more difficult, while the half-mass values are usually obtained from the half-light radius with semi-empirical formulae that add some uncertainty. In any case, the tidal radius of  $\omega$  Cen is quite large, ranging from 65.7 pc (Webbink 1995) to 87.4 pc (Richer et al. 1991): the concentration parameter  $c$  is quite small ( $c=1.24$ ). We can conclude that  $\omega$  Cen is a big cluster, but not very concentrated and quite far from the core collapse conditions.

#### 4.4 Multiple populations

Photographic photometry by Dickens & Wooley (1967) revealed for the first time the unusual color spread among RGB stars, which was later confirmed by photoelectric data by Cannon & Stobie (1973, see fig.4.1). As far as CCD technology was adopted, new deeper and more accurate CMD were obtained. Alcaïno & Liller (1987) and Noble et al. (1991) estimated the TO magnitude in excellent agreement at  $V=18.3$ . The first CMD of the very center of the cluster was obtained by Lyngå (1996), while deep HST data

by Pulone et al. (1998) and King & Anderson (2002) allowed to study the lower part of the MS, inferring the luminosity function down to  $\approx 0.2M_{\odot}$ . However, the modern era of photometric study of  $\omega$  Cen was opened by wide field studies like the ones by Lee et al. (1999) and by Pancino et al. (2000), which allowed to reveal the discrete nature of the RGB.

The wide RGB of  $\omega$  Cen was soon interpreted as an indication of intrinsic spread in the chemical abundance. The reddening is known to be fairly constant within the cluster field. This was largely proved by many authors (Burstein & Heiles 1982; Schlegel et al. 1998). Moreover, an ISO-CAM study by Origlia et al. (2002) confirms the absence of intracluster gas. The chemical inhomogeneity is the most noticeable characteristic that distinguishes  $\omega$  Cen from all the other globular cluster. In fact, globular clusters present a very small metallicity spread (entirely due to measurements error), while  $\omega$  Cen disclosed spread of at least  $1dex$ , that is an order of magnitude bigger than the typical globular cluster. Spectroscopic studies confirmed the hypothesis of an intrinsic spread of heavy elements. Butler, Dickens & Epps (1978) derived a metallicity range  $[Fe/H] = -2.2 \div -0.6$  by studying a vast sample of RR Lyrae stars. Similar values were obtained by Persson et al. (1996) from 82 RGB stars, and by Cannon & Stewart (1981), who investigated MS stars.

More recently, the low resolution survey of several hundreds of RGB stars conducted by Norris & Da Costa (1995) and Suntzeff & Kraft (1996), based on the H and K as well on the infrared triplet Ca II lines revealed a Metallicity Distribution Function as follows:

- there are just a few stars with  $[Fe/H] < -1.8$ ;
- the dominant peak in the distribution is located at  $[Fe/H] \approx -1.6$ ;
- a secondary peak is clearly visible at  $[Fe/H] \approx -1.2$ ;
- a long, asymmetric tail extends to high metallicity values, close to  $[Fe/H] \approx -0.5$ .

These values are in agreement with more recent surveys such as by Hilker & Richtler (2000) and Frinchaboy et al. (2004). Moreover, a new small component of very metal-poor stars ( $[Fe/H] < -2$ ) was discovered.

The discrete nature of RGB appeared evident from the wide field photometry by Lee et al. (1999) and Pancino et al. (2000). The former discovered multiple RGB's, and for the first time detected a new, redder, well-defined, and well-separated RGB (the so-called Anomalous RGB, *RGB-a*). Even if the stars populating this feature are bright, it was never identified before for the small statistics of previous works, and probably because the photometric accuracy was not enough. It was interpreted as a metal rich component, with  $[Fe/H] \approx -0.5$ , and many authors suggested a correlation between metallicity and age, being the RGB-a stars significantly younger ( $\approx 4Gyr$ ) than metal-poor stars. (Lee et al. 1999; Hughes & Wallerstein 2000; Hilker & Richtler 2000; Rey et al, 2000). In particular Rey et al, (2000), on the basis on the same data published by Lee et al. (1999), suggested a model in

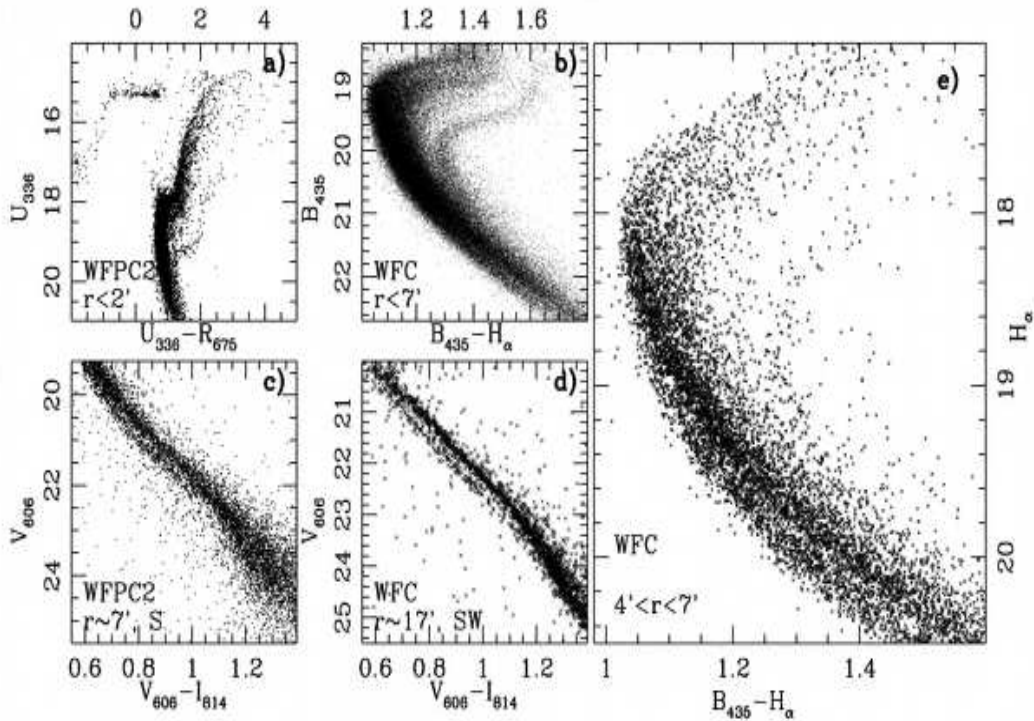


Figure 4.2: Fig. 1. from Bedin et al. (2004)

which four populations with different metallicities can reproduce the morphology of the RGB and HB. They determined the age-metallicity relation by comparing the observed HB distribution with the population models.

However, as far as new high quality data became available, new questions arose on the nature of this cluster. King & Anderson (2002), on the basis of deep multi-epoch HST photometry, disclosed that the MS is splitted in two components, which are hardly explained by the previous scenario. This bifurcation is itself puzzling. The existence of two separated MS seem to support the idea of two distinct population in  $\omega$  Cen. However, both spectroscopic and photometric data of evolved star indicate a spread in metallicity, rather than a net dicotomy. Moreover, the secondary sequence is much less populated and appears bluer than the main component. This is at odds with theoretical predictions of stellar evolution. In fact, assuming that all the stars in the two MSs are  $\omega$  Cen members, any canonical stellar model predicts that the blue MS must be more metal-poor than the red one, and this is at odds with what observed in the bright part of the diagram. More recently, new data collected with the ACS camera on board of HST

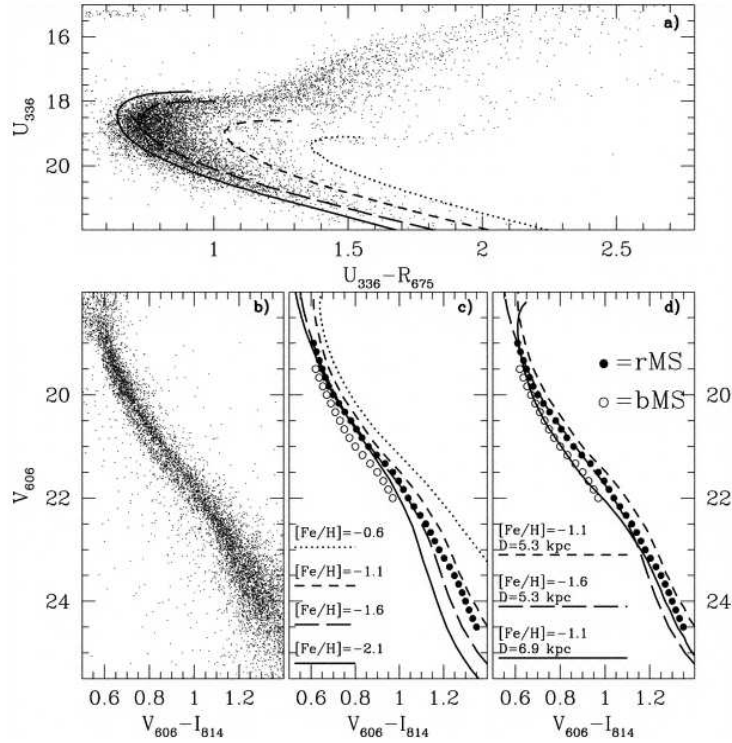


Figure 4.3: Fig. 2 from Bedin et al. (2004)

have stimulated the debate (Piotto et al. 2005). Ferraro et al. (2004) reported the discovery of a new sub-giant branch, which merges the MS at a magnitude level significantly fainter than the bulk of  $\omega$  Cen stars. Photometric data consist of a set of high resolution  $B, V, I$  images obtained with FORS1@VLT plus a set F435W, F625W, F658N ( $B, R, H_\alpha$ ) acquired with the ACS camera. In their CMD, the SGB-a appears as the natural continuation of the RGB-a. The TO of this population ( $R_{TO}$ ) appears significantly fainter than TO the more metal-poor stars. Then, by assuming that the SGB-a is the extension of the most metal-rich RGB, Ferraro et al. (2004) performed a detailed comparison with a set of theoretical isochrones calculated with the most up-to-date input physics (Straniero, Chieffi & Limongi 1998). They demonstrated, from a direct detection of the TO, that this anomalous, metal-rich population cannot be younger than the most metal-poor one.

More recently, Bedin et al. (2004) added new interesting features to this scenario. Fig. 4.2 show a composition of their CMD, obtained from HST data, from both the WFPC as well as the ACS cameras. They confirmed the split along the MS already discovered by King & Anderson (2002). Panel **b** of fig. 4.3 shows the MS in the F606W vs. (F606W-F814W) bands, with overplotted the isochrones representative of the cluster's population. The first thing to notice is that the red MS (rMS) is well fitted by the  $[Fe/H]=$

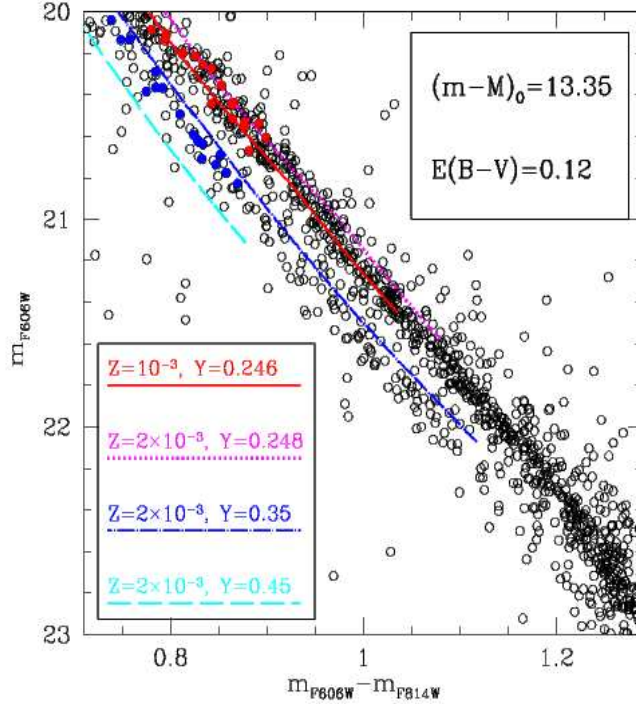


Figure 4.4: Fig. 7 from Piotto et al. (2005), showing the F606W vs (F606W-F814W) with superimposed the theoretical isochrones by Pietrinferni et al. (2004). Blu and red filled dots represent the spectroscopic targets. The best fit for the bMS is achieved with  $Z=0.02$  and  $Y=0.35$ .

1.6 curve. Second, the canonical models are not able to explain the blue MS (bMS). In order to explain the 0.06 mag  $V - I$  color difference we would have to assume a very metal-poor population ( $[Fe/H] \ll -2$ ), but it seems strange to admit the existence of such sizable sample of metal-poor MS stars with no evolved counterpart at all along the RGB. To force the model to fit the data, an arbitrary shift in color or magnitude should be applied. Four possible explanations have been suggested, but none of them seems fully satisfying.

- it is possible that the calibration and/or the isochrones are wrong. If we assume that the error in  $V - I$  is 0.06 mag, then the  $[Fe/H]=-1.6$  isochrone may fit the bMS. In this case the rMS would be counterpart of the metal-rich component, because the difference in the metallicity between the metal-poor and metal-intermediate component cannot explain a difference of 0.06mag. But this does not seem the case. The metal-rich component is a small fraction of the RGB ( $\approx 5\%$ ), but it would account for the 70% of MS stars. This huge difference in the mass function would be unexplained.

- if the rMS is made by metal-poor stars, then we have to admit that very metal-poor stars populate the blu one. However, Piotto et al. (2005)

demonstrated, using GIRAFFE@VLT spectra, that the bMS is more metal-poor than the red one than  $0.3 \pm 0.2$  dex.

- In the same paper, Piotto et al. (2005) support the hypothesis of different He enrichment between the two populations. They analysed medium resolution spectra of 17 stars from each sequence. They measured an intrinsic dispersion of 0.2dex in the rMS around the mean value of  $[M/H] = -1.57$ , while the bMS appears much more homogeneous around  $[M/H] = -1.26$ . With these value of the chemical composition, Piotto et al. (2005) used the theoretical isochrones by Pietrinferni et al. (2004) to fit the two MS (see fig. 4.4).

- If the rMS corresponds to the bulk of the cluster stars, then it is possible that the blue MS is associated with an object somewhat more distant beyond  $\omega$  Cen. Fig. 4.3, panel **d**, shows that an isochrone with  $[Fe/H] = -1$  would fit the bMS if the distance is increased by 1.6 Kpc.

## 4.5 Overview of the data sets

We present here multiwavelength photometry of  $\omega$  Cen. The data shown are part of a big project aimed at understanding the formation and evolution of this peculiar cluster. They are both proprietary as well as archive data, and have been collected with different telescopes: we present optical *UVI* (FORs1@VLT ESO), *BRH $\alpha$*  (ACS@HST) and infrared *JK* (SOFI@NTT ESO) data.

### 4.5.1 The VLT data

*U*, *V*, and *I* band images were collected with the FORs1 camera mounted on the UT1 (Antu) VLT telescope in Cerro Paranal, Chile, during two observing runs on April 23<sup>rd</sup> and June 1<sup>st</sup>, 1999 (ESO project 63.L-0686(A)). The standard resolution of the camera,  $0.2''/\text{px}$ , was adopted, and the observations were characterized by good seeing ( $0.4''$  to  $0.8''$ ). The field of view of the CCD is  $6.8' \times 6.8'$ , and hence a mosaic of four pointings around the  $\omega$  Cen centre was chosen to sample the cluster for more than 2 core radii. The four fields are mildly overlapped, and the total field of view is  $\approx 14' \times 14'$ . Fig. 4.5 shows the fields observed with the three instruments, while tab. 4.1 summarizes the log of the observations.

The prereduction has been performed by Lars Freyhammer, paying particular attention on the cross-talk effect due to the multi-channel CCD (Freyhammer et al. 2001). The PSF was derived for each single frame, with the same procedure described for the Carina data. The photometric reduction has been performed with DAOPHOTII/ALLFRAME, each of the four pointings has been studied separately including all the images available.

A median image was built for each field, in order to cancel out cosmic rays and to raise the S/N ratio of faint object. The master list of star required

field name	RA (h)	DEC (deg)	MJD	filter	expos. (sec)	seeing (")	angle (°)
F1	13:26:27.7	-47:25:32.9	291.16312	I	10	0.73	90
F1	13:26:27.7	-47:25:32.9	291.15766	I	10	0.67	0
F1	13:26:27.7	-47:25:32.9	291.16206	V	11	0.74	90
F1	13:26:27.7	-47:25:32.9	291.15660	V	11	0.74	0
F1	13:26:27.7	-47:25:32.9	291.16555	U	30	0.93	90
F1	13:26:27.7	-47:25:32.9	291.15522	U	30	1.03	0
F2	13:26:27.7	-47:32:00.9	291.15210	I	10	0.77	0
F2	13:26:27.7	-47:32:00.9	291.14403	I	10	0.70	90
F2	13:26:27.7	-47:32:00.9	291.13872	V	11	0.83	0
F2	13:26:27.7	-47:32:00.9	291.14170	V	11	0.95	90
F2	13:26:27.7	-47:32:00.9	291.13311	U	30	0.85	0
F2	13:26:27.7	-47:32:00.9	291.14286	U	30	0.88	90
F3	13:27:05.8	-47:32:00.9	291.22107	I	10	0.49	0
F3	13:27:05.8	-47:32:00.9	291.22821	I	10	0.52	90
F3	13:27:05.8	-47:32:00.9	291.22000	V	11	0.49	0
F3	13:27:05.8	-47:32:00.9	291.22576	V	11	0.53	90
F3	13:27:05.8	-47:32:00.9	291.21861	U	30	0.48	0
F3	13:27:05.8	-47:32:00.9	291.22692	U	30	0.61	90
F4	13:27:05.8	-47:25:32.9	291.23455	I	10	0.47	0
F4	13:27:05.8	-47:25:32.9	291.24091	I	10	0.67	90
F4	13:27:05.8	-47:25:32.9	291.23350	V	11	0.56	0
F4	13:27:05.8	-47:32:32.9	291.23847	V	11	0.55	90
F4	13:27:05.8	-47:32:32.9	291.23211	U	30	0.65	0
F4	13:27:05.8	-47:32:32.9	291.23963	U	30	0.67	90
F4	13:26:56.2	-47:27:10.0	330.17306	I	20	0.67	90

Table 4.2: Log of the data collected with FORS1. Note that 4 images were secured per each filter. Note that a couple of images (per field, per filter) have been rotated by 90 degrees.

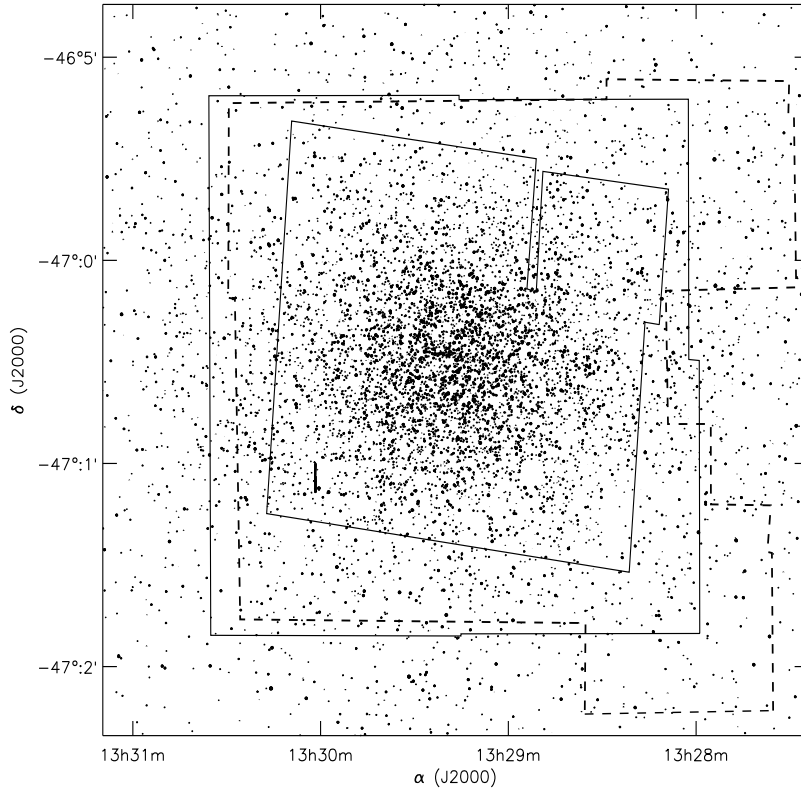


Figure 4.5: Field of the central regions of  $\omega$  Cen. We overplotted the field of view of all our datasets. Solid thin line encloses the ACS@HST field, while the solid thick line shows the field of view of the VLT images. The dashed line is referred to the IR data collected with SOFI@NTT.

by ALLFRAME was made on each median image. The final catalogues have been calibrated using standard fields collected during the run, and then rescaled on a common grid of coordinates. We ended up with a list of  $\approx 450000$  stars. CMDs for a selected sample of stars are shown in fig. 4.6

#### 4.5.2 The HST data

ACS on board on HST is a  $4K \times 4K$  CCD, with an unprecedented spatial resolution. The Wide Field Camera used in this work has a field of view of  $3.4' \times 3.4'$  and a pixel scale of  $0.05''/\text{px}$ .  $F435W$ ,  $F625W$  and  $F658N$  images (hereinafter  $B$ ,  $R$  and  $H_\alpha$ ), were retrieved from the HST archive. Nine different pointings map the central regions of  $\omega$  Cen, for a total field of view of  $\approx 9' \times 9'$ .

Fig. 4.7 shows the resulting CMDs. The features are well represented, from the upper part of the RGB down to 8mag below the MSTO. The WD cooling sequence is populated by a few thousands of objects.

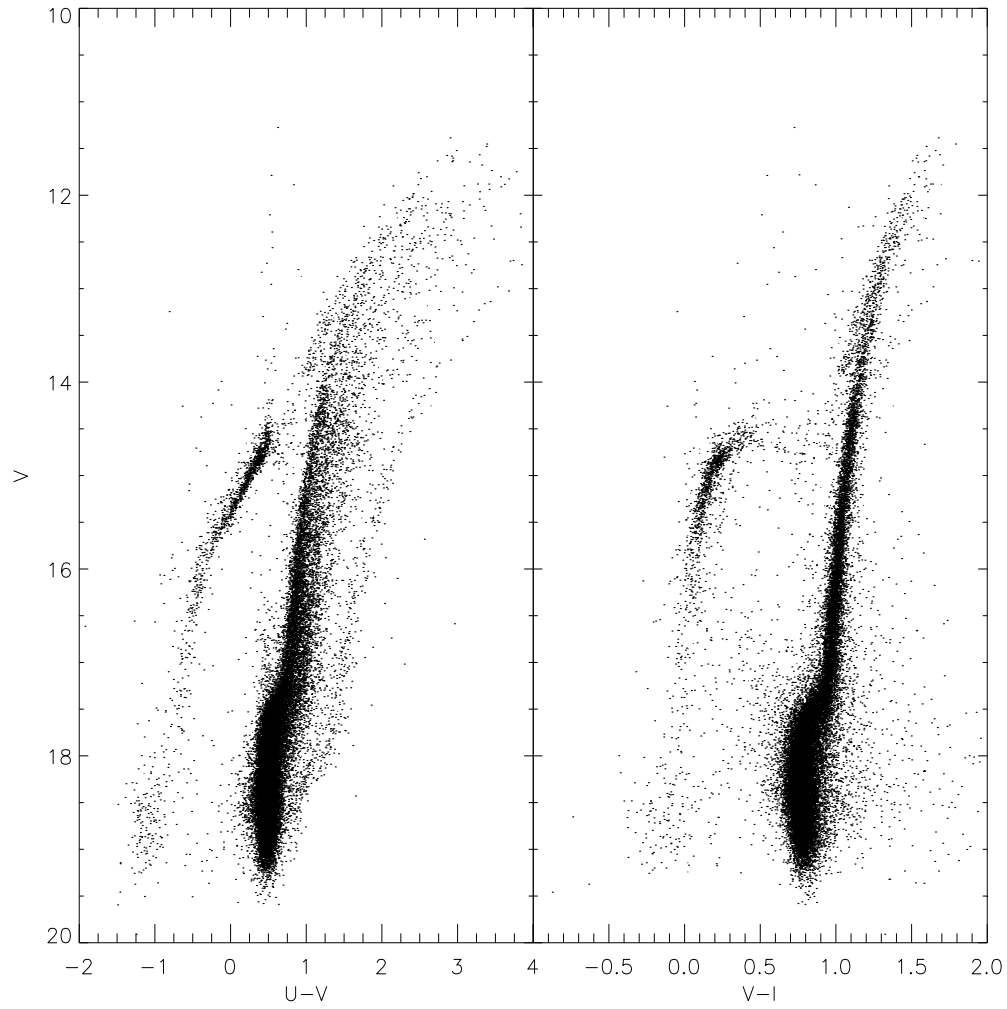


Figure 4.6: CMD from the VLT dataset. The catalogue has been selected with the *separation* index. The anomalous RGB appears well separated in the  $V, U - V$  plane.

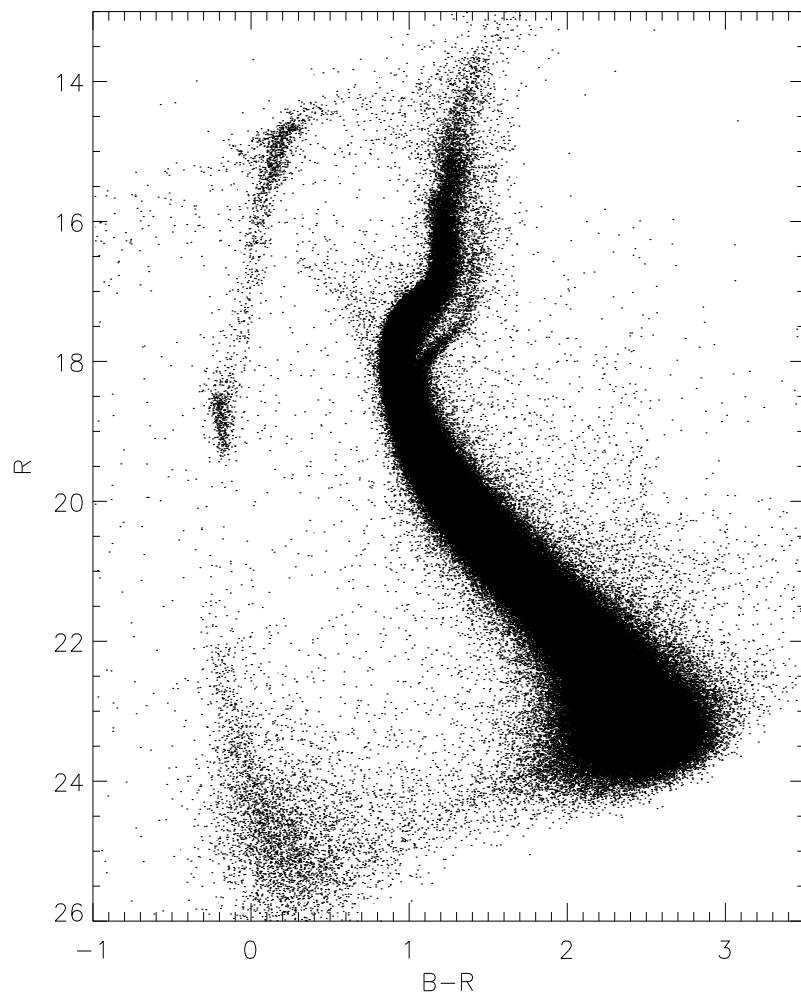


Figure 4.7:  $R$  vs  $B - R$  CMD of  $\approx 900,000$  stars, selected according to the photometric error and the sharpness parameter.

archive name	RA (h)	DEC (deg)	filter	exp. time (sec)
F1	13 26 27.99	-47 25 34.5	F435N	12., 3X440
F1	13 26 27.99	-47 25 34.5	F625W	8., 3X340
F1	13 26 27.99	-47 25 34.5	F658N	4X440
F2	13 26 29.31	-47 28 47.6	F435W	12., 3X440
F2	13 26 29.31	-47 28 47.6	F625W	8., 3X340
F2	13 26 29.31	-47 28 47.6	F658N	4X440
F3	13 26 30.63	-47 32 00.8	F435W	12., 3X440
F3	13 26 30.63	-47 32 00.8	F625W	8., 3X340
F3	13 26 30.63	-47 32 00.8	F658N	4X440
F4	13 26 48.31	-47 31 34.2	F435W	12., 3X440
F4	13 26 48.31	-47 31 34.2	F625W	8., 3X340
F4	13 26 48.31	-47 31 34.2	F658N	4X440
F5	13 26 46.97	-47 28 21.1	F435W	12., 3X440
F5	13 26 46.97	-47 28 21.1	F625W	8., 3X340
F5	13 26 46.97	-47 28 21.1	F658N	4X440.
F6	13 26 45.63	-47 25 08.0	F435W	12., 3X440
F6	13 26 45.63	-47 25 08.0	F625W	8., 3X340
F6	13 26 45.63	-47 25 08.0	F658N	4X440
F7	13 27 04.73	-47 24 39.1	F435W	12., 3X440
F7	13 27 04.73	-47 24 39.1	F625W	8., 3X340
F7	13 27 04.73	-47 24 39.1	F658N	4X440
F8	13 27 06.09	-47 27 52.2	F435W	12., 3X440
F8	13 27 06.09	-47 27 52.2	F625W	8., 3X340
F8	13 27 06.09	-47 27 52.2	F658N	4X440
F9	13 27 07.44	-47 31 05.3	F435W	12., 3X440
F9	13 27 07.44	-47 31 05.3	F625W	8., 3X340
F9	13 27 07.44	-47 31 05.3	F658N	4X440

Table 4.3: Log of the ACS@HST data retrieved from the STSCI archive.

### 4.5.3 Infrared observations

Near-infrared  $J$  and  $K_s$  images of  $\omega$  Cen were collected in two different runs, the first on 5 and 7 February 2001, and the second during four non-consecutive nights in February 2002, using the SOFI camera mounted on the Nasmyth focus of the NTT ESO telescope. This 1K $\times$ 1K camera has a pixel scale of 0.292"/px, resulting in a field of view of 4.94' $\times$ 4.94'. We observed three different fields. The exposure times were 3s in  $J$  with NDIT=1 and 3s in  $K_s$  with NDIT=3. The NDIT on-chip integrations were averaged by the SOFI acquisition system. We alternated observations of  $\omega$  Cen with observations of the sky, to properly subtract the background.

Moreover, we retrieved  $J$  and  $K_s$  frames from the ESO archive, i.e. a mosaic of nine pointings partially overlapping, for a total area of  $\approx 13' \times 13'$  around the cluster center. These images were obtained during the nights of 12 and 13 January 2000. seven of these fields were observed once in the  $J$  as well as in the  $K_s$  band, with exposure times of 54s (NDIT=45) and of 180s (NDIT=150), respectively. The last two fields, the first on the center and the second at a distance of  $\approx 3'$  were observed twice. One exposure of the central field was shorter, namely 18s and 54s for the  $J$  and  $K_s$  respectively. The prereduction and reduction of the data has been performed by M. Del Principe and A. Piersimoni. IRAF procedures were applied for differential flat-fields and the relative illumination correction. All the photometric measurements were carried out with the DAOPHOT/ALLFRAME package. More than 50 stars were used to derive the individual PSF. Several tests were performed, and the best results were obtained with a linearly variable PSF. A few  $V$  and  $I$  band from the VLT dataset were reduced together with  $J$  and  $K_s$ , in order to obtain a better determination of the centroid of the star. The final list of stars included 120,000 objects, with limiting magnitude  $J \approx 20.5$ mag and  $K_s \approx 20$ mag. The absolute calibration was performed using the standard stars S971-C, S8670-V, S273-R, and S870-T from Persson et al. (1996). The derived calibration curves are the following:

$$J = j + K_j * X + 2.036 \pm 0.007$$

$$K = k + K_k * X + 2.686 \pm 0.008$$

where  $j$  and  $k$  are the instrumental magnitudes, and  $J$  and  $K_s$  are the calibrated ones,  $X$  is the airmass. The extinction coefficient,  $K_j=0.08$  and  $K_k=0.11$ , were provided by the ESO staff.

The resulting CMD is presented in fig. 4.8. The main features are:

- all the evolved phases are well represented, and the MS reaches a magnitude 3mag fainter than the TO.
- The AGB is well populated and clearly distinct from the RGB.
- The HB is well defined, and the RR Lyrae instability strip is well populated.

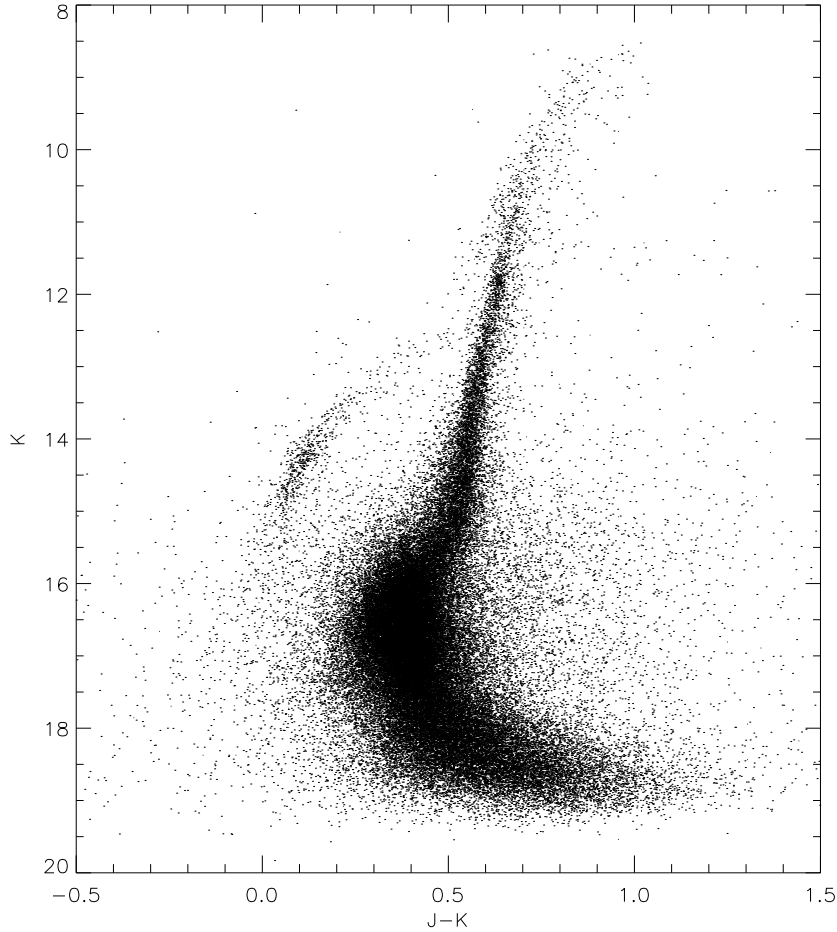


Figure 4.8:  $K$  vs  $J - K$  CMD of  $\omega$  Cen. The RGB-Bump has been detected at  $K_s \approx 11.8$  (Del Principe et al. 2004, priv. comm.).

- The RGB-Bump is evident, and differential luminosity function suggest a value  $K_{bump}=11.8$ .

#### 4.5.4 Tidal tails in $\omega$ Cen?

A big effort has been devoted to gather all the information from the previous data sets. Since all the data obtained from different telescopes have been reduced independently, the final catalogue of stars has been built *a posteriori*, rescaling the photometry on a common coordinate system. To do this, DAOMATCH and DAOMASTER were adopted. The final list includes 7 photometric bands, from the  $U$  to the  $K_s$  band. In the absence of conformity in the literature for the  $\omega$  Cen RGB names, we here refer to the metal-poor component as  $\omega 1$ , to the metal-intermediate as  $\omega 2$ , and to the anomalous branch as  $\omega 3$ .

Fig. 4.9 shows CMDs based on the five different photometric bands. The plotted stars were selected from individual catalogues by using the ‘separation index’  $sep$  introduced by Stetson et al. (2003), since crowding errors dominate the photometric errors. This parameter estimates, per each star, the flux contamination due to nearby objects. The adopted  $sep$  ranges from 6.5 (NIR data) to 8 (ACS data), which corresponds to stars having less than 0.3% of their measured light contaminated by neighbour stars; the higher the  $sep$  for a star, the less the severity of the crowding by neighbours. Error bars plotted at the left side of each panel account for photometric and calibration errors in magnitude and color. The input physics adopted in our evolutionary code has been discussed in detail in a series of papers (Cariulo et al. 2004; Cassisi et al. 1998). Here, it is worth mentioning that the stellar models (partly available at <http://astro.df.unipi.it/SAA/PEL/Z0.html>) account for atomic diffusion, including the effects of gravitational settling, and thermal diffusion with diffusion coefficients given by Thoul et al. (1994). The amount of original He is based on a primordial He abundance  $Y_P = 0.23$  and a He-to-metals enrichment ratio of  $\Delta Y/\Delta Z \sim 2.5$  (Pagel & Portinari 1998; Castellani & Degl’Innocenti 1999). We adopt the solar mixture provided by Noels & Grevesse (1993). For details on the calibration of the mixing length parameter and on model validation, see Cariulo et al. (2004) and Castellani et al. (2003). To avoid deceptive uncertainties in the comparison between theory and observations, the predictions were transformed into both the  $BR$  Vega system and the  $IJK$  Johnson-Cousins bands by adopting the atmosphere models provided by Castelli et al. (1997) and Castelli (1999). Data plotted in 4.9 display the comparison between observations and a set of four isochrones (solid lines) with the same age (12 Gyr) and different chemical compositions (see labels). A mean reddening of  $E(B - V) = 0.12$  ( $E(B - V) = 0.11 \pm 0.02$ , Lub 2002) was adopted and a true distance modulus of  $\mu = 13.7$  ( $(m - M)_V = 14.05 \pm 0.11$ ; Thompson et al. (2001),  $(m - M)_K = 13.68 \pm 0.07$ , Del Principe et al. 2004, priv. comm.). Extinction parameters for both optical and NIR bands have been estimated using the extinction model of Cardelli et al. (1989). The metal-poor and the metal-intermediate isochrones supply, within current empirical and theoretical uncertainties, a good fit to the bulk of RGB and HB stars. Close to the RGB tip, the isochrones are slightly brighter than the observed stars, which is caused by the adopted mixing-length parameter ( $\alpha = 2$ ). The SGB and the lower RGB are only marginally affected by this parameter, since the empirical isochrone calibration is based on these evolutionary phases (Cariulo et al. 2004). However, the most metal-rich isochrone appears to be systematically redder than the stars at the base of the  $\omega 3$  branch<sup>1</sup> (green dots) and fainter than the SGB stars. Clearly, the shape of the  $\omega 3$  SGB

---

<sup>1</sup>Stars of the  $\omega 3$  branch have been selected following the original detection in the  $B - R, R$  plane by (Ferraro et al. 2004, see their fig. 2)

does not support metal-abundances  $\geq Z = 0.004$ , since TO stars for more metal-rich populations become brighter than SGB stars. To further constrain this evidence, fig. 4.10 shows the comparison between observed HB stars (the entire sample includes more than 2,300 objects) and predicted Zero Age Horizontal Branches (ZAHBs) with a progenitor age of 12 Gyr and different chemical compositions. For the sake of the comparison, the objects located between hot HB stars and RGB stars were selected in the  $B - R$ ,  $B$  plane and plotted as blue dots. Theoretical predictions plotted in this figure show that the more metal-rich ZAHB appears to be systematically brighter than the observed HB stars for  $B - J \approx B - K \approx 0.5$ . Moreover, the same ZAHB crosses the RGB region, thus suggesting that the occurrence of HB stars more metal-rich than  $Z=0.002$  should appear as an anomalous bump along the RGB. Data plotted in these figures disclose that *the stellar populations in  $\omega$  Cen cannot be explained with a ranking in metal abundance*. In line with Ferraro et al. (2004) and Bedin et al. (2004), we find that plausible changes in the cluster distance, reddening, age, and chemical composition do not supply a reasonable simultaneous fit of the  $\omega 1$ ,  $\omega 2$ , and  $\omega 3$  branches.

To further investigate the nature of the  $\omega 3$  branch, we performed a series of tests by changing the metallicity, the cluster age, and the distance. A good fit to the anomalous branch is possible by adopting the same reddening as in fig. 4.9, a true distance modulus of  $\mu = 13.9$ , and an isochrone of 15.5 Gyr with  $Z = 0.0025$  and  $Y = 0.248$ . Figure 4.11 shows that these assumptions supply a good fit in both the optical and the NIR bands, and indeed the current isochrone properly fits the width in color of the sub-giant branch and the shape of a good fraction of the RGB. Moreover, the ZAHB for the same chemical composition (dashed line) agrees quite well with the faint component of HB stars. Note that more metal-poor ZAHBs at the canonical distance do not supply a reasonable fit of the yellow spur stars with  $15 \leq B \leq 15.5$ . The yellow spur is visible in all planes, and in the NIR (**c**, **d**) it even splits up in brightness due to a stronger sensitivity to effective temperature. The identification of the entire sample was checked on individual images and, once confirmed by independent measurements, the data indicate a separate HB sequence for the  $\omega 3$  population.

Although the  $\omega 3$  fit may appear good, it implies an increase in distance of  $\Delta\mu = 0^m2$  and an unreasonable  $\sim 4$  Gyr increase in age. This estimate is at variance with the absolute age estimates of GGCs (Gratton et al. 2003) and with CMB measurements by W-MAP (Bennett et al. 2003). The discrepancy becomes even larger if we account for the fact that this isochrone was constructed by adopting a He abundance slightly higher ( $Y = 0.248$ , vs 0.238) than estimated from a He-to-metals enrichment ratio  $\Delta Y/\Delta Z = 2.5$ . This increase implies a decrease in age of  $\sim 1$  Gyr. Moreover, we are performing a differential age estimate, and therefore if we account for uncer-

ainties: in the input physics of the evolutionary models (e.g. equation of state, opacity); in the efficiency of macroscopic mechanisms (like diffusion); in model atmospheres applied in the transformation of the models into the observational plane; and in the extinction models, we end up with an uncertainty of  $\sim 1 - 2$  Gyr in cluster age (Castellani & Degl’Innocenti 1999; Krauss & Chaboyer 2003).

Owing to the wide range of chemical compositions and stellar ages adopted in the literature for explaining the morphology of the  $\omega 3$  branch, we decided to investigate whether different combinations of assumed values of distance, chemical composition, and reddening may also simultaneously account for the  $\omega 3$  branch and the HB stars. We found that two isochrones of 13 Gyr for  $Z = 0.0015$  and  $Z = 0.003$  bracket the  $\omega 3$  stars (see fig. 4.12), within empirical and theoretical uncertainties. The fit was obtained using the same true distance modulus adopted in fig.4.11, together with a mild increase in reddening,  $E(B - V) = 0.155$ . Once again theory agrees reasonably well with observations in all color planes. Moreover, data plotted in fig. 4.13 show that the predicted ZAHB with  $Z=0.0015$  and  $Z=0.003$ , for the adopted distance modulus and reddening correction, account for the yellow spur stars. The same figure shows a sample of 53 RR Lyrae stars selected from the variable-star catalogue by Kaluzny et al. (2004) for which we have a good coverage of  $J$ - and  $K$ -band light curves (Del Principe et al. 2004, private communication). The RR Lyrae stars only account for a tiny fraction of the yellow-spur stars. This finding together with the detection a well-defined sequence in panels **b,c**, and **d** indicate that this spur might be the HB associated with the  $\omega 3$  population. Note that a few of these ‘ $\omega 3$ -HB’ spur stars have also been detected by (Rey et al, 2000, see their fig. 7), for  $V \approx 14.75$ ) and by (Sollima et al. 2004, see their figs. 6 and 12).

## 4.6 White dwarfs in $\omega$ Cen

The detection of WDs in  $\omega$  Cen dates back to Ortolani & Rosino (1987) who selected two dozen WD candidates on the basis of ground-based data, and to Elson et al. (1995), who detected four WD candidates using HST data. Our color-magnitude diagram, based on the ACS data, discloses a well populated sequence of stars at  $B - R \approx 0$  and  $R < 22$ , that is bluer than MS stars and fainter than extreme HB stars. We ended up with a sample of approximately 45,000 stars. These stars have been identified in individual deep  $B, R, H_\alpha$  images and we performed once again the photometry using ROMAFOTwo. Individual stars have been interactively checked in every image, and the magnitude was simultaneously estimated together with neighbor stars which might affect the photometry. Note that more than 50% of selected stars revealed to be either cosmic rays or spurious identifications of faint stars located close to saturated stars. The photometric calibration was performed

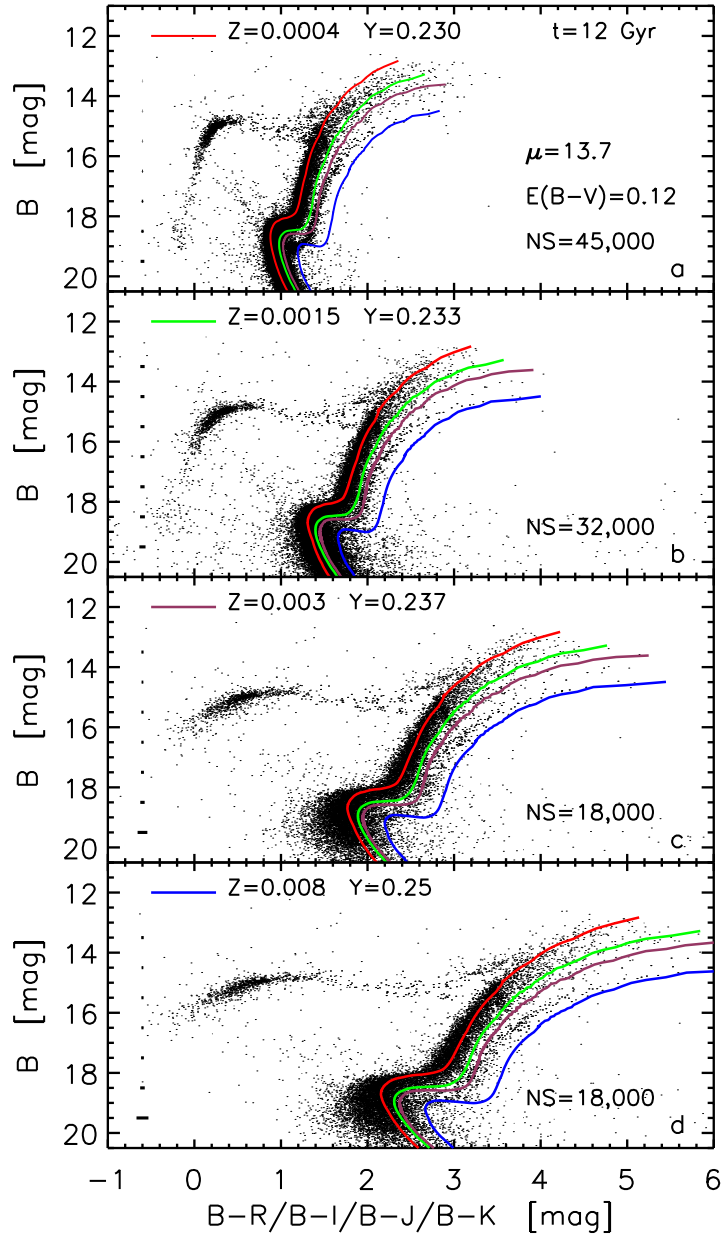


Figure 4.9: Optical (panels **a**,**b**), and NIR (panels **c**,**d**) CMDs for selected subsamples of the detected stars, compared with a set of 12 Gyr isochrones (solid lines) at different chemical compositions (see color coding). The adopted true distance modulus and cluster reddening are  $\mu = (m - M)_0 = 13.7$  and  $E(B - V) = 0.12$ , respectively. The number of stars selected (NS) is also indicated.

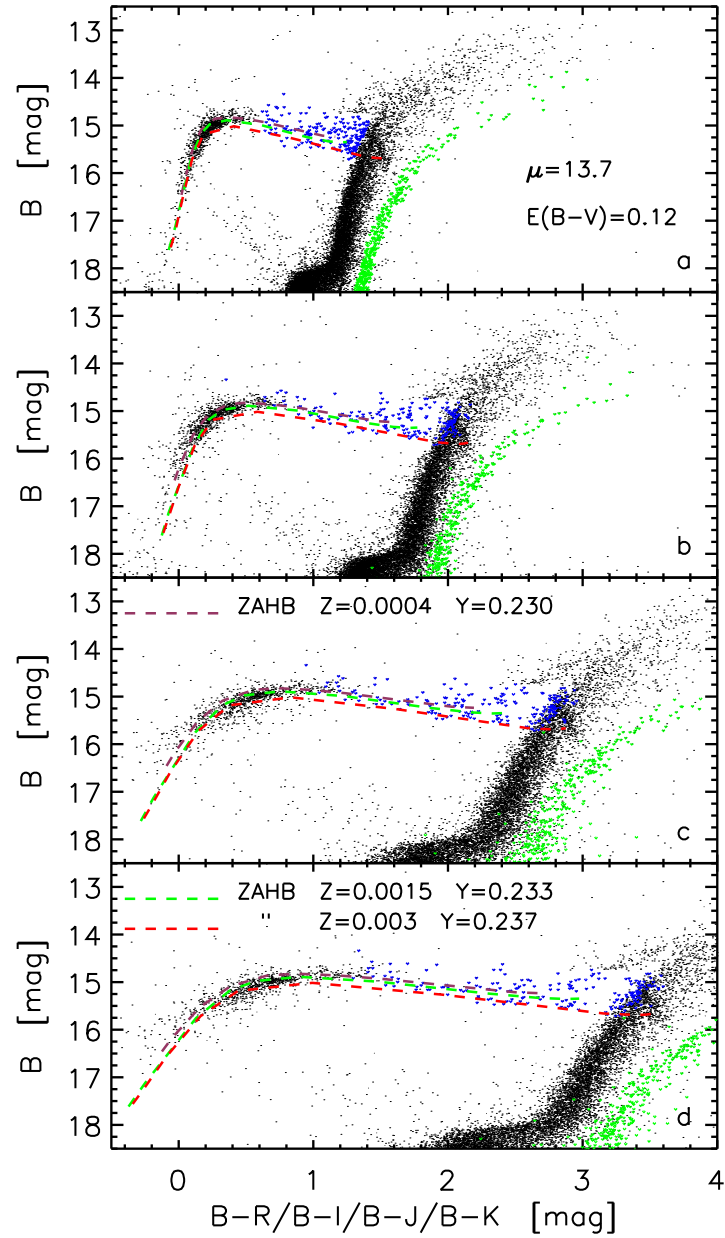


Figure 4.10: Same as in fig. 4.9, but the comparison between theory and observations is focused on Horizontal Branch stars. Blue objects mark stars located between hot HB stars and RGB stars. They have been selected in  $B - R, B$  plane.

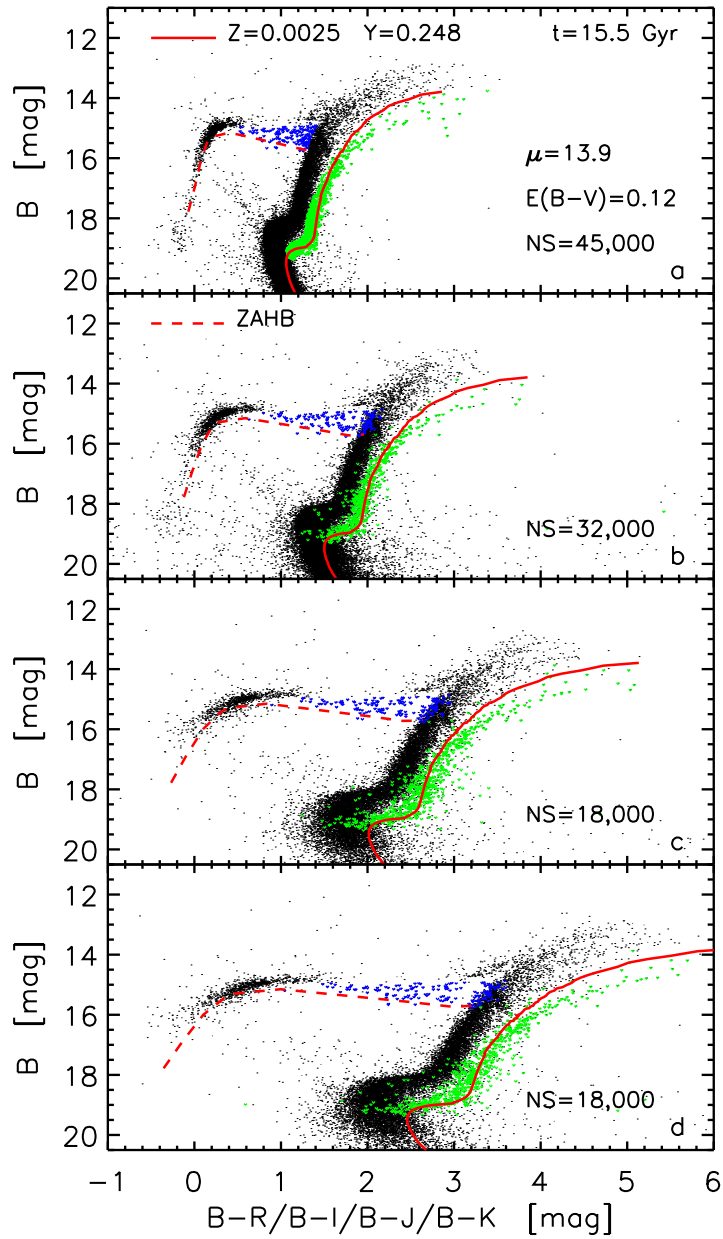


Figure 4.11: Same as in fig. 4.9, but compared to a 15.5 Gyr isochrone for the  $\omega 3$  population, constructed by adopting  $Z = 0.0025$ , and  $Y = 0.248$ . The fit was performed by adopting a true distance  $\mu = 13.9$ , and a reddening correction  $E(B - V) = 0.12$ . Note that the corresponding ZAHB matches the selected HB stars (blue objects).

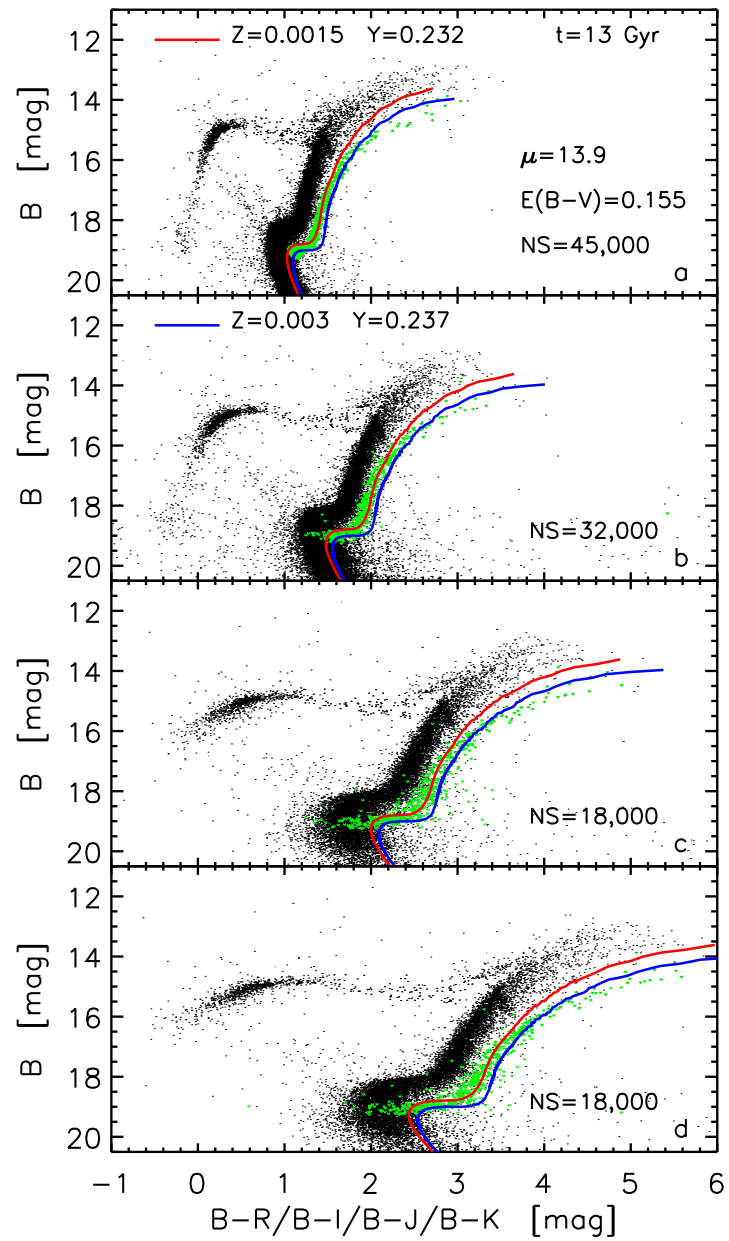


Figure 4.12: Same as fig. 4.11, but compared to 13-Gyr isochrones constructed by adopting different chemical compositions (see labels) and a higher reddening.

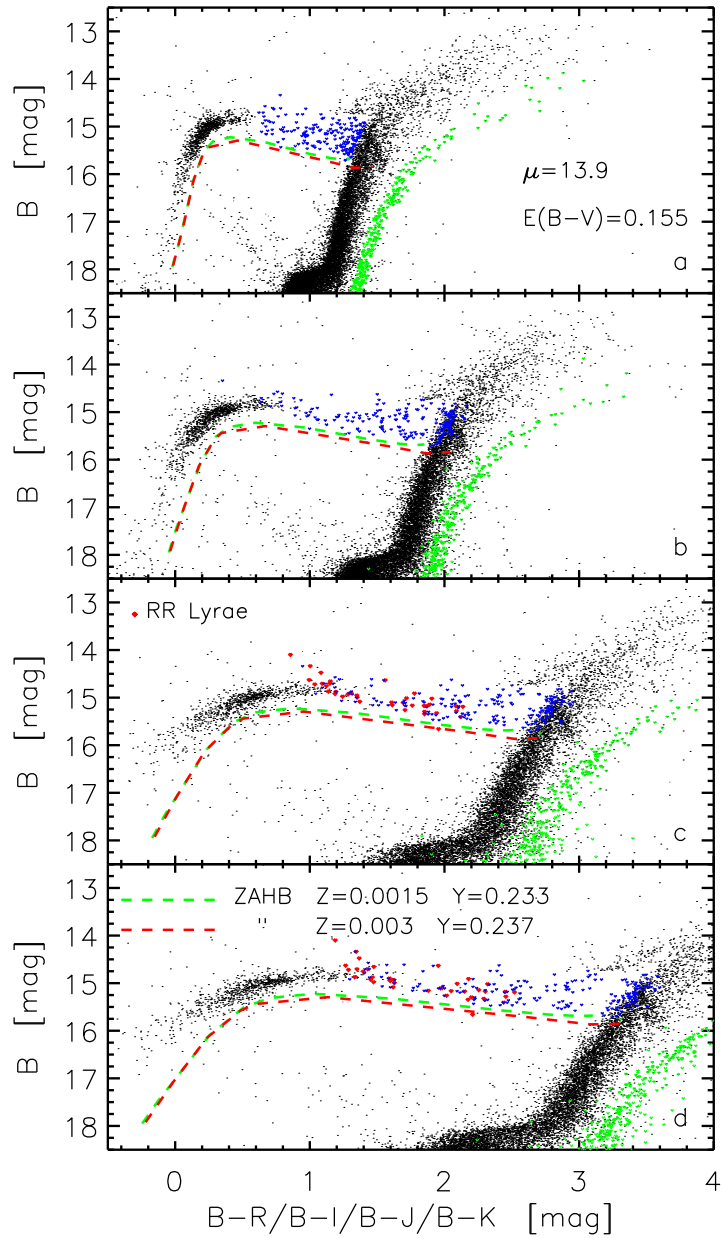


Figure 4.13: Same as in fig. 4.12, but the comparison between theory and observations is focused on Horizontal Branch stars. Blue objects mark stars located between hot HB stars and RGB stars, while red dots (panels **c,d**) in the HB region display RR Lyrae stars for which we have accurate mean NIR magnitudes.

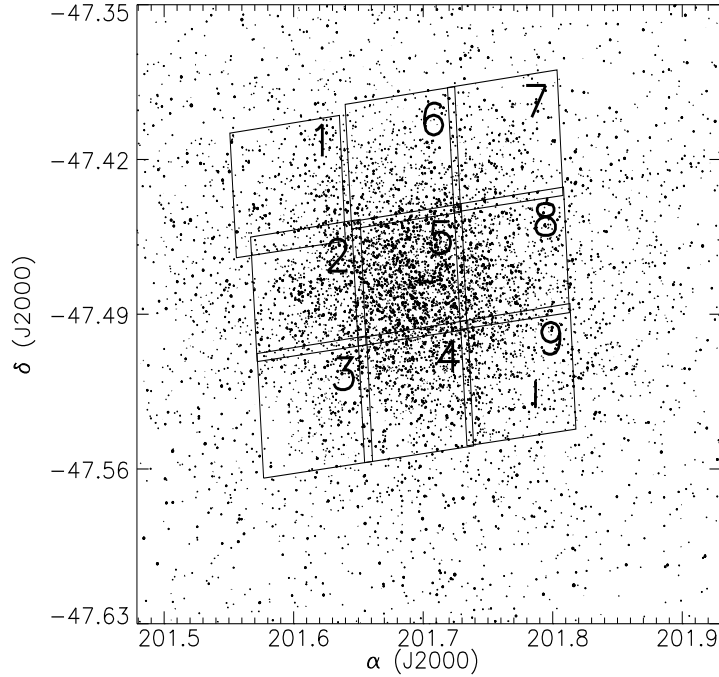


Figure 4.14: Position of the nine ACS pointings overplotted on a reference catalogue provided by Stetson (2000) (<http://cadwww.hia.nrc.ca/standards/>). Current photometry refers to pointings 2, 7 and 9.

in the Vega System (<http://www.stsci.edu/hst/acs/documents>).

In this investigation we present preliminary results based on three (pointings 2, 7, and 9) out the nine pointings (see fig. 4.14 for individual coordinates). Figure 4.15 shows the current sample of  $\omega$  Cen stars in the  $B - R, B$  plane. Interestingly enough, more than 2,212 blue objects populate the region ranging from  $B \approx 22, B - R \approx 0$ , down to  $B \approx 27, B - R \approx 0.8$ , thus covering the expected region of cluster WD cooling sequence.

Using GOODS data collected with ACS in the bands F435W and F606W, we estimated that the expected number of field galaxies with  $22 \leq B \leq 26$  and  $0.2 \leq B - R \leq 0.5$ <sup>2</sup> in the same area covered by current observations is  $\approx 60$  (Grazian et al. 2005, private communication). The number of field stars is also negligible, because halo and disk stars peak around  $B - R = 0.7$  and  $B - R = 1.8$ , respectively (King et al. 1990). More detailed estimates based on radial velocity (Suntzeff & Kraft 1996) or proper motion (van Leeuwen et al. 2000) measurements in  $\omega$  Cen suggest that at most two dozen of field stars might be located inside the area covered by current

<sup>2</sup>Note that to perform this estimate we accounted for the difference in magnitude between AB and Vega systems and for the difference between the filter F606W and the filter F625W (<http://www.stsci.edu/hst/acs/documents>).

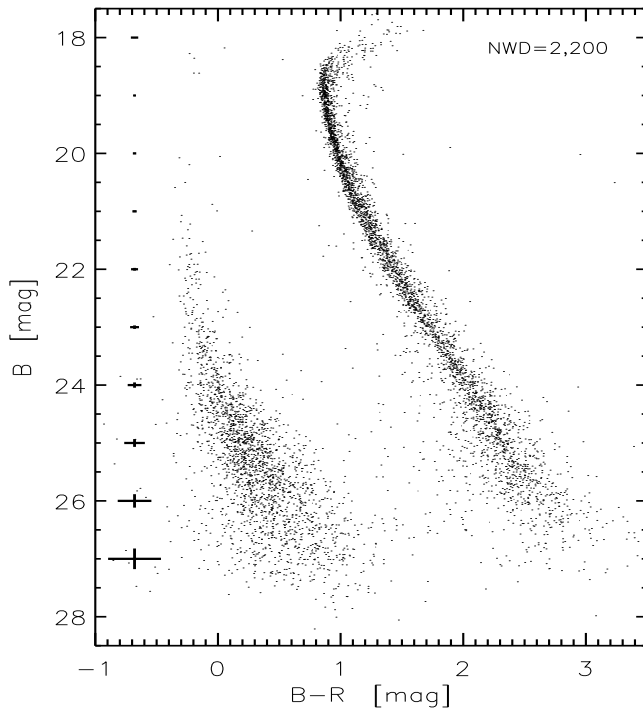


Figure 4.15: Color-Magnitude diagram in the  $B, B - R$  bands. The number of WD candidates are labeled. Error bars display intrinsic photometric errors.

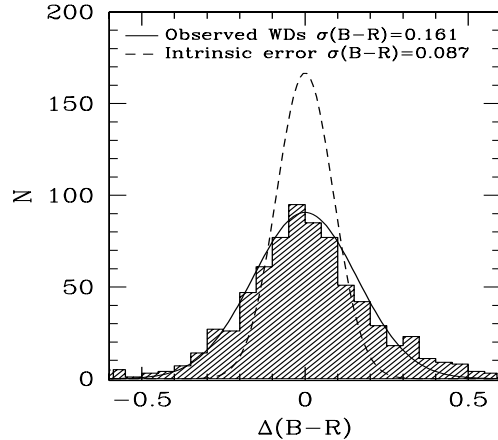


Figure 4.16: Color distribution of WDs in the magnitude interval  $B = 25 \pm 0.5$ . The solid line shows the gaussian fit to the observed distribution, while the dashed line the expected distribution for the same sample in case the WD colors would only be affected by gaussian photometric intrinsic errors.

data. Finally, theoretical Galactic models (Castellani et al. 2002) suggest that in the same area covered by current observations are present at most sixteen field WDs brighter than  $B = 25.5$  and fiftyfive field WDs brighter than  $B = 28$ .

This evidence suggests that we are facing with a bona fide sample of cluster WDS, including more than 2,000 objects, thus the largest sample of WDs ever observed in a stellar cluster. Data plotted in fig. 4.15 clearly show that, thanks to the sizable sample of  $\omega$  Cen stars, the cooling sequence show up at  $B \approx 21$ . This bright limit, if we assume for  $\omega$  Cen an apparent distance modulus  $DM_B \sim 14.21$  (Thompson et al. 2001), implies that current data are tracing the cooling history of cluster WDs at least below  $M_B \sim 7$ . According to predictions by Althaus, & Benvenuto (1998) for a  $0.5M_\odot$  WD with a CO core and pure H atmosphere models by Bergeron et al. (1995)<sup>3</sup> current WD sample provides the opportunity to investigate the WD cooling for luminosities ranging from ten times the solar luminosity down to  $\log L/L_\odot \sim -3.1$  ( $B \sim 27$ ,  $M_B \sim 12.8$ ).

By adopting the same theoretical predictions one can easily recognize that the huge number of WDs should not be a real surprise. As a matter of the fact, the number ratio between WD and HB stars, for not too long cooling times, is simply given by the ratio of the lifetimes spent during these two evolutionary phases. On the basis of the shallow ACS photometry in

<sup>3</sup>See also <http://www.ASTRO.UMontreal.CA/bergeron/CoolingModels/>

the  $B, R$  bands, recently presented by Freyhammer et al. (2005), we found in the same three fields the occurrence of  $\sim 630$  HB stars. The typical evolutionary lifetime for HB stars is  $\sim 1 - 4 \times 10^8$  year, depending on their ZAHB effective temperature (Castellani et al. 2004), while for a WD with a CO core and  $M = 0.5M_{\odot}$  at  $M_B \sim 11.3$  ( $\log L/L_{\odot} = -2.24$ ) the lifetime is  $\sim 3.5 \times 10^8$  years. This means that we expect to detect roughly twice as many WDs than HB stars brighter than  $B \approx 25.5$ . Interestingly enough, we detected approximately 1200 WDs brighter than this magnitude limit. However, current estimate should be considered as a robust lower limit, since we did not perform completeness experiment along the WD cooling sequence.

An unexpected observed feature in fig. 4.15, is the steady increase in color dispersion when moving toward fainter WD magnitudes. In order to assess whether this spread in color might be due to photometric errors, we performed an empirical test. We estimated the ridge line of WDs and the distance in color of individual objects from the ridge line. Figure 4.16 shows the color distribution of WDs in the magnitude interval  $B = 25 \pm 0.5$  together with its gaussian fit (solid line). Then we estimated standard deviation in color of the same selected WDs (intrinsic errors) and we found  $\sigma_{B-R} = 0.087$ . The dashed line plotted in fig. 4.16 shows the expected color distribution for the same sample of WDs (712) according to the assumption that their  $B, R$  magnitudes would only be affected by gaussian intrinsic errors. Data plotted in fig. 4.16 indicate that the sigma of the gaussian fit to observed WDs is a factor of two larger than expected. On this basis, we estimated that the two distributions differ at 99% confidence level. This finding, taken at face value, indicates that the color dispersion might be real.

#### 4.6.1 Discussion

In order to investigate the WD location in the CM diagram we adopted the WD cooling sequences for CO core and H envelopes constructed by Althaus, & Benvenuto (1998). Theoretical predictions have been transformed into the observational plane by adopting pure H atmosphere models constructed by Bergeron et al. (1995). Predicted cooling sequences for  $M = 0.5, 0.7, 0.9M_{\odot}$  have been plotted by adopting canonical estimates for cluster reddening ( $E(B - V) = 0.11 \pm 0.02$ , Lub 2002) and distance modulus ( $\mu = 13.7 \pm 0.11$ , Thompson et al. 2001). The reddening in the  $B, R, H_{\alpha}$  bands was estimated using the extinction model of Cardelli et al. (1989).

The comparison between theory and observations (see panel a) of fig. 4.17) discloses a good agreement for the bright portion ( $22 \leq B \leq 23$ ). However, the theoretical sequences toward fainter magnitudes appear to fit the blue (hot) edge of the observed WDs. It is noteworthy, that a WD with a stellar mass  $M = 0.5M_{\odot}$  is a lower limit for WDs with CO-core, actual WDs are expected to be slightly more massive ( $\sim 0.53M_{\odot}$ , Renzini

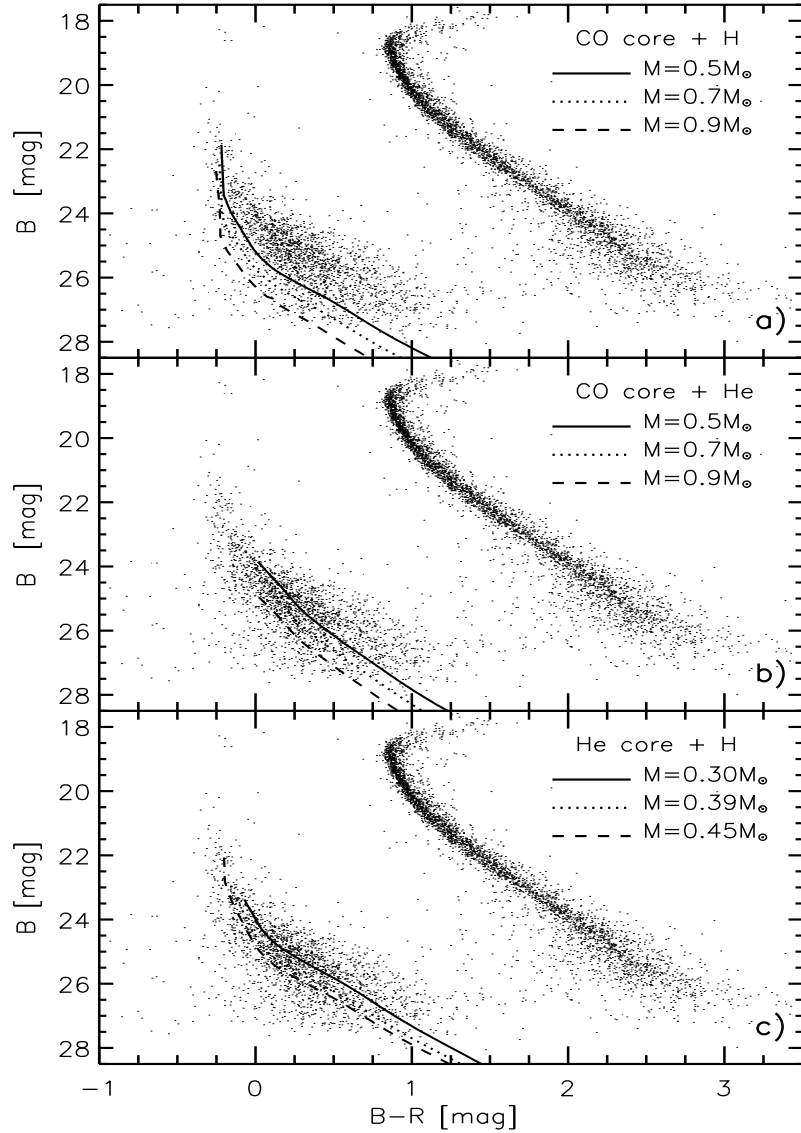


Figure 4.17: Color-Magnitude diagram in the  $B, B-R$  bands. Panel **a)** - Solid, dotted, and dashed lines show predicted WD cooling sequences for CO core and H envelopes with stellar masses equal to 0.5, 0.7, and 0.9  $M/M_{\odot}$  (Althaus, & Benvenuto (1998)). Theoretical predictions have been transformed into the observational plane by adopting H atmosphere models. Panel **b)** - Same as panel **a)**, but for WD cooling sequences, with CO core and He envelopes (Benvenuto, & Althaus (1997), transformed into the observational plane by adopting He atmosphere models. Panel **c)** - Same as panel **a)**, but for WD cooling sequences with He core and H envelopes (Serenelli et al. (2002)), stellar masses equal to 0.30, 0.39, and 0.45  $M/M_{\odot}$  and H atmospheres.

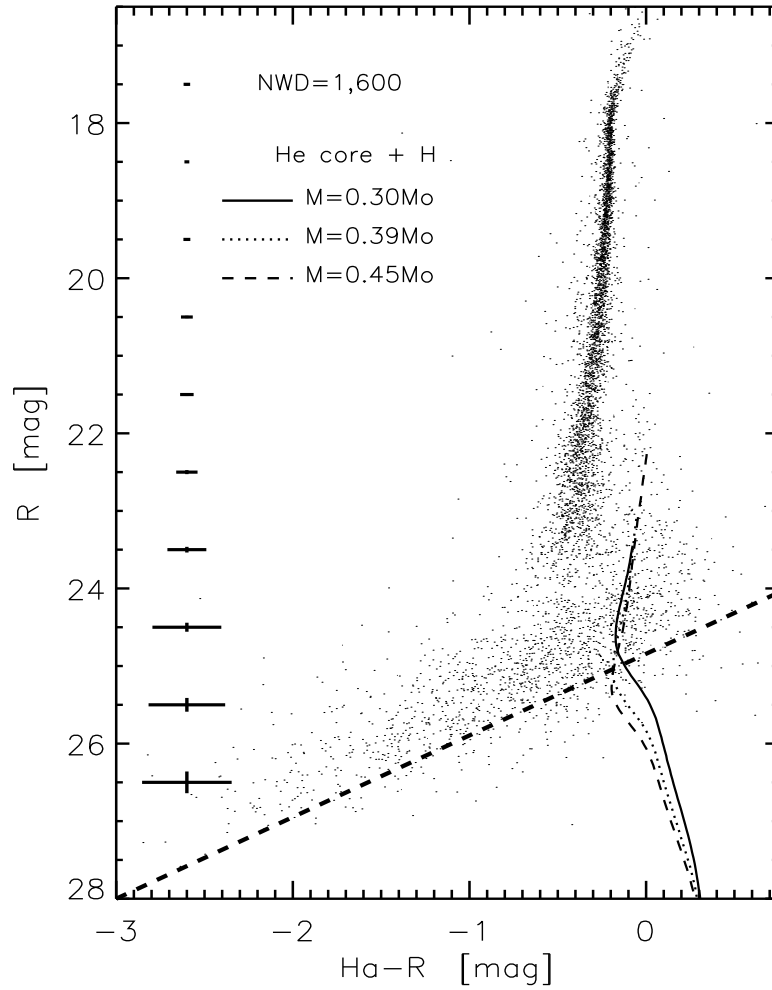


Figure 4.18: Color-Magnitude diagram in the  $R, H_\alpha - R$  bands. Predicted cooling sequences are the same as in panel c) of fig. 4.17. The thick dashed line marks the detection limit. Error bars display intrinsic photometric errors.

et al. 1996). Current uncertainties on reddening (0.02 across the body of the cluster (Schlegel et al. 1998), and on cluster distance cannot account for the observed systematic drift in color. This evidence suggests that the observed WD cooling sequence is cooler (redder) than expected.

In principle one can find several plausible reasons for such an occurrence. In particular, we note that for  $22 \leq B$  we are already below the so-called "DB gap" (Hansen & Liebert 2003), i.e. WDs with He atmospheres could be present. Data plotted in panel b) of fig. 4.17, show that by adopting WD cooling sequences for CO core, and He envelopes by Benvenuto, & Althaus (1997) together with He atmosphere models by Bergeron et al. (1995) the cooling sequence is indeed moving toward redder colors. Note that the cut-off of the cooling sequences in the bright region is due to the fact that He atmosphere models do not cover this temperature region. The comparison between theory and observations indicates that the bulk of the observed WDs might be of the DB type.

As shown in the lower panel of fig. 4.17, a different possibility is given by the occurrence of He-core WDs. Interestingly enough, predicted WD cooling sequences for He core structures by Serenelli et al. (2002), transformed into the observational plane by adopting H atmosphere models, also account for the observed distribution. Current findings are marginally affected by the adopted theoretical predictions, and indeed different sets of WD cooling sequences (Fontaine et al. 2004; Prada & Straniero 2002), transformed into the  $B - R, B$  plane by adopting the same atmosphere models, agree quite well with each other.

Finally, it is worth noting that current  $H_\alpha - R, R$  data (see fig. 4.18), show that a good fraction of detected WDs ( $\sim 1,600$ ) are  $H_\alpha$  bright, and indeed they attain  $H_\alpha - R$  colors systematically bluer than predicted. This evidence is suggestive of WDs with a Hydrogen atmosphere and/or with stellar activity. We would like to mention that blending and/or binarity could also affect observed colors. Therefore, no firm conclusion can be reached on the basis of current data. More detailed photometric and spectroscopic investigations of this large sample of cluster WDs will certainly provide fundamental hints concerning the evolution of cooling WD structures and their origin.

# Chapter 5

## Conclusions

### 5.1 Stellar populations in the Carina dSph galaxy

We have presented wide field optical photometry of the Carina dSph galaxy. The main results obtained can be summarized as follows:

- At least three distinct star formation events have been identified. The bulk of the Carina stellar content is made by intermediate-age stars (3-7Gyr), but hosts old stars (>10 Gy) as well. We discovered the presence of a young MS formed less than 1Gyr ago. The occurrence of this young population is supported by the detection of 13 Anomalous Cepheids.
- The radial distributions of Carina stellar populations are different. Intermediate-age stars appear more centrally concentrated, while the old component is distributed in a sort of broad halo. Moreover, the projected distribution of old stars along both mayor and minor axis is not symmetric.
- Preliminary results based on low-resolution spectra of  $\approx 40$  Carina stars suggest the existence of two peaks in the radial velocity distribution. Due to the small sample it is not possible to correlate the the kinematical and the evolutionary properties of our target.
- We performed a statistical subtraction of field stars. We could study in detail the morphology of the Red Clump, which appears to be populated by stars with masses up to  $2M_{\odot}$ . We detected an overdensity of objects at  $B - V \approx 0.75$  and  $B - V \approx 0.90$  consistent with theoretical predictions for the AGB of the old population.

There is evidence that the subgiant branch of the intermediate-age population has a discrete structure, supporting the hypothesis of an halt during the intermediate-age burst.

- We investigated the outer regions of Carina to detect extra-tidal stars. We observed six fields, located across or well beyond the tidal radius. A blue spur of faint objects has been detected in all regions. To investigate the nature of these object, we collected deep multiwavelength photometry in the  $U, B, V, I$  bands. We used the color-color plane ( $U-V$ ) vs ( $B-I$ ) as a diagnostic to split Carina stars from background galaxies.

### 5.1.1 Future perspectives

- We collected radial velocity measurments for  $\approx 330$  stars. Five fields were observed, both in the very centre of the galaxy as well as outside the core radius. Our targets sample the stellar populations of Carina down to  $V \approx 23$ . This allow us to investigate any peculiarity in the kinematical properties, supporting or not the photometric evidence that intermediate-age stars are more centrally concentrated than old stars. Moreover, it will be possible to investigate whether the occurrence of a double peak in the radial velocity distribution is correlated with different populations.
- We will estimate the chemical composition of our targets. This will allow us to constrain on a quantitaive basis the spread in the metal abundancies between old and intermediate-age stars, if any.
- We could not confirm nor discard the detection of extra-tidal stars in Carina. More data are mandatory to understand the nature of the blue faint objects present in the CMDs. However, the detection of extra-tidal stars would arise new questions about the real extent of this stellar system. Extra-tidal stars could be the fingerprint of tidal interaction with the Galaxy, but we could also support the theoretical prediction of the existence of a huge halo surrounding dSphs.
- We are developing new algorithms for the detection of variable stars. We observed the central regions of Carina in many runs in the last five years. Moreover, we collected archive data for a total baseline of roughly ten years. This means that we can search for variable stars from the Tip of the RGB (long period variables) down to the MSTO (Dwarf Cepheids, oscillating Blue Stragglers)

## 5.2 Stellar populations in $\omega$ Cen

We have presented a new set of multi-band photometric data for the GGC  $\omega$  Cen and—in agreement with previous findings in the literature—we find no acceptable fit to the different stellar populations for a single distance, reddening, and age. We found two reasonable fits for the  $\omega 3$  stars: (1) by

adopting a 0.2 higher distance modulus ( $\approx 500$  pc), a metal-intermediate composition ( $Z = 0.0025$ ,  $\text{Fe}/\text{H} \approx -0.9$ ), and an unreasonable increase in age of  $\sim 4$  Gyr; or (2) for the same  $\Delta\mu = 0.2$  shift, an increase in the reddening, metal-intermediate chemical compositions ( $0.0015 \leq Z \leq 0.003$ ,  $-1.1 \leq \text{Fe}/\text{H} \leq -0.8$ ), and an age that, within current uncertainties, is coeval with the bulk of the  $\omega$  Cen stars. Current findings indicate that  $\omega$  3 stars are not significantly more metal-rich than  $Z = 0.003$ . This evidence is supported by the shape of the  $\omega$  3 SGB, as already suggested by Ferraro et al. (2004) and by the fit of HB stars. We are in favour of the latter solution for the following reasons:

- The difference in distance between the  $\omega$  3 branch and the bulk of  $\omega$  Cen stars is of the order of 10%. This estimate is 3–4 times smaller than the estimate by Bedin et al. (2004) and in very good agreement with the distance of the density maxima detected by Odenkirchen et al. (2003) along the tidal tails of the GGC Pal 5. Moreover, recent N-body simulations (Capuzzo Dolcetta et al. 2004) indicate that clumps along the tidal tails can approximately include 10% of the cluster mass.

- We found that by artificially shifting the  $\omega$  3-branch stars to account for the assumed difference in distance and reddening, they overlap with the  $\omega$  2 population. It has been recently suggested by Piotto et al. (2005), on the basis of low-resolution spectra, that the bluer main sequence detected by Bedin et al. (2004) is more metal-rich than the red main sequence. Unfortunately, current ACS photometry is only based on shallow exposures, and therefore we cannot properly identify in our data these stellar populations located in the lower main sequence. The same outcome applies to the suspected extremely-hot HB progeny of the bluer main sequence, since they have not been detected in the NIR bands.

- Current preliminary findings support recent N-body simulations by Chiba & Mizutani (2004) and by Ideta & Makino (2004). In particular, the latter authors found, by assuming that the progenitor of Omega Centauri is a dwarf galaxy, that more than 90% of its stellar content was lost during the first few pericenter passages (see their fig. 2).

- $\omega$  Cen reddening estimates in the literature cluster around  $E(B - V) = 0.12 \pm 0.02$ . However, the map from (Schlegel et al. 1998) indicates reddening variations of 0.02 across the body of the cluster while, more importantly, 2MASS data (Law et al. 2003) show a very clumpy reddening distribution at distances beyond  $1^\circ$  (100 pc) from the cluster centre, with large variations  $\Delta E(B - V) = 0.18$  across a 4 degrees<sup>2</sup> area. However, the inference of reddening *between* the main body of  $\omega$  Cen and the supposed background population is very surprising.  $\omega$  Cen lies at the comparatively low galactic latitude of  $+15^\circ$ , and the reddening variations seen in the Schlegel and 2MASS maps likely originate in the foreground interstellar material of the Galactic disk. Any interstellar material behind  $\omega$  Cen must lie at least 1.4 kpc from the Galactic plane, and therefore would most likely be asso-

ciated with  $\omega$  Cen itself. Smith et al. (1990) have reported a significant detection of  $HI$  in the direction of  $\omega$  Cen, blueshifted by  $\sim 40 \text{ km s}^{-1}$  with respect to the cluster velocity. However, their interpretation is that this gas is associated with the northern extension of the Magellanic Stream far beyond the cluster. It would be a remarkable coincidence if this interstellar material happened to lie between the cluster and a clump in the tidal tail at a 10% greater distance than the main cluster body, while traveling at the quoted relative speed. However, it is worth noting that Smith et al. (1990) estimated for this cloud a column density of  $N_H \approx 3 \times 10^{18} \text{ atoms/cm}^2$ , and therefore a reddening  $E(B - V) \approx 0.07$  (Predehl & Schmitt 1995) that is at least a factor of two larger than required by our best fit. This point is crucial for the proposed explanation and needs to be further investigated.

Finally, we note that the comparison between predicted ZAHBs and HB stars indicates that the occurrence of an old stellar population with  $Z > 0.002$  would imply the occurrence of an anomalous clump along the RGB. In fact, more metal-rich, red HB stars cover the same color range of metal-poor RGB stars. The detection of such a feature along the RGB can supply robust constraints on the progeny of the  $\omega 3$  stellar population. These results, when independently confirmed, would suggest that the  $\omega 3$  branch might be a clump of stars located 500 pc beyond the bulk of the cluster. No firm conclusion can be drawn on the basis of current data, although this evidence together with the increase in radial velocity among  $\omega 3$  stars measured by Sollima et al. (2004) and numerical simulations recently provided by Capuzzo Dolcetta et al. (2004) indicates that it could be a tidal tail.

We have presented preliminary results concerning the detection of more than 2,000 WDs. This is the biggest sample of WDs ever detected in any GC. Such a large sample appears in good agreement with predictions based on the ratio between WD and HB evolutionary lifetimes. No firm conclusions can be derived on the origin of these stars. The comparison with theoretical cooling sequences suggests that the bulk of WDs may be of the DB type. However, predicted sequences for He core WDs nicely fits the observed distribution. This suggests that part of the detected WDs might be the evolutionary aftermath of binary systems. Interestingly enough, a sizable fraction of the detected WDs appears to be  $H_\alpha$  bright.

### 5.2.1 Future perspectives

- Spectroscopic observations of the brightest WDs will be performed in the next months with the FLAMES multi-object spectrograph. This will allow us to shed new light on the nature of these objects.
- Deep IR data will be acquired with ISAAC@VLT. New deep optical-IR CMDs will allow us to disentangle the age-metallicity degeneracy. In

fact, the  $U$ ,  $(U-J)$  and  $U$ ,  $(U-K)$  planes are very sensitive to metallicity and age, but only marginally affected by reddening uncertainties.



# Appendix A

## Publications

### Refereed Publications:

- Dall’Ora, M; Ripepi, V; Caputo F.; Castellani, V.; Bono, G; Brocato, E.; Buonanno, R.; Castellani, M; Corsi, C.E.; Marconi, M; Pulone, L.; Walker, A.R.; Smith, H.A., 2003, **The carina project I: bright variable stars**, 2003, AJ, 126, 197
- Monelli, M.; Pulone, L.; Corsi, C.E.; Castellani, M.; Bono, G.; Walker, A.R.; Brocato, E.; Buonanno, R.; Caputo, F.; Castellani, V.; Dall’Ora, M.; Marconi, M.; Monelli M.; Nonino, M.; Ripepi, V.; Smith, H.A., 2003, **The carina project II: stellar populations**, 2003, AJ, 126, 218
- Dall’Ora, M.; Storm, J.; Bono, G.; Ripepi, V.; Monelli, M.; Testa, V.; Andreuzzi, G.; Buonanno, R.; Caputo, F.; Castellani, V.; Corsi, C. E.; Marconi, G.; Marconi, M.; Pulone, L.; Stetson, P. B. **The Distance to the Large Magellanic Cloud Cluster Reticulum from the K-Band Period-Luminosity-Metallicity Relation of RR Lyrae Stars** , 2004, ApJ, 610, 269
- Monelli, M.; Corsi, C. E.; Castellani, V.; Ferraro, I.; Iannicola, G.; Prada Moroni, P. G.; Bono, G.; Buonanno, R.; Calamida, A.; Freyhammer, L. M.; Pulone, L.; Stetson, P. B. **The Discovery of more than 2000 white dwarfs in the Globular Cluster Omega Centauri**, 2005, ApJ, 621L, 117

### Proceedings with Referee:

- Ripepi, V.; Monelli, M.; dall’Ora, M.; Bono, G.; Corsi, C.; Caputo, F.; Pulone, L.; Testa, V.; Andreuzzi, G.; Buonanno, R.; Marconi, G.; Marconi, M.; di Criscienzo, M.; Storm, J.; degl’Innocenti, S. **UBVI Time-series Photometry of the Old LMC Globular Cluster Reticulum**, 2004, CoAst, 145, 24

## Non Refereed Publications:

- Ripepi, V., dall’Ora, M., Pulone, L., Castellani, M., Corsi, C., Monelli, M., Bono, G., Brocato, E., Caputo, F., Castellani, V., Marconi, M., Nonino, M., Smith, H., Walker, A. R. **The Carina Dwarf Galaxy Variable Star Population**, in Radial and Nonradial Pulsations as Probes of Stellar Physics , ASP Conference Proceedings, 2002, Vol. 259, p.134
- Monelli M., Andreuzzi G., Bono G., Buonanno R., Caputo F., Castellani M., Castellani V., Corsi C.E., Dall’Ora M., Marconi G., Pulone L., Ripepi V., Storm J., Testa V. **Multiwavelength Time Series Data of the LMC Cluster Reticulum**, in “New Horizons in Globular Cluster Astronomy”, ASP Conference Series, 2003, 296, 388, Eds.: G. Piotto, G. Meylan, G. Djorgowski and M. Riello
- Castellani M., Bono G., Buonanno R., Caputo F., Castellani V., Corsi C.E., Dall’Ora M., Marconi M, Monelli M., Nonino M., Pulone L., Ripepi V., Smith H.A., Walker A.R., **The Carina Project: color magnitude diagram and radial distribution** in Workshop on Variability with Wide Field Imagers , Memorie della Societa Astronomica Italiana, 2003, 74, 874
- Corsi, C. E., Bono, G., Walker, A. R., Brocato, E., Buonanno, R., Caputo, F., Castellani, M., Castellani, V., Dall’Ora, M., Marconi, M., Monelli, M., Nonino, M., Pulone, L., Ripepi, V., Smith, H. A., **The Carina Project: Absolute and Relative Calibrations** in Workshop on Variability with Wide Field Imagers , Memorie della Societa Astronomica Italiana, 2003, 74, 874
- Dall’Ora, M.; Ripepi, V.; Caputo, F.; Castellani, V.; Bono, G.; Brocato, E.; Buonanno, R.; Castellani, M.; Corsi, C. E.; Marconi, M.; Monelli, M.; Nonino, M.; Pulone, L.; Smith, H. A.; Walker, A. R. **The Carina project: bright variables** in Workshop on Variability with Wide Field Imagers , Memorie della Societa Astronomica Italiana, 2003, 74, 894
- Monelli, M.; Walker, A. R.; Bono, G.; Brocato, E.; Buonanno, R.; Caputo, F.; Castellani, M.; Castellani, V.; Corsi, C. E.; Dall’Ora, M.; Marconi, M.; Pulone, L.; Ripepi, V.; Nonino, M.; Smith, H. A.; Stetson, P. B.; Zoccali, M. **The Carina Project: Photometric Accuracy**, in Workshop on Variability with Wide Field Imagers , Memorie della Societa Astronomica Italiana, 2003, 74, 909
- Dall’Ora, M.; Bono, G.; Storm, J.; Testa, V.; Andreuzzi, G.; Buonanno, R.; Caputo, F.; Castellani, V.; Corsi, C. E.; Degl’Innocenti, S.;

- Marconi, G.; Marconi, M.; Monelli, M.; Ripepi, V. **Near-Infrared photometry of LMC cluster Reticulum** in Stars in Galaxies , Memorie della Societa Astronomica Italiana, 2004, 75, 138
- Monelli, M.; Walker, A. W.; Bono, G.; Buonanno, R.; Caputo, F.; Castellani, M.; Corsi, V. Castellani C. E.; Dall’Ora, M.; Marconi, M.; Pulone, L.; Ripepi, V.; Nonino, M.; Brocato, E.; Smith, H. A. **Wide Field Optical Photometry of the Carina Dwarf Spheroidal Galaxy**, in Stars in Galaxies , Memorie della Societa Astronomica Italiana, 2004, 75, 114
  - Monelli, M.; Walker, A. R.; Bono, G.; Buonanno, R.; Caputo, F.; Castellani, M.; Castellani, V.; Corsi, C. E.; dall’Ora, M.; Pulone, L.; Marconi, M.; Ripepi, V.; Nonino, M.; Smith, H. A.; Stetson, P. B. **Short and long period variable stars in the Carina dwarf Spheroidal galaxy** in Variable Stars in the Local Group , IAU Colloquium 193, ASP Conference Proceedings, 2004, Vol. 310, 133
  - Dall’Ora, M.; Bono, G.; Storm, J.; Ripepi, V.; Testa, V.; Andreuzzi, G.; Buonanno, R.; Caputo, F.; Castellani, V.; Corsi, C. E.; degl’Innocenti, S.; Marconi, G.; Marconi, M.; Monelli, M. **Near-Infrared photometry of the LMC cluster Reticulum** in Variable Stars in the Local Group , IAU Colloquium 193, ASP Conference Proceedings, 2004, Vol. 310, 189
  - Ripepi, V.; Monelli, M.; Dall’Ora, M.; Bono, G.; Corsi, C.E.; Caputo, F.; Pulone, L.; Testa, V.; Andreuzzi, G.; Buonanno, R.; Marconi, G.; Marconi, M.; di Criscienzo, M.; Storm, J.; Degl’Innocenti, S. **UBVI Time-series Photometry of the Old LMC Globular Cluster Reticulum** , 2004, CoAst, 145, 24
  - Nevils, G. K.; Koger, D. K.; James, C. R.; Monelli, M., **Seeking chemical and kinematic correlations within the Carina Dwarf Spheroidal**, 2004, AAS, 205, 9302

## Accepted Publications:

- Freyhammer L.M.; Monelli M.; Bono G. ; Cunti P.; Ferraro I.; Calamida A.; Degl’Innocenti S.; Prada Moroni P.G.; Del Principe M.; Piersimoni A.; Iannicola G.; Stetson P.B.; Andersen M.I.; Buonanno R.; Corsi C.E.; Dall’Ora M.; Petersen J.O.; Pulone L.; Sterken C; Storm J. **On the anomalous Red Giant Branch of the globular cluster  $\omega$  Cen**, Accepted for publication on ApJ, astro-ph/0502585



# Bibliography

- Adorf, H.M., 1995, *ST-ECF Newsletter*, 23, 19
- Alcaino, G & Liller, W., 1987, *AJ*, 94, 1585
- Althaus, L. G., & Benvenuto O. G. 1998, *MNRAS*, 296, 206
- Andersen, M.I., Freyhammer, L., & Storm, J. 1995, *Calibrating and Understanding HST and ESO Instruments*, 87
- Bedin et al., 2000, *A&A*, 363, 159
- Bedin, L.R., Piotto, G., Anderson, J., Cassisi, S. et al. 2004, *ApJ*, 605, 125
- Bennett, C.L., Halpern, M., Hinshaw, G., Jarosik, N. et al. 2003, *ApJS*, 148, 1
- Benvenuto, O. G., & Althaus L. G. 1997, *MNRAS*, 288, 1004
- Bergeron, P., Wesemael, F., & Beauchamp, A. 1995, *PASP*, 107, 1047
- Bonifacio, P., Hill, V., Molaro, P., Pasquini, L., Di Marcantonio, P., & Santin, P. 2000, *A&A*, 359, 663
- Bono, G., Caputo, F., Santolamazza, P., Cassisi, S., Piersimoni, A. 1997, *AJ*, 113, 2209
- Bono, G., Groenewegen, M. A. T., Marconi, M., & Caputo, F. 2002, *ApJ*, 574, L33
- Brocato, E., Castellani, V., Ferraro F. R., Piersimoni, A. N., & Testa, V. 1996, *MNRAS*, 282, 614
- Butler, D.; Dickens, R. J.; & Epps, E., 1978, *ApJ*, 225, 148
- Burstein, D., & Heiles, C. 1982, *AJ*, 87, 1165
- Cannon, R.D., Hawarden, T.G. & Tritton, S.B. 1977, *MNRAS*, 180, 81
- Cannon, R.D., Niss, B. & Nørgaard-Nielsen, H.U. 1981, *MNRAS*, 196, 1

- Cannon, R. D.; & Stobie, R. S., 1973, MNRAS, 162, 207
- Cannon, R. D.; & Stewart, N. J., 1981, MNRAS, 195, 15
- Caputo, F., Castellani, V., & Degl'Innocenti, S. 1995, A&A, 304, 365
- Caputo, F., Castellani, V., Marconi, M., & Ripepi, V. 2000, MNRAS, 316, 819
- Capuzzo Dolcetta, R., Di Matteo, P., & Mocchi, P. 2004, AJ, accepted, astro-ph/0406313
- Cardelli, J.A., Clayton, G.C., Mathis, J.S. 1989, ApJ, 345, 245
- Carignan, C., Beaulieu, S., Ct, S., Demers, S., & Mateo, M., 1998, AJ, 116, 1690
- Cariulo, P., Degl'Innocenti S., Castellani, V., 2004, A&A 421, 1121
- Carrera, R., Aparicio, A., Martinez-Delgado, D., & Alonso-Garcia, J. 2002, AJ, 123, 3199
- Cassisi, S., Schlattl, H., Salaris, M., Weiss, A., 2003, ApJL, 582, 43
- Cassisi, S., Castellani, V., Degl'Innocenti, S. & Weiss, A. 1998, A&AS, 129, 267
- Cassisi, S., Castellani, V., Degl'Innocenti, S., Salaris, M., & Weiss, A. 1999, A&AS, 134, 103
- Castellani, M., Marconi, G., & Buonanno, R. 1996, A&A, 310, 715
- Castellani, V., Cignoni, M., Degl'Innocenti, S., Petroni, S., & Prada Moroni, P. G., 2002, MNRAS, 334, 69
- Castellani, V., & Degl'Innocenti, S. 1999, A&A, 344, 97
- Castellani, V., Degl'Innocenti, S., Marconi, M., Prada Moroni, P.G. & Sestito, P. 2003, A&A, 404, 645
- Castellani, V., Zoccali, M., Bono, G., Iannicola, G., Cassisi, S., Buonanno, R. 2004, A&A, accepted
- Castelli, F. 1999, A&A, 346, 564
- Castelli, F., Gratton, R. G., & Kurucz, R. L. 1997, A&A, 318, 841
- Castelli, F., Gratton, R. G., & Kurucz, R. L. 1997, A&A, 324, 432
- Cen, R. 2001, ApJ, 549, 195

- Chiba, M., & Mizutani, A. 2004, *PASA*, 21, 237
- Cole, A. A., Smecker-Hane, T. A., & Gallagher, J. S., III. 2000, *AJ*, 120, 1808
- Corwin, T., Carney, B. W., & Nifong, B. G. 1999, *AJ*, 118, 2875
- Da Costa, G. S. 1991, in *IAU Symp. 148, The Magellanic Clouds*, ed. R. Haynes & D. Milne (Dordrecht: Kluwer), 183
- Dall’Ora, M., Ripepi, V., Caputo, F., Castellani, V., Bono, G., Smith, H. A., Brocato, E., Buonanno, R., Castellani, M., Corsi, C. E., Marconi, M., Monelli, M., Nonino, M., Pulone, L., Walker, A. R., 2003, *AJ*, 126, 197
- Dickens, R.J., & Wooley, R.v.d.R., 1967, *R.Obs.Bull*, 128, 255
- Dinescu, D.I.; van Altena, W.F.; Girard, T.M.; Lpez, C.E., 1999, *AJ* ,117, 277
- Djorgowski, G, 1993, *ASP Conf. Ser. 50: Structure and Dynamics of Globular Cluster*, 50
- Dolphin, A. E. 2002, *MNRAS*, 332, 91
- Elson, R. A. W., Gilmore, G. F., Santiago, B. X., Casertano, S.,1995, *AJ*, 110, 682
- Ferraro, F.R.; Sollima, A.; Pancino, E.; Bellazzini, M.; Straniero, O.; Origlia, L.; Cool, A.M.
- Ferraro, F. R., Clementini, G., Fusi Pecci, F., Sortino, R., & Buonanno, R. 1992, *MNRAS*, 256, 391
- Ferraro, F.R., Sollima, A., Pancino, E., Bellazzini, M., et al. 2004, *ApJ*, 603, 81
- Fioc, M. & Rocca-Volmerange, B., 1997, *A&A*, 326, 950
- Fontaine, G., Brassard, P., & Bergeron, P. 2001, *PASP*, 113, 409
- Freyhammer, L. et al., 2001, *ExA*, 12, 147
- Freyhammer, L., Monelli, M., Bono, G., et al. 2005, *ApJ*, accepted
- Frinchaboy, P.M.; Majewski, S.R.; Crane, J.D.; Reid, I.N.; Rocha-Pinto, H.J.; Phelps, R.L.; Patterson, R.J.; Muoz, R.R., 2004, *ApJL*, 602, 21
- Fusi Pecci, F., Ferraro, F. R., Corsi, C. E., Cacciari, C., & Buonanno, R. 1992, *AJ*, 104, 1831
- Geyer, E.H., Nelles, B. & Hopp, U., 1983, *A&A*, 125, 359

- Girardi, L., & Salaris, M. 2001, MNRAS, 323, 109
- Godwin, P.J., 1985, in "Dynamics of star cluster", IAUS, 113, 77
- Gratton, R.G., Bragaglia, A., Carretta, E., Clementini, G., Desidera, S., Grundahl, F., Lucatello, S. 2003, A&A, 408, 529
- Grillmair, Carl J.; Freeman, K. C.; Irwin, M.; Quinn, P. J., 1995, AJ, 109, 2553
- Hansen, B. M. S., & Liebert, J. 2003, ARA&A, 41, 465
- Harbeck, D., et al. 2001, AJ, 122, 3092
- Harris, W.,E., 1996, AJ, 112, 1487
- Hartwick, F. 1968, ApJ, 154, 475
- Hayashi, E. et al., 2003, ApJ, 584, 541
- Hernandez, X., Gilmore, G., & Valls-Gabaud, D. 2000, MNRAS, 317, 831
- Hilker, M. & Richtler, T., 2000, A&A, 362, 895
- Hurley-Keller, D., Mateo, M., & Nemeč, J. 1998, AJ, 115, 1840
- Hodge, P. W. 1989, ARA&A, 27, 139
- Hughes, J. & Wallerstein, G., 2000, AJ, 119,, 1225
- Ideta, M., & Makino, J. 2004, ApJ, 616, L107
- Ikuta, C., & Arimoto, N., 2002, A&A, 391, 55
- Irwin M. & Hatzidimitriou D., 1995, MNRAS, 277, 1354
- Kaluzny, J., Olech, A., Thompson, I.B., Pych, W., Krzeminski, W., Schwarzenberg-Czerny, A. 2004, A&A, 424, 1101
- Kazantzidis, S, Mayer, L, Mastropietro, C, Diemand, J, Stadel, J, Moore, B, 2004, ApJ, 608, 663
- King, I., Gilmore, G., & van der Kruit, P. C. 1990, The Milky Way As Galaxy, University Science Books
- King, I. R.; Anderson, J., 2002, in ASP Conf. Ser. 265, Omega Centauri: A Unique Window into Astrophysics, ed. F. van Leeuwen, J. Hughes and G. Piotto (S. Francisco: ASP), 87
- Kleyna et al., 2001, ApJ, 563, 115
- Krauss, L. M. & Chaboyer, B. 2003, Sci, 299, 65

- Kravtsov, V., Ipatov, A., Samus, N., Smirnov, O., Alcaïno, G., Liller, W., & Alvarado, F. 1997, *A&AS*, 125, 1
- Koch, A., Grebel, E.K., Harbeck, D., Wilkinson, M.I., Kleyna, J.T., Gilmore, G.F., Wyse, R.F.G., Evans, N.W., astro/ph0410435
- Koch, A., Grebel, E. K., Odenkirchen, M., Caldwell, J. A. R., 2004, *Msngr*, 115, 37
- Kuhn, J.R., Smith, H.A. & Hawley, S.L. 1996, *ApJ*, 469, L93
- Landolt, A.U., 1983, *AJ*, 88, 853
- Landolt, A.U., 1992, *AJ*, 104, 340
- Lavery, R. J., Seitzer, P., Walker, A. R., Suntzeff, N. B., & Da Costa, G. S. 1996, in *The Impact of Stellar Physics on Galaxy Evolution*, ed. C. Leitherer, U. Fritze-von-Alvensleben, & J. Huchra, (San Francisco: ASP), 333
- Law, D.R., Majewski, S.R., Skrutskie, M.F., Carpenter, J.M. et al. 2003, *AJ*, 126, 1871
- Lee, Y.-W.; Joo, J.-M.; Sohn, Y.-J.; Rey, S.-C.; Lee, H.-C.; & Walker, A. R., 1999, *Nature*, 402, 55
- Leon, S.; Meylan, G.; & Combes, F., 2000, *A&A*, 359, 907
- Lub, J., 2002, in *ASP Conf. Ser. 265, Omega Centauri: A Unique Window into Astrophysics*, ed. F. van Leeuwen, J. Hughes and G. Piotto (San Francisco: ASP), 95
- Lyngå, G., 1996, *A&AS*, 115, 297
- Majewski, S. R., Ostheimer, J. C., Kunkel, W. E. et al., 2000, *AJ*, 119, 760
- Majewski, S. R., Ostheimer, J. C., Kunkel, W. E. et al., 2000, *AJ*, 120, 2550
- Manfroid, J. & Selman, F. 2001, *The Messenger*, 104, 16
- Mateo, M., Fischer, P., & Krzeminski, W. 1995, *AJ*, 110, 2166
- Mateo, M., 1998, *ARA&A*, 36, 435
- Mateo, M., Hurley-Keller, D., & Nemec, J., 1998, *AJ*, 115, 1856
- Mayer, L.; Governato, F.; Colpi, M.; Moore, B.; Quinn, T.; Wadsley, J.; Stadel, J.; Lake, G., 2001, *ApJ*, 559, 754
- McNamara, D. H., 1995, *AJ*, 109, 1751

- Merritt, D., Meylan, G., & Mayor, M., 1997, *AJ*, 114, 1074
- Meylan, G., 1987, *A&A*, 184, 144
- Meylan, G., Mayor, M., Duquenois, A. & Dubath, P., 1995, *A&A*, 303, 761
- Mighell, K.J., 1989, *A&AS*, 82, 1
- Mighell, K.J., 1997, *AJ*, 114, 1458
- Monelli M. et al., 2003, *AJ*, 126, 218
- Monelli M. et al., 2003, *ASP Conf. Ser.* 296: *New Horizons in Globular Cluster Astronomy*, 388
- Morrison, H. L., Olszewski, E. W., Mateo, M. et al., 2001, *AJ*, 121, 283
- Mould, J. & Aaronson, M. 1983, *ApJ*, 273, 530
- Nemec, J.M., Nemec, A.F., Lutz, T.E., 1994, *AJ*, 108, 222
- Noble, R.G., et al., 1991, *MNRAS*, 250, 314
- Noels, A. & Grevesse, N. 1993 in *Origin and Evolution of the Elements*, ed. N. Prantzos, E. Vangioni-Flam, M. Casse (Cambridge: Cambridge Univ. Press), 15
- Norris, John E.; & Da Costa, G. S., 1995, *ApJ*, 447, 680
- Norris, John E.; Freeman, K. C.; & Mighell, K. J., 1996, *ApJ*, 462, 241
- Odenkirchen, M.; Grebel, E.K.; Dehnen, W.; Rix, H.W.; Yanny, B.; Newberg, H.J.; Rockosi, C.M.; Martinez-Delgado, D.; Brinkmann, J.; Pier, Jeffrey R.
- Origlia, L.; Ferraro, F.R.; Fusi Pecci, F.; Rood, R.T., 2002, *ApJ*, 571, 458
- Ortolani, S., & Rosino, L. 1987, *A&A*, 185, 1020
- Pagel, B.E.J. & Portinari, L. 1998, *MNRAS*, 298, 747
- Pancino, E.; Ferraro, F.R.; Bellazzini, M.; Piotto, G.; & Zoccali, M., 2000, *ApJ*, 534, 83
- Persson, S.E., Murphy, D.C., Krzeminski, W., Roth, M., & Rieke, M.J., 1996, *AJ*, 115, 2475
- Piatek, S.; Pryor, C.; Olszewski, E. W.; Harris, H. C.; Mateo, M.; Minniti, D.; Tinney, C. G
- Pickles, A.J., 1998, *PASP*, 110, 863

- Pietrinferni, A., Cassisi, S., Salaris, M., & Castelli, F., 2004, ApJ, 612, 168
- Piotto, G., et al. 2002, A&A, 391, 945
- Piotto, G., et al., astro-ph/0412016
- Prada Moroni, P. & Straniero, O. 2002, ApJ, 581, 585
- Predehl, P., & Schmitt, J. H. M. M. 1995, A&A, 293, 889
- Preston, G. W., & Sneden, C. 2000, AJ, 120, 1014
- Pryor, C., & Meylan, G., 1993, ASP Conf. Ser. 50: Structure and Dynamics of Globular Cluster, 357
- Pulone, L.; de Marchi, G.; Paresce, F.; Allard, F., 1998, ApJL 492, 41
- Renzini, A., et al. 1996, ApJ, 465, L23
- Renzini, A., Mengel, J. G., & Sweigart, A. V. 1977, A&A, 56, 369
- Rey, S. et al., 2000, AJ, 119, 1824
- Richer, H.,B. et al., 1991, ApJ, 381, 147
- Saha, A., Monet, D.G. & Seitzer, P. 1986, AJ, 322, L59
- Schlegel, D.J., Finkbeiner, D.P., Davis, M., 1998, ApJ, 500, 525
- Saviane, I., Held, E.V. & Bertelli, G., 2000, A&A, 355,56
- Serenelli A. M., Althaus L. G., Rohrmann R. D., Benvenuto O. G., 2002, MNRAS, 337, 1091
- Shetrone, M, Venn, K.A., Tolstoy, E., Primas, F., Hill, V., Kaufer, A., 2003, AJ, 125, 684
- Smecker-Hane, T. A., Stetson, P. B., Hesser, J. E., & Lehnert, M. D. 1994, AJ, 108, 507
- Smecker-Hane et al. 1996, in "From Stars to Galaxies", ASP Conference Series, 98, 328
- Smecker-Hane, T. A., Mandushev, G. I., Hesser, J. E., Stetson, P. B., Da Costa, G. S., & Hatzidimitriou, D., 1999, in ASP Conf. Ser. 192, Spectrophotometric Dating of Stars and Galaxies, ed. I. Hubeny, S. Heap, & R. Cornett (San Francisco: ASP), 159
- Smith, G. H., Wood, P. R., Faulkner, D. J., Wright, A. E., 1990, ApJ, 353, 168

- Sollima, A., Pancino, E., Ferraro, F.R., & Bellazzini, M. 2004, in *Chemical Abundances and Mixing in Stars in the Milky Way and its Satellites*, ed. L. Pasquini, S. Randich (Berlin: Springer-Verlag), in press
- Stetson, P.B, 1987, *PASP*, 99, 191
- Stetson, P.B, 1994, *PASP*, 106, 250
- Stetson, P.B, 2000, *PASP*, 112, 925
- Stetson, P. B., Hesser, J. E., & Smecker-Hane, T. A. 1998, *PASP*, 110, 533
- Stetson, P.B., Bruntt, H., & Grundahl, F. 2003, *PASP*, 115, 413
- Straniero, O., Chieffi, A., & Limongi, M. 1997, *ApJ*, 490, 425
- Suntzeff, N. B., & Kraft, R. P. 1996, *AJ*, 111, 1913
- Suntzeff, N. B., Schommer, R. A., Olszewski, E. W., & Walker, A. R. 1992, *AJ*, 104, 1743
- Thompson, I.B., Kaluzny, J., Pych, W., Burley, G. et al. 2001, *AJ*, 121, 3089
- Thoul, A., Bahcall, J., & Loeb, A. 1994, *ApJ* 421, 828
- Tolstoy, E., Venn, K.A., Shetrone, M., Primas, F., Hill, V., Kaufer, A., Szeifert, T., 2003, *AJ*, 125, 707
- Tolstoy, E., Irwin, M.J., Helmi, A., Battaglia, G., Jablonka, P., Hill, V., Venn, K. A., Shetrone, M. D., Letarte, B., Cole, A. A., Primas, F., Francois, P., Arimoto, N., Sadakane, K., Kaufer, A., Szeifert, T., Abel, T., 2004 *ApJ*, 617, 119
- Valdes, F., 1997, in *ASP Conf. Ser. 125, Astronomical Data Analysis Software and Systems VI*, ed. G. Hunt & H. E. Payne (San Francisco: ASP), 455
- van Leeuwen, F.; Le Poole, R. S.; Reijns, R. A.; Freeman, K. C.; de Zeeuw, P. T. 2000, *A&A*, 360, 472
- VandenBerg, D. A., Richard, O., Michaud, G., & Richer, J. 2002, *ApJ*, 571, 487
- E. Velrome, PhD thesis, "Dynamical models of axysymmetric and triaxial stellar systems", 2003, Leiden University
- Walcher, C. J., Fried, J. W., Burkert, A et al., 2003 *A&A*, 406, 847
- Walker, A. R. 1992, *AJ*, 103, 1166

Webbink, R.F., 1985, IAU Symposium 113, Dynamics of star clusters, 113,  
541

White, S.D.M., & Frenk, C.S., 1991, ApJ, 379, 52

Zinn, R., & West, M. J. 1984, ApJS, 55, 45